이학박사 학위논문

Theory and BD simulations of diffusion-controlled reactions and development of new constant-NPT MD method

확산지배반응 이론 및 브라운 동역학 모의실험과
새로운 일정 온도 일정 압력
분자동역학 방법론 개발

2019 년 8 월

서울대학교 대학원
화학부 물리화학 전공
김 민 정

Abstract

Theory and BD simulations of diffusion-controlled reactions and development of new constant-NPT MD method

Minjung Kim

Department of Chemistry

The Graduate School

Seoul National University

A variety of chemical reactions in natural or artificial systems are influenced by the relative diffusion rate of reactant molecules. Nevertheless, there still lacks a comprehensible account of diffusion-influenced reactions in many realistic conditions. To tackle this problem, many studies have been carried out from both theoretical and experimental aspects. To shed some light on this issue, this thesis intends to establish a theoretical and computational framework for diffusion-controlled reactions in some specific conditions. In this regard, we have also developed a new method for constant-NPT molecular dynamics that enables a reliable calculation of dynamic properties.

This thesis is composed of four chapters. First, an overview of the thesis is

given in Chapter 1. Diffusion-controlled reactions can be described by Smoluchowski's theory assuming that like reactant molecules do not interact with each other. This assumption is not valid when the concentration of reactant molecules gets higher. Chapter 2 presents a new theory that can be applied at high concentrations of reactant molecules. The electron transfer reaction with low activation energy is a representative example of the diffusion-controlled reaction. The previous analytic expressions for the time-dependent electron-transfer rate and the charge separation probability were obtained only for the case where the reaction can be assumed to occur at a contact separation. In Chapter 3, time-dependent electron transfer rate between geminate ions with strong Coulomb interaction and distance-dependent reactivity is examined. The well-established thermostatting and barostatting algorithms of molecular dynamics simulation may alter the dynamic properties of the molecules under consideration, because their equations of motion are modified by the coupling with the thermostat or the barostat. In Chapter 4, a new molecular dynamics simulation algorithm to obtain accurate dynamic properties as well as equilibrium properties is introduced.

Keywords : diffusion-controlled reactions, concentration effects, excluded volume effects, electron transfer rate, molecular dynamics
Student Number **:** 2011-23216

Table of Contents

List of tables

List of figures

Chapter 1

1. Introduction

Bimolecular reactions may be described as a two-step process. First, two reactant molecules diffuse through the medium until they encounter each other. Then, the chemical reaction process to form product molecules takes place. If the first step is slow enough to be a rate determining step, the whole reaction is called a diffusion-controlled reaction. Many kinds of reactions occurring in solution or solid are diffusion-influenced reactions. So, they have been studied extensively by many researchers. Nevertheless, a thorough understanding of diffusion-controlled reactions in realistic situations is still lacking. The aim of this thesis is to develop an effective theoretical and computational method to enable us to deal with the diffusion-controlled reaction properly. In this regard, a new method for constant-NPT molecular dynamics is also introduced.

The relative diffusion and reaction rates between reactant molecules are modified when like-particle interactions are present. These like-particle interactions become significant when the concentration of reactant molecules is high. In **Chapter 2**, we formulate a new theory of the effects of like-particle interactions on the irreversible diffusion-influenced bimolecular reactions of the type $A + B \to P + B$ by considering the evolution equation of the triplet ABB number density field explicitly. The solution to the evolution equation is aided by a recently proposed method for solving the Fredholm integral equation of the second kind. We evaluate the theory by comparing its predictions with the results of extensive

Brownian dynamics computer simulations. The present theory provides a reasonable explanation of the simulation results.

Previous analytic expressions for the time-dependent rate of diffusion-influenced electron-transfer between geminate ions were obtained for the case when the reaction occurs at a contact separation. But the reaction generally takes place at various separations by a distance-dependent reactivity. By applying a recently developed solution method for the Fredholm integral equation of the second kind, we obtain an accurate analytic expression for the time-dependent electron-transfer rate with the account of the distance-dependent reactivity in **Chapter 3**. We also consider the dependence of the rate on the initial separation between the geminate ions. We check the accuracy of the solution against numerical results obtained by solving the equation for the survival probability. The solution is found to be accurate enough for most reasonable parameter values.

In **Chapter 4**, we introduce a new molecular dynamics simulation method. The well-established molecular dynamics simulation methods for constant-NPT ensemble systems such as the Andersen-Nosé-Hoover method and their variants may alter the dynamic properties of the molecules under consideration, because their equations of motion are modified by the coupling with thermostat or barostat. To circumvent this artifact, we propose a new molecular dynamics simulation algorithm, by which only the molecules near the wall of the simulation box are coupled to the thermostat and barostat and the molecules of interest placed in the inner part of the simulation box remain intact. We test the efficiency of our algorithm in attaining the target temperature and pressure, and the conformity of

the calculated equilibrium and dynamic properties to those of a constant-NPT ensemble system.

Chapter 2

2. Concentration effects on the rates of irreversible diffusion-influenced reactions

2.1. Introduction

There are a plenty of reactions occurring in solution as well as in solids, whose reaction rates are influenced by the diffusion rates of reactants.[1,2] In many theories of diffusion-influenced reactions, one consider a central reactant molecule, say *A*, surrounded by the other reactant molecules, say *B*. This Smoluchowski approach is exact when the central *A* molecule is immobile and the surrounding *B*'s do not interact with each other.[3-5] However, interactions between the *B* molecules introduce reactive interference[6,7] and modify the relative diffusion rate between *A* and *B*.[8-12]

Many investigations have been made that addressed the deficiency of the Smoluchowski theory due to the neglect of the interactions among reactants of the same species. In this work, we deal with the case that can be treated by considering the diffusive dynamics of a single *A* and many *B*'s. The case requiring the consideration of several or many *A*'s will not be considered.[13-17]

When the dominant interaction between the *B*'s is a repulsive one, it will prevent the *B* molecules to overlap. Blumen and Manz considered such an excluded volume (EV) effect on reactions occurring in a solid solution based on a lattice model.[18,19] They generalized their results to a continuum limit, but the theory is not applicable to reactions occurring in the liquid solution. Kalnin also

considered the EV effect, but his analysis was limited to the long-time regime and to the case of small concentration.[20] Swallen *et al.* noted the importance of EV effect on the long-range electron transfer reaction.[21,22] They extended the Blumen–Manz theory by including the molecular diffusion process and compared the theoretical results with Monte Carlo simulations, but the agreement was not satisfactory when the packing fraction of electron acceptors is greater than 5%.

Jung and Lee[6] and Lee et al.[7] investigated the transient kinetics of reactions of the type $A + B \rightarrow P + B$ with *B* present in much excess. Jung and Lee evaluated the effect of reactive interference among *B*'s on the diffusion-influenced reaction rate by solving numerically the coupled evolution equations for reduced distribution functions (RDFs) of reactants. By employing the many-particle kernel (MPK) formalism, which was developed to evaluate the many-particle effects on the kinetics of diffusion-influenced reactions,[23 - 25] Lee et al.[7] obtained an approximate analytic expression for the time-dependent survival probability of the central *A* molecule. To assess the accuracy of the analytic expression, they also carried out Brownian dynamics (BD) simulations and showed that the analytic results agreed with simulations when the packing fraction of *B* molecules is less than 7%.

Dzubiella and McCammon,[9] and more recently, Piazza and his coworkers[10-12] investigated the effects of particle number density on the rates of reactions of the type $A + B \rightarrow A + P$ with *B* present in much excess; for this reaction type, there is no reactive interference among *B*'s. These authors employed the generalized Smoluchowski equation,[8] including the influence of the osmotic pressure gradient,

to derive analytic expressions for the steady-state rate constant, and assessed the theories against computer simulations. A good agreement was found up to the packing fraction as high as 0.5 when the size of A is much bigger than that of B.

Litniewski carried out extensive investigations of the influence of reactant concentrations on the rate of irreversible bimolecular reactions of various types by molecular dynamics simulations as well as BD simulations.[26,27] Seki et al. investigated the EV effect (site blocking effect) on diffusion-mediated reactions based on a lattice model with prohibited double occupancy of the lattice sites.[28-31] They considered the effects of excluded volumes of inert particles as well as those of reactants, and the theoretical rate expressions were assessed by Monte Carlo simulations.

In this work, we present a refined theory of the reactive interference effects on the transient kinetics of diffusion-influenced reactions. We consider irreversible bimolecular reactions of the type $A + B \to P + B$. To take a proper account of the reactive interference effects, one needs to solve the evolution equation of the triplet ABB number density field explicitly. By employing the recently proposed solution method for the Fredholm integral equation of the second kind,[32-34] we derive an approximate analytic expression for the ABB number density field, which in turn enables us to evaluate the reactive interference effects. For the steady-state reaction rates, we consider the combined effects of the reactive interference and the osmotic pressure gradient. We assess the theory by comparing its predictions with the results of extensive computer simulations. The new theory provides a reasonable explanation of the simulation results.

2.2. Theory

2.2.1. Evolution equations for reduced distribution functions

Let us consider a simple model of an irreversible reaction of the type $A + B \rightarrow P + B$, where the reactants A and B are represented by spherical particles with diameter σ_A and σ_B, respectively. The reaction occurs upon contact of A and B at the separation of $\sigma \ \left[\equiv (\sigma_A + \sigma_B)/2\right]$. Suppose that the reactant B is present in much excess of A. In such a case the reaction dynamic coupling between A particles can be neglected, and one can describe the reaction kinetics by considering a single A surrounded with many B's.

For this reaction system, the reactant-molecule reduced distribution function (RDF) theory provides the following kinetic equation,[23,35]

$$\frac{d}{dt} Y_A(t) = -k_f(t) C_B Y_A(t), \tag{2.1}$$

where $Y_A(t)$ is the probability that an A molecule located at the coordinate origin has not reacted by time t. C_B is the bulk number density of B particles, and $k_f(t)$ is the time-dependent bimolecular rate coefficient given by

$$k_f(t) = \kappa \rho(\sigma, t). \tag{2.2}$$

κ is an intrinsic rate constant and $\rho(r,t)$ is the nonequilibrium pair correlation function between A and B particles. $\rho(r,t)$ is related to the number density field $C_B(r,t)$ of B particles as

$$\rho(r,t) = C_B^{-1} C_B(r,t). \tag{2.3}$$

$C_B(r,t)4\pi r^2 dr$ represents the average number of *B* particles at time *t* within a spherical shell of width *dr* at a distance *r* from the origin, given that an *A* particle is at the origin.

The evolution equation for $C_B(r,t)$ is given by[23,35]

$$\frac{1}{Y_A(t)}\frac{\partial}{\partial t}Y_A(t)C_B(r,t) = L_1(r)C_B(r,t) - \frac{\kappa\delta(r-\sigma)}{4\pi\sigma^2}C_B(r,t)$$

$$-\int d\mathbf{r}'\frac{\kappa\delta(|\mathbf{r}'|-\sigma)}{4\pi\sigma^2}C_{BB}(\mathbf{r},\mathbf{r}',t) \qquad (2.4)$$

where $L_1(r)$ is the mean evolution operator for $C_B(r,t)$ in the absence of reaction. We assume that the mean transport of *B* particles to the central *A* is not coupled with the reaction events. A rigorous expression for $L_1(r)$ is rather complicated, depending even on time.[36] The second term on the right hand side of Eq. (2.4) represents a change due to the reaction between an *A* at the origin and a *B* at $\mathbf{r}$. The last term of Eq. (2.4) represents the reactive interference of a second *B* particle at $\mathbf{r}'$ into the reaction dynamics of the just mentioned *A*-*B* pair. $C_{BB}(\mathbf{r},\mathbf{r}',t)$ represents the product of number densities of *B* particles at the positions $\mathbf{r}$ and $\mathbf{r}'$ at time *t*, given that an *A* particle is at the origin. It is related to the usual three-particle RDF $C_{ABB}(\mathbf{r}_A,\mathbf{r}_B,\mathbf{r}_B',t)$ (also called the triplet *ABB* number density field) as $C_{ABB}(\mathbf{r}_A,\mathbf{r}_B,\mathbf{r}_B',t) = Y_A(t)C_{BB}(\mathbf{r}_B-\mathbf{r}_A,\mathbf{r}_B'-\mathbf{r}_A,t)$.

The evolution equation for $C_{BB}(\mathbf{r},\mathbf{r}',t)$ is in turn given by[23,35]

$$\frac{1}{Y_A(t)}\frac{\partial}{\partial t}Y_A(t)C_{BB}(\mathbf{r},\mathbf{r}',t) = L_2(\mathbf{r},\mathbf{r}')C_{BB}(\mathbf{r},\mathbf{r}',t)$$

$$-\left[\frac{\kappa\delta(|\mathbf{r}|-\sigma)}{4\pi\sigma^2}+\frac{\kappa\delta(|\mathbf{r}'|-\sigma)}{4\pi\sigma^2}\right]C_{BB}(\mathbf{r},\mathbf{r}',t)$$

$$-\int d\mathbf{r}''\frac{\kappa\delta(|\mathbf{r}''|-\sigma)}{4\pi\sigma^2}C_{BBB}(\mathbf{r},\mathbf{r}',\mathbf{r}'',t) \tag{2.5}$$

$L_2(\mathbf{r},\mathbf{r}')$ is the mean evolution operator for $C_{BB}(\mathbf{r},\mathbf{r}',t)$ in the absence of reaction. The last term on the right hand side represents the reactive interference of a third *B* particle at $\mathbf{r}''$ into the reaction dynamics of the triplet of particles, *A* at the origin and two *B*'s at $\mathbf{r}$ and $\mathbf{r}'$. The RDF $C_{BBB}(\mathbf{r},\mathbf{r}',\mathbf{r}'',t)$ represents the product of number densities of *B* particles at the positions $\mathbf{r}$, $\mathbf{r}'$, and $\mathbf{r}''$ at time *t*, given that an *A* particle is at the origin; it is related to the usual four-particle RDF $C_{ABBB}(\mathbf{r}_A,\mathbf{r}_B,\mathbf{r}_B',\mathbf{r}_B'',t)$ as $C_{ABBB}(\mathbf{r}_A,\mathbf{r}_B,\mathbf{r}_B',\mathbf{r}_B'',t)=Y_A(t)$ $\times C_{BBB}(\mathbf{r}_B-\mathbf{r}_A,\mathbf{r}_B'-\mathbf{r}_A,\mathbf{r}_B''-\mathbf{r}_A,t)$. The whole set of evolution equations for the reactant-molecule RDFs are coupled in a hierarchical manner.[35] To get an explicit expression for an RDF, we need to introduce an appropriate truncation approximation.

2.2.2. Separation of the reactive interference effect

From Eqs. (2.1) – (2.3), the survival probability of an *A* at time *t* is given by

$$Y_A(t)=\exp\left[-\kappa\int_0^t d\tau\, C_B(\sigma,\tau)\right] \tag{2.6}$$

Using Eq. (2.1), the evolution equation (2.4) for $C_B(r,t)$ can be rewritten as

$$\frac{\partial}{\partial t}C_B(r,t)-k_f(t)C_BC_B(r,t)=L_1(r)C_B(r,t)$$

$$-\frac{\kappa\delta(r-\sigma)}{4\pi\sigma^2}C_B(r,t)-\int d\mathbf{r}'\frac{\kappa\delta(|\mathbf{r}'|-\sigma)}{4\pi\sigma^2}C_{BB}(\mathbf{r},\mathbf{r}',t) \tag{2.7}$$

If we may neglect the *direct correlation* in the thermal motions of the *B* particles as well as the reactive interference among them, the second term on the left and the last term on the right cancel out. That is, for such *effectively* independent *B*'s we have

$$\frac{\partial}{\partial t}C_B^0(r,t)=L_1(r)C_B^0(r,t)-\frac{\kappa\delta(r-\sigma)}{4\pi\sigma^2}C_B^0(r,t)\,. \tag{2.8}$$

Note that $L_1(r)$ is the mean evolution operator for a *B* particle which may include average influence of other *B* particles as the Hartree-Fock potential includes the average influence of other electrons on the motion of an effectively independent electron. Hereafter, the superscript "0" designates a quantity for such a hypothetical system in which *B* particles move without direct correlation and react with *A* independently of one another.

Let us denote the difference $C_B(r,t)-C_B^0(r,t)$ by $X(r,t)$. We then have

$$Y_A(t)=Y_A^0(t)\exp\left[-\kappa\int_0^t d\tau\, X(\sigma,\tau)\right] \tag{2.9}$$

with $Y_A^0(t)=\exp\left[-\kappa\int_0^t d\tau\, C_B^0(\sigma,\tau)\right]$, denoting the survival probability in the above-mentioned hypothetical system. From Eqs. (2.7) and (2.8), the equation for $X(r,t)$ is given by

$$\frac{\partial}{\partial t}X(r,t)=L_1(r)X(r,t)-\frac{\kappa\delta(r-\sigma)}{4\pi\sigma^2}X(r,t)$$

$$+k_f(t)C_BC_B(r,t)-\int d\mathbf{r}'\frac{\kappa\delta(|\mathbf{r}'|-\sigma)}{4\pi\sigma^2}C_{BB}(\mathbf{r},\mathbf{r}',t) \tag{2.10}$$

To evaluate the last term we now make a factorization approximation:

$$C_{BB}(\mathbf{r},\mathbf{r}',t)\cong C^0_{BB}(r,r',t)e^{-U_{BB}(|\mathbf{r}-\mathbf{r}'|)} \tag{2.11}$$

where U_{BB} is the potential of mean force between a pair of *B* particles in units of k_BT. By taking the polar axis of the $\mathbf{r}'$-space in the direction of $\mathbf{r}$, we then obtain

$$\int d\mathbf{r}'\frac{\kappa\delta(|\mathbf{r}'|-\sigma)}{4\pi\sigma^2}C_{BB}(\mathbf{r},\mathbf{r}',t)=\kappa C^0_{BB}(r,\sigma,t)[1-v_B(r)];$$

$$v_B(r)\equiv 1-\frac{1}{2}\int_{-1}^{1}d\mu\exp\left[-U_{BB}\left(\sqrt{r^2+\sigma^2-2r\sigma\mu}\right)\right] \tag{2.12}$$

where μ denotes the cosine of the angle between $\mathbf{r}$ and $\mathbf{r}'$; that is, $\mu=\mathbf{r}\cdot\mathbf{r}'/(rr')$. With Eq. (2.12), Eq. (2.10) becomes

$$\frac{\partial}{\partial t}X(r,t)=L_1(r)X(r,t)-\frac{\kappa\delta(r-\sigma)}{4\pi\sigma^2}X(r,t)$$

$$+[k_f(t)C_BC_B(r,t)-\kappa C^0_{BB}(r,\sigma,t)]+v_B(r)\kappa C^0_{BB}(r,\sigma,t) \tag{2.13}$$

It is expected that the third square-bracketed term on the right hand side should be small compared to other terms since $\kappa C^0_{BB}(r,\sigma,t)\cong\kappa C^0_B(\sigma,t)C^0_B(r,t)=k^0_f(t)C_BC^0_B(r,t)$. We thus obtain the following evolution equation for $X(r,t)$:

$$\frac{\partial}{\partial t}X(r,t)=L_1(r)X(r,t)-\frac{\delta(r-\sigma)}{4\pi\sigma^2}\kappa X(\sigma,t)+\kappa v_B(r)C^0_{BB}(r,\sigma,t) \tag{2.14}$$

Let us assume that *B* particles are distributed initially in equilibrium around *A*;

that is, $C_B(r,0) = C_B^0(r,0) = C_B g(r)$ with $g(r)$ denoting the equilibrium radial distribution function. Hence $X(r,0) = 0$, and the Laplace transform expression for $X(\sigma,t)$ can be obtained from Eq. (2.14) as

$$\hat{X}(\sigma,s) = \frac{\kappa \int d\mathbf{r}\, \hat{G}(\sigma,s|r) v_B(r) \hat{C}_{BB}^0(r,\sigma,s)}{1+\kappa \hat{G}(\sigma,s|\sigma)}, \tag{2.15}$$

where the caret symbol denotes Laplace-transformed quantities, and $\hat{G}(r,s|r_0)$ is the Laplace transform of the diffusive propagator for a pair of *A* and *B* particles:[32,33]

$$\hat{G}(r,s|r_0) = \frac{1}{s-L_1(r)} \frac{\delta(r-r_0)}{4\pi r_0^2} \tag{2.16}$$

.

2.2.3. Approximate expression for $\hat{C}_{BB}^0(r,\sigma,s)$

An analytically solvable evolution equation for $C_{BB}^0(r,\sigma,t)$ can be derived from Eq. (2.5) with the following approximations:

$$L_2(\mathbf{r},\mathbf{r}') \cong L_1(r) + L_1(r') \tag{2.17}$$

$$C_{BBB}^0(r,r',r'',t) \cong C_{BB}^0(r,r',t) C_B^0(r'',t) \tag{2.18}$$

Noting that $C_{BB}^0(r,r',t=0) = C_B^2 g(r) g(r')$, we obtain after some algebra the following equation for $\hat{C}_{BB}^0(r,r',s)$

$$s\hat{C}_{BB}^0(r,r',s) - C_B^2 g(r) g(r') = L_1(r)\hat{C}_{BB}^0(r,r',s) + L_1(r')\hat{C}_{BB}^0(r,r',s)$$
$$-\kappa \hat{C}_{BB}^0(\sigma,r',s) \frac{\delta(r-\sigma)}{4\pi\sigma^2} - \kappa \hat{C}_{BB}^0(r,\sigma,s) \frac{\delta(r'-\sigma)}{4\pi\sigma^2} \tag{2.19}$$

The last term on the right hand side is manipulated as

$$\kappa\hat{C}^0_{BB}(r,\sigma,s)\frac{\delta(r'-\sigma)}{4\pi\sigma^2}=\kappa\hat{C}^0_{BB}(r,\sigma,s)[s-L_1(r')]\frac{1}{s-L_1(r')}\frac{\delta(r'-\sigma)}{4\pi\sigma^2}$$

$$=\kappa\hat{C}^0_{BB}(r,\sigma,s)[s-L_1(r')]\hat{G}(r',s|\sigma) \tag{2.20}$$

Then noting that $L_1(r')\hat{C}^0_{BB}(r,r',s)\Big|_{r'=\sigma}=0$ and $L_1(r')\hat{G}(r',s|\sigma)\Big|_{r'=\sigma}=0$ due to the reflecting boundary condition, we obtain the following integral equation for $\hat{C}^0_{BB}(r,\sigma,s)$:

$$\hat{C}^0_{BB}(r,\sigma,s)=C_B^2 g(\sigma)s^{-1}g(r)-\kappa\hat{C}^0_{BB}(\sigma,\sigma,s)\hat{G}(r,s|\sigma)$$

$$-\kappa s\hat{G}(\sigma,s|\sigma)\int d\mathbf{r}_0\hat{G}(r,s|r_0)\hat{C}^0_{BB}(r_0,\sigma,s) \tag{2.21}$$

This integral equation can be solved formally as[32,34]

$$\hat{C}^0_{BB}(r,\sigma,s)=\frac{C_B^2 g(\sigma)s^{-1}g(r)-\kappa\hat{C}^0_{BB}(\sigma,\sigma,s)\hat{G}(r,s|\sigma)}{1+\kappa s\hat{G}(\sigma,s|\sigma)\int d\mathbf{r}_0\hat{G}(r,s|r_0)\left[\hat{C}^0_{BB}(r_0,\sigma,s)/\hat{C}^0_{BB}(r,\sigma,s)\right]} \tag{2.22}$$

with

$$\hat{C}^0_{BB}(\sigma,\sigma,s)$$

$$=\frac{C_B^2[g(\sigma)]^2 s^{-1}}{1+\kappa\hat{G}(\sigma,s|\sigma)+\kappa s\hat{G}(\sigma,s|\sigma)\int d\mathbf{r}_0\hat{G}(\sigma,s|r_0)\left[\hat{C}^0_{BB}(r_0,\sigma,s)/\hat{C}^0_{BB}(\sigma,\sigma,s)\right]}$$

From Eq. (2.22), by setting the ratio $\hat{C}^0_{BB}(r_0,\sigma,s)/\hat{C}^0_{BB}(r,\sigma,s)$ to $g(r_0)/g(r)$, a first-order approximation for $\hat{C}^0_{BB}(r,\sigma,s)$ can be obtained as

$$\hat{C}^0_{BB}(r,\sigma,s)=\frac{C_B^2 g(\sigma)g(r)\left[1+2\kappa\hat{G}(\sigma,s|\sigma)\right]-\kappa\hat{G}(r,s|\sigma)C_B^2[g(\sigma)]^2}{s\left[1+\kappa\hat{G}(\sigma,s|\sigma)\right]\left[1+2\kappa\hat{G}(\sigma,s|\sigma)\right]} \tag{2.23}$$

In the diffusion-controlled limit ($\kappa\to\infty$), this reduces to

$$\hat{C}^0_{BB}(r,\sigma,s)=\frac{C_B^2 g(\sigma)}{2s\kappa\hat{G}(\sigma,s|\sigma)}\left[2g(r)-\frac{\hat{G}(r,s|\sigma)}{\hat{G}(\sigma,s|\sigma)}g(\sigma)\right] \tag{2.24}$$

2.2.4. Expressions for the survival probability and the steady-state rate constant

From Eq. (2.9), we have

$$Y_A(t)=Y_A^0(t)\exp\left\{-L^{-1}\left[s^{-1}\kappa\hat{X}(\sigma,s)\right]\right\} \tag{2.25}$$

where L^{-1} denotes the inverse Laplace transformation operator. By putting Eq. (2.23) or Eq. (2.24) for $\hat{C}^0_{BB}(r,\sigma,s)$ into Eq. (2.15) for $\hat{X}(\sigma,s)$ and performing the inverse Laplace transformation, we can calculate the survival probability from Eq. (2.25). To get a concrete result, we have to fix the model for diffusive thermal motion for a pair of *A* and *B* particles in the absence of reaction. We will provide an exemplary model calculation in Sec. IV to compare with the BD simulations described in the next section.

It is very difficult to calculate the steady-state rate constant $k_f(\infty)$ from the simulated survival probability curve because the long-time data are statistically noisy. At any rate, it would be interesting to compare the rough estimate for $k_f(\infty)$ with the theoretical estimate given by

$$k_f(\infty)=k_f^0(\infty)+\lim_{s\to 0}C_B^{-1}s\kappa\hat{X}(\sigma,s) \tag{2.26}$$

2.3. Brownian dynamics simulation

We have carried out BD simulations to study the effects of interaction between

the reactants of the same species on the diffusion-influenced reaction rates. The reaction system consists of hard spheres immersed in a viscous medium. A single particle A is placed at the center of the cubic simulation box and kept fixed throughout the simulation. Initially the B particles are placed randomly without overlap around the central A particle. The reason for choosing the random initial distribution of B particles rather than the equilibrium distribution is that we want to evaluate the concentration effect on the reaction rate that is free from the effect of potential of mean force.

When the packing fraction ϕ_B of B particles is high, placing thousands of B particles without overlap seems not an easy task. Hence, we first equilibrate the configuration of all particles and then randomize the positions of about one hundred B particles in the vicinity of the particle A. This procedure ensures that the simulation result at very low concentration of B particles fits well with the prediction of the simple Smoluchowski theory.

The movement of the B particles is first conducted according to the diffusive BD method of Ermak and McCammon:[37]

$$\mathbf{r}_i(t+\Delta t) = \mathbf{r}_i(t) + \mathbf{R}_i \,. \tag{3.1}$$

$\mathbf{r}_i(t)$ is the position of particle i at time t, and $\mathbf{R}_i$ is the random diffusive displacement with zero mean and variance given by $\langle R_{i\alpha} R_{j\beta} \rangle = 2D_0 \Delta t \delta_{ij} \delta_{\alpha\beta}$; α and β denote the Cartesian components and D_0 is the diffusion constant of a B particle. We are neglecting the hydrodynamic interaction. Since the B particles are hard spheres, there is no movement due to a systematic force. However, any

overlap of *B* particles must not be allowed. This may cause some difficulty because when the packing fraction is high many *B*'s would overlap in a BD step. We use an "elastic collision method" of Strating[38] to resolve this problem. If there is an overlap in a BD step, all the particles are repositioned to their original position. Then, thermal velocities of particles are calculated by the relation, $\mathbf{v}_i = \mathbf{R}_i / \Delta t$, and the step is propagated essentially as in the hard-sphere MD method.[39] For the simulation result to be free of inertial effect, the time step Δt must be chosen to be small.

When any *B* particle comes into contact with the *A* particle, the trajectory is terminated, and the time is recorded. The survival probability is calculated as

$$Y_A(t) = \lim_{N_T \to \infty} N(t) / N_T \tag{3.2}$$

where $N(t)$ is the number of trajectories in which *A* survives until time *t* and N_T is the total number of trajectories.

The basic units used in the simulations are as follows; length in σ_B, and time in σ_B^2 / D_0. Table 2.1 summarizes the simulated systems. In each of the four systems, we vary the diameter σ_A of the central *A* particle as 0.5, 1.0, and 2.0. The time step size is 0.0005. Since we use the periodic boundary condition, there is a possibility that a *B* particle may react with the *A* particle in the image box. Hence we take the system size large enough to avoid such an event to occur.

Table 2.1. Number of *B* particles, box size, and the packing fraction of *B* particles of simulated systems; $\phi_B = N_B(4\pi/3)(\sigma_B/2)^3/L^3$.

System	N_B (number of B's)	L (box length)	ϕ_B (volume fraction)
I	4912	60.0	0.0119
II	4095	35.0	0.0500
III	3374	25.0	0.113
IV	2196	18.0	0.197

2.4. Results and discussion

2.4.1. Evaluation of theoretical expressions

The model systems simulated by BD as described in the previous section correspond to the diffusion-controlled case ($\kappa \to \infty$). The interaction potentials between the *A* and *B* reactants are those of hard spheres. Hence the equilibrium pair correlation function between *A* and *B* particles is given by $g(r) = 1$ for $r \geq \sigma$, and the excluded volume function $v_B(r)$ defined in Eq. (2.12) becomes

$$v_B(r) = \begin{cases} 1 & \text{for } \sigma < r < \sigma_B - \sigma \\ \dfrac{\sigma_B^2 - (r-\sigma)^2}{4r\sigma} & \text{for } \max(\sigma, \sigma_B - \sigma) < r < \sigma + \sigma_B \\ 0 & \text{for } r > \sigma + \sigma_B \end{cases} \tag{4.1}$$

To evaluate the survival probability expression in Eq. (2.25), we have first to calculate the integral given in Eq. (2.15) with the expression for the three-particle RDF $\hat{C}_{BB}^0(r,\sigma,s)$ in Eq. (2.24). In the $\kappa \to \infty$ limit we have

$$\kappa \hat{X}(\sigma,s) = \frac{\int d\mathbf{r}\, \hat{G}(\sigma,s|r) v_B(r) \kappa \hat{C}_{BB}^0(r,\sigma,s)}{\hat{G}(\sigma,s|\sigma)}$$

$$= \frac{C_B^2}{2s[\hat{G}(\sigma,s|\sigma)]^2} \int d\mathbf{r}\, \hat{G}(\sigma,s|r) v_B(r) \left[2 - \frac{\hat{G}(r,s|\sigma)}{\hat{G}(\sigma,s|\sigma)} \right]$$

$$= \frac{C_B^2}{2s^2[\hat{G}(\sigma,s|\sigma)]^2} \left[2I(s) - J(s) \right], \tag{4.2}$$

where $I(s)$ and $J(s)$ are defined by

$$I(s) \equiv s \int d\mathbf{r}\, \hat{G}(\sigma,s|r) v_B(r),$$

$$J(s) \equiv s[\hat{G}(\sigma,s|\sigma)]^{-1}\int d\mathbf{r}\,\hat{G}(\sigma,s|r)\hat{G}(r,s|\sigma)v_B(r)\,. \tag{4.3}$$

For the model systems under consideration, the effective thermal evolution operator L_1 for a *B* particle may be assumed to be given by[8-11]

$$L_1(r,t) = \frac{D_0}{r^2}\frac{\partial}{\partial r}r^2\Phi(r,t)\frac{\partial}{\partial r} \quad \text{for} \quad r \geq \sigma\,, \tag{4.4}$$

where $\Phi(r,t)$ accounts for the effect from the osmotic pressure gradient. A model expression for $\Phi(r,t)$ is discussed in the Appendix. Many assumptions and approximations are necessary to validate the expression in Eq. (4.4). In particular, the *B*-particle number density field $C_B(r,t)$ varies linearly over the range of the interaction potential between a pair of *B* particles. It is not likely that the above evolution operator works at short times during which $C_B(r,t)$ varies rapidly with time and has a steep slope near the contact distance σ.

Hence, in dealing with transient kinetics, we confine ourselves to investigating the reactive interference effect. That is, we assume that L_1 is given by the simple diffusion operator. The diffusive propagator defined by Eq. (2.16) is then given by[40]

$$\hat{G}(r,s\,|\,r_0) = \frac{1}{8\pi D_0\zeta r r_0}\left[e^{-\zeta|r-r_0|} + \frac{\zeta\sigma-1}{\zeta\sigma+1}e^{-\zeta(r+r_0-2\sigma)}\right] \tag{4.5}$$

where $\zeta = \sqrt{s/D_0}$. Then the integrals defined in Eq. (4.3) can be evaluated analytically, and the final expression for $\hat{X}(\sigma,s)$ is given by

$$s^{-1}\kappa\hat{X}(\sigma,s) = \frac{C_B^2 k_D^2}{2}\frac{(1+\sigma\zeta)^2}{s^3}\left[2I(s) - J(s)\right], \tag{4.6}$$

where $k_D = 4\pi D_0 \sigma$. $I(s)$ and $J(s)$ are given by

$$I(s) = \frac{e^{-\zeta\sigma_B}[2 + 2\zeta\sigma_B + e^{\zeta\sigma_B}(\zeta^2\sigma_B^2 - 2)]}{4\zeta\sigma(1+\zeta\sigma)},$$

$$J(s) = [16(1+\zeta\sigma)]^{-1}\left\{[1 - 2\zeta(\sigma - \sigma_B)]e^{-2\zeta\sigma_B} + (2\zeta\sigma - 1)\right.$$

$$\left. + 4e^{2\zeta\sigma}\zeta^2(\sigma - \sigma_B)(\sigma + \sigma_B)\left[\mathrm{Ei}(-2\zeta\sigma) - \mathrm{Ei}\left(-2\zeta(\sigma + \sigma_B)\right)\right]\right\}. \quad (4.7)$$

where the exponential integral $\mathrm{Ei}(z)$ is defined by $\mathrm{Ei}(z) = -\int_{-z}^{\infty} dt\, e^{-t}/t$.[41]

Substituting Eq. (4.6) into Eq. (2.25), we have

$$Y_A(t) = Y_A^0(t)\exp\left\{-L^{-1}\left[\frac{C_B^2 k_D^2}{2}\frac{(1+\sigma\zeta)^2}{s^3}\left[2I(s) - J(s)\right]\right]\right\}. \quad (4.8)$$

$Y_A^0(t)$ is the Smoluchowski expression for the survival probability that is given by[1]

$$Y_A^0(t) = \exp\left\{-C_B k_D\left[t + 2\sqrt{\frac{\sigma^2 t}{\pi D_0}}\right]\right\} \quad (4.9)$$

To evaluate Eq. (4.8), one needs to perform the inverse Laplace transformation numerically.

A much simpler expression for the survival probability can be obtained which is valid for short times. In Eq. (4.2), we note that for large s, $\hat{G}(\sigma, s|r)$ decays rapidly with increasing $|r - \sigma|$. Hence we may make the following approximation:

$$\int d\mathbf{r}\, \hat{G}(\sigma, s|r) v_B(r)\kappa\hat{C}_{BB}^0(r,\sigma,s) \cong v_B(\sigma)\kappa\hat{C}_{BB}^0(\sigma,\sigma,s)\int d\mathbf{r}\, \hat{G}(\sigma, s|r)$$

$$= v_B(\sigma)\kappa\hat{C}_{BB}^0(\sigma,\sigma,s)s^{-1} \quad (4.10)$$

This gives the following approximation for $\hat{X}(\sigma,s)$:

$$s^{-1}\kappa\hat{X}(\sigma,s)=\frac{v_B(\sigma)C_B^2k_D^2}{2}\frac{(1+\sigma\zeta)^2}{s^3}. \tag{4.11}$$

Inverse Laplace transformation of Eq. (4.11) gives

$$Y_A(t)=Y_A^0(t)\exp\left\{-\frac{v_B(\sigma)C_B^2k_D^2}{2}\left[\frac{t^2}{2}+\frac{8}{3\sqrt{\pi}}\sqrt{\frac{\sigma^2}{D_0}}t^{3/2}+\frac{\sigma^2t}{D_0}\right]\right\} \tag{4.12}$$

For the steady-state rate constant, we consider the osmotic pressure gradient as well as the reactive interference. From Eqs. (2.26), (4.2), and (4.3) we have

$$k_f(\infty)=k_f^0(\infty)$$

$$+\frac{C_B}{2\hat{G}(\sigma,0|\sigma)}\int d\mathbf{r}\,v_B(r)\left[2\frac{\hat{G}(\sigma,0|r)}{\hat{G}(\sigma,0|\sigma)}-\frac{\hat{G}(\sigma,0|r)}{\hat{G}(\sigma,0|\sigma)}\frac{\hat{G}(r,0|\sigma)}{\hat{G}(\sigma,0|\sigma)}\right] \tag{4.13}$$

For the simple model excluding the effect of the osmotic pressure gradient, we have $k_f^0(\infty)=[\hat{G}(\sigma,0|\sigma)]^{-1}=4\pi D_0\sigma$. Then, Eq. (4.13) reduces to

$$\frac{k_f(\infty)}{k_D}=1+4\phi_B\left\{1+\frac{3\sigma}{8\sigma_B^3}\left[\sigma_B(\sigma_B-2\sigma)-2(\sigma-\sigma_B)(\sigma+\sigma_B)\ln\frac{\sigma}{\sigma+\sigma_B}\right]\right\}, \tag{4.14}$$

where ϕ_B is the packing fraction of *B* particles: $\phi_B=C_B(4\pi/3)(\sigma_B/2)^3$.

In Appendix, we derive an expression for $k_f(\infty)$, which takes account of the combined effects of the reactive interference and the osmotic pressure gradient. The final result is

$$\frac{k_f(\infty)}{k_D}=\left[\frac{1+\phi_B+\phi_B^2-\phi_B^3}{(1-\phi_B)^3}\right]\left\{1+C_B\int d\mathbf{r}\,v_B(r)\left[\frac{\tilde{\sigma}}{\tilde{r}}-\frac{1}{2}\left(\frac{\tilde{\sigma}}{\tilde{r}}\right)^2\right]\right\}. \tag{4.15}$$

The tilded variables, $\tilde{\sigma}$ and $\tilde{r}$, are defined by Eq. (A.6) in Appendix. We note

that the first square-bracketed factor on the right hand side represents the effect of the osmotic pressure gradient in the absence of reactive interference.[10] On the other hand, the quantity in the curly brackets represents mainly the reactive interference effect; its numerical value is not much different from that of Eq. (4.14). Hence the effects of the reactive interference and the osmotic pressure gradient are roughly multiplicative.

2.4.2. Comparison with simulation results

For each of the four systems listed in Table 2.1 and for the varying size of central A particle, we calculate the time-dependent survival probability of A from 40,000 trajectories. In Figure 2.1 through 2.4, the simulated $Y_A(t)$ vs. t curves are plotted along with the theoretical predictions of the simple Smoluchowski theory [Eq. (4.9)] and Eqs. (4.8) and (4.12) of the present theory.

Figure 2.1 displays the results for the cases when the packing fraction of B particles is very low ($\phi_B = 0.0119$). In these cases, regardless of the size ratio σ_A / σ_B, the survival probability curves from BD simulation, Smoluchowski theory, and Eq. (4.8) of the present theory are all in good agreement with each other; they are indistinguishable in the inset figures displaying $Y_A(t)$ vs. t curves. However, even at this small value of ϕ_B, small deviations of the Smoluchowski theory from BD simulations are noticeable at long times. The short-time approximation for $Y_A(t)$ in Eq. (4.12) is reliable only up to the time when $Y_A(t)$ reduces to one half.

Figure 2.2 displays the results for the cases with $\phi_B = 0.0500$. In these cases the Smoluchowski theory obviously underestimates the reaction rate. In contrast, Eq. (4.8) of the present theory is in good agreement with BD simulation at least up to the time when $Y_A(t)$ has an appreciable value, as can be seen in the inset figures. Eq. (4.12) also appears to be in agreement with BD simulation due to error cancellation; see inset figures.

Figures 2.3 and 2.4 show that the theoretical survival probability curves from Eqs. (4.8) and (4.12) of the present theory deviate increasingly from the simulated curves as the packing fraction increases. The deviations are much larger when the size of *A* is larger than *B*. The main reason for these deviations is that both Eqs. (4.8) and (4.12) do not take into account the effects of osmotic pressure gradient. The osmotic pressure gradient enhances the diffusion rate of *B* particles toward *A*, resulting in the enhancement of the reaction rate.

The rate enhancement effects of the osmotic pressure gradient and the reactive interference are multiplicative at least in the steady-state, as discussed above in the paragraph following Eq. (4.15). As observed by Dorsaz, et al. in Ref. 10, the rate enhancement due to the osmotic pressure gradient is differentiated depending on the size ratio of the reactants. Dorsaz, et al. found that for a given value of packing fraction the rate enhancement tends to approach a limiting value as the ratio σ_A / σ_B gets larger. On the other hand, as σ_B gets larger than σ_A, *B* particles start to form a nonequilibrium structure. This structure forms a kind of effective barrier for a *B* particle to go over to reach the central *A*, reducing the rate enhancement due to the osmotic pressure gradient.[10] We observe the same trend in

Figures 2.3 and 2.4 as noted by Dorsaz, et al.

The trend in the size ratio effect can be visualized more clearly for the steady-state rate constant. Figure 2.5 displays the dependence of the steady-state rate constant on the packing fraction of B and the reactant size ratio σ_A / σ_B. The simulation results are obtained by fitting the $\ln Y_A(t)$ vs. t curves by the function $at^{1/2} - k_f(\infty) C_B t$. Although the simulation results involve appreciable statistical errors, we can clearly see the trend. $k_f(\infty)$ increases with the packing fraction ϕ_B due to both the osmotic pressure gradient and the reactive interference among B's. We plot the theoretical curve, designated as $k_f(\text{Dorsaz}) / k_D$, representing the osmotic pressure gradient effect only as well as that calculated from Eq. (4.15), which takes account of the reactive interference effect as well. The difference between these two theoretical curves represents mainly the effect of the reactive interference.

Although the term inside the curly brackets of Eq. (4.15), representing the reactive interference effect, indicates some dependence on the size ratio σ_A / σ_B, it turns that the dependence is numerically negligible. We thus plot only one theoretical curve for Eq. (4.15) in the case with $\sigma_A / \sigma_B = 2$; the other curves with $\sigma_A / \sigma_B = 1$ and 0.5 are indistinguishable. However, the simulation results show clearly the dependence of $k_f(\infty)$ on the size ratio σ_A / σ_B. The rate is more enhanced as σ_A / σ_B gets larger. Indeed, this is the trend observed by Dorsaz, et al.[10] as mentioned above. For the reaction of the type $A + B \rightarrow A + P$, there is no

reactive interference effect. Therefore, the size ratio effect must arise from the difference in the relative mobility of *B* particles, as observed by Dorsaz, et al.

Figure 2.1. Time-dependent survival probability curves from BD simulations, theoretical expressions in Eqs. (4.8) and (4.12) of the present theory, and the simple Smoluchowski theory when $\phi_B = 0.0119$.

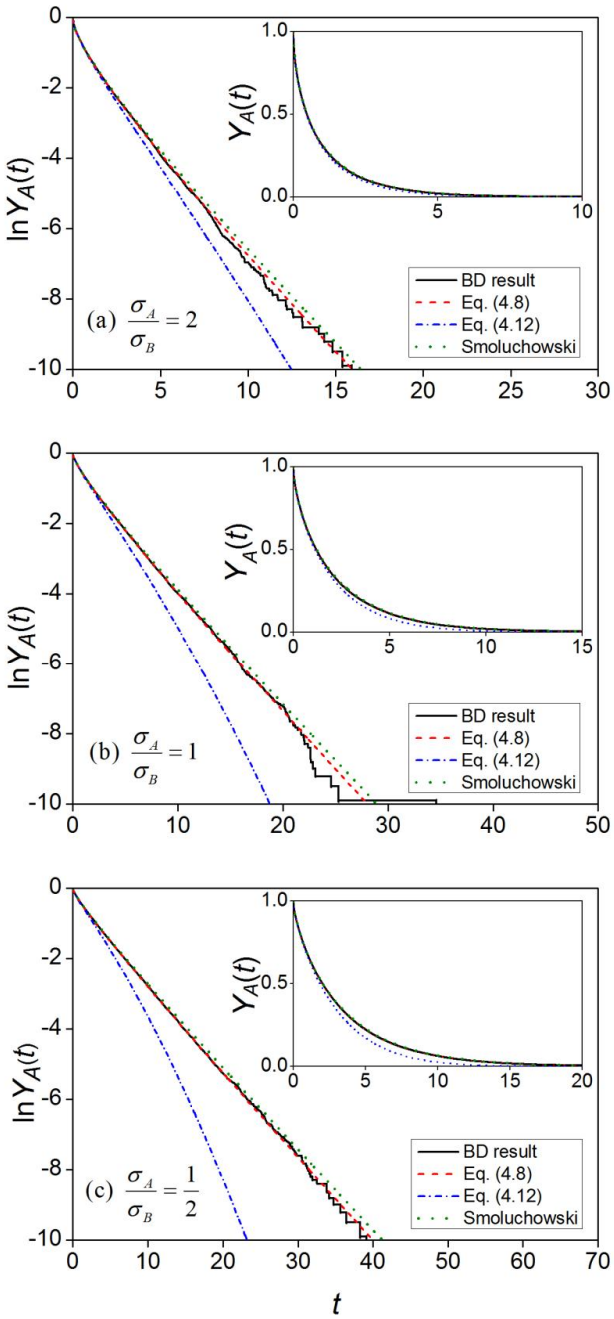

Figure 2.2. Time-dependent survival probability curves from BD simulations, theoretical expressions in Eqs. (4.8) and (4.12) of the present theory, and the simple Smoluchowski theory when $\phi_B = 0.0500$.

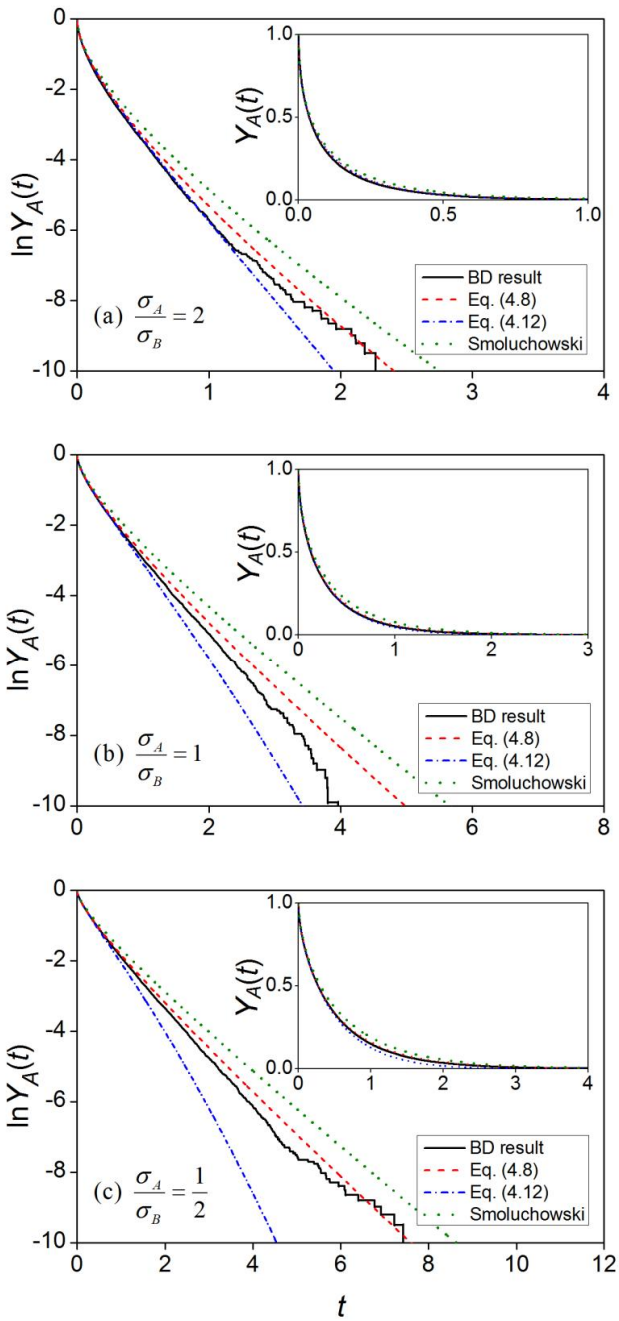

Figure 2.3. Time-dependent survival probability curves from BD simulations, theoretical expressions in Eqs. (4.8) and (4.12) of the present theory, and the simple Smoluchowski theory when $\phi_B = 0.113$.

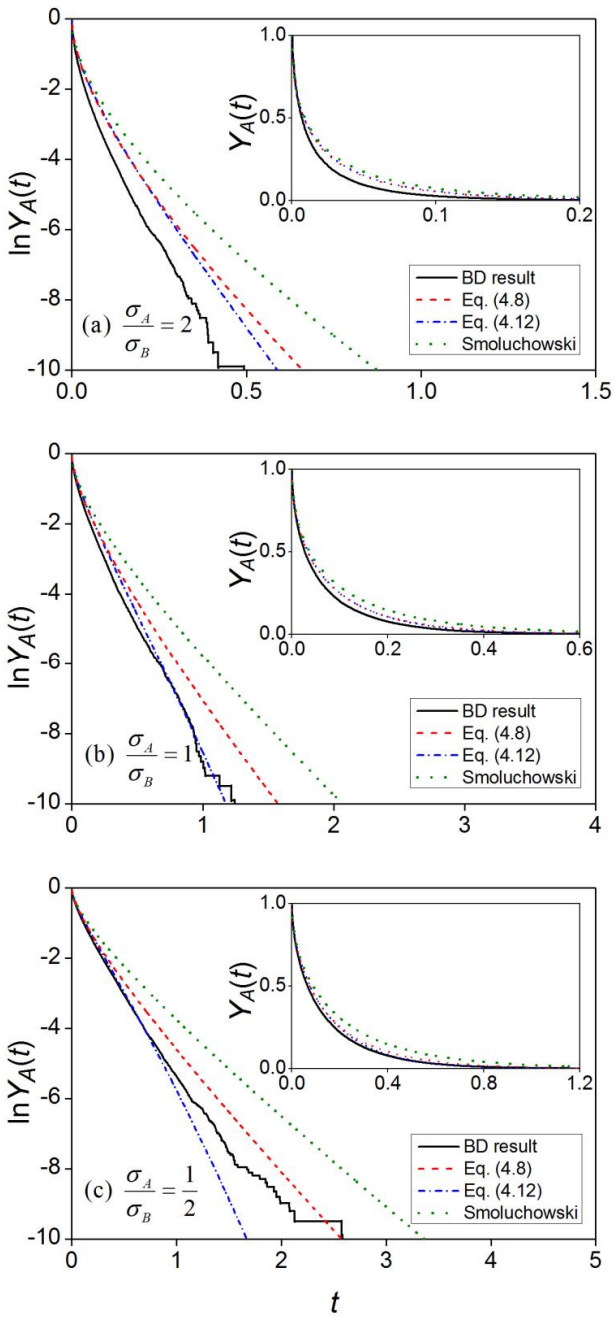

Figure 2.4. Time-dependent survival probability curves from BD simulations, theoretical expressions in Eqs. (4.8) and (4.12) of the present theory, and the simple Smoluchowski theory when $\phi_B = 0.197$.

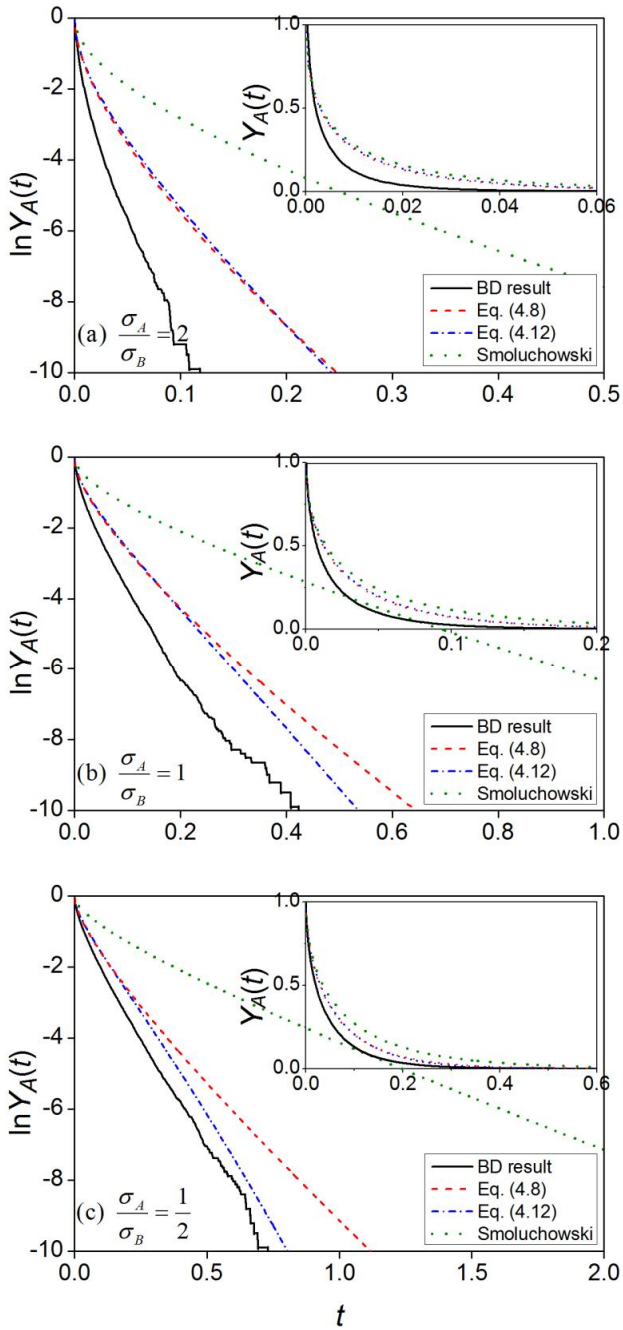

Figure 2.5. Steady-state rate constants calculated from BD simulations and the theory [Eq. (4.15)]. The rate constant values are scaled by the Smoluchowski rate constant, $k_D = 4\pi D_0 \sigma$.

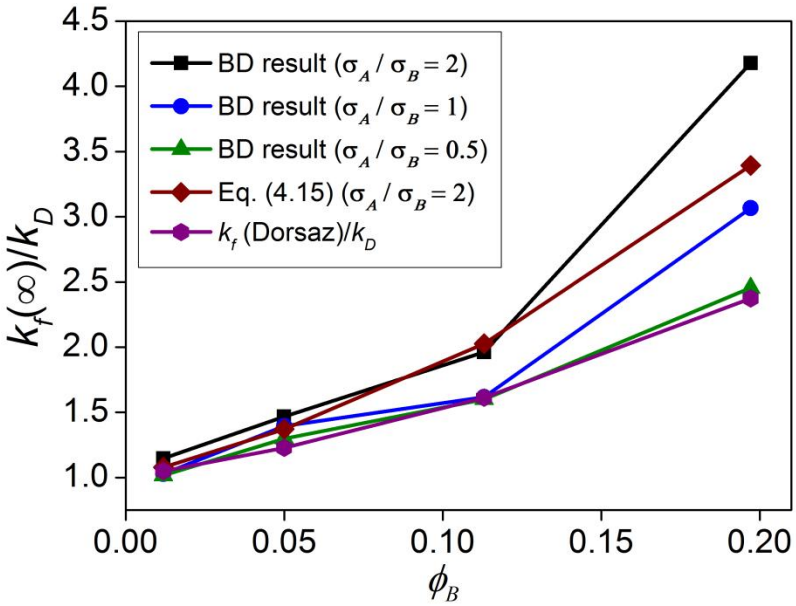

2.5. Conclusion

In this work, we have presented a refined theory of the kinetics of diffusion-influenced reactions of the type $A + B \rightarrow P + B$ with excess B's. The main focus of the present theory is the effects of B particle concentration on the rate coefficient. The interaction between B particles modifies the mobility of B particles toward A. In particular, as the reaction progresses, the B particle concentration is depleted near A so that an osmotic pressure gradient develops along the radial direction. This enhances the mobility of B particles toward A leading to the increase in the rate constant. Another subtle concentration effect present in the type of reactions under consideration is the reactive interference among B particles.

In Sec. II we have developed a general theoretical formalism for evaluating these reactant concentration effects. For the steady-state rate constant, an explicit expression [Eq. (4.15)] has been obtained that takes account of both effects of the osmotic pressure gradient and the reactive interference. However, for the time-dependent survival probability, we were able to obtain an explicit expression [Eq. (4.8)] that accounts for the reactive interference effect only. For the steady-state kinetics, we have found that the effects of the osmotic pressure gradient and the reactive interference are approximately multiplicative. Both enhance the reaction rate considerably as the B particle concentration increases.

The theory has been assessed against the BD simulation results. The time-dependent survival probability expression in Eq. (4.8) provides results that are in good agreement with simulations when the packing fraction of B particles is less than 0.05. However, as the B particle concentration gets higher, significant

deviations of the theoretical survival probability curves from the simulated ones are observed because the effect of osmotic pressure gradient has not been counted. The steady-state rate constant expression in Eq. (4.15) provides a reasonable explanation for the rate enhancement with increasing ϕ_B, but it still does not provide an adequate prediction on the differentiation of the rates depending on the reactant size ratio. Formulating a more complete theory of concentration effects on the transient rates as well as on the steady-state rates must be a challenging task that should be addressed in a future work.

Appendix: Derivation of eq. (4.15)

The $s \to 0$ limit of the Laplace transform of the diffusive propagator, $\hat{G}(r,0|r_0)$, satisfies the following equation:

$$-\frac{\delta(r-r_0)}{4\pi r_0^2} = \frac{D_0}{r^2}\frac{\partial}{\partial r} r^2 \Phi^s(r) \frac{\partial}{\partial r}\hat{G}(r,0|r_0) . \tag{A.1}$$

$\Phi^s(r)$ describes the effect of the steady-state osmotic pressure gradient,[8]

$$\Phi^s(r) = \frac{d[\beta\Pi(C_B^s(r))]}{dC_B^s(r)} \tag{A.2}$$

where $\beta = 1/k_BT$ and $C_B^s(r)$ is the steady-state number density field of B particles. The Carnahan-Starling equation of state[42] suggests that

$$\frac{\Pi(C_B^s(r))}{k_BT} = C_B^s(r)\frac{1+\phi_B(r)+[\phi_B(r)]^2-[\phi_B(r)]^3}{[1-\phi_B(r)]^3} \tag{A.3}$$

with the distance-dependent packing fraction, $\phi_B(r) = (4\pi/3)(\sigma_B/2)^3 C_B^s(r)$. This gives

$$\Phi^s(r) = \frac{1 + 4\phi_B(r) + 4[\phi_B(r)]^2 - 4[\phi_B(r)]^3 + [\phi_B(r)]^4}{[1-\phi_B(r)]^4} \tag{A.4}$$

The radial flux at $r = \sigma$ vanishes due to the reflecting boundary condition. Hence by multiplying both sides of Eq. (A.1) by $4\pi r^2$ and then integrating the resulting equation from $r = \sigma$ to $r = r_1$, we obtain

$$-\Theta(r_1 - r_0) = 4\pi D_0 r_1^2 \Phi^s(r_1) \frac{\partial}{\partial r_1} \hat{G}(r_1, 0|r_0), \tag{A.5}$$

where Θ denotes the Heaviside step function. Then, by dividing both sides of Eq. (A.5) by $4\pi D_0 r_1^2 \Phi^s(r_1)$ and integrating the resulting equation over r_1 from σ to ∞, we obtain

$$\hat{G}(\sigma, 0|r) = \frac{1}{4\pi D_0} \int_r^\infty dr_1 \frac{1}{r_1^2 \Phi^s(r_1)} \equiv \frac{1}{4\pi D_0 \tilde{r}}, \tag{A.6}$$

where we have noted that $\lim_{r_1 \to \infty} \hat{G}(r_1, 0|r_0) = 0$, and defined the tilded variable $\tilde{r}$ as the inverse of the integral.[32] For example, $\tilde{\sigma}^{-1} = \int_\sigma^\infty dr_1 [r_1^2 \Phi^s(r_1)]^{-1}$. From detailed balance condition,[43] $\hat{G}(r, 0|\sigma) = \hat{G}(\sigma, 0|r)$.

The steady-state rate constant is given by Eq. (4.13), which is reproduced here for easy reference,

$$k_f(\infty) = k_f^0(\infty) + \frac{C_B}{2\hat{G}(\sigma, 0|\sigma)} \int d\mathbf{r}\, v_B(r) \left[2\frac{\hat{G}(\sigma, 0|r)}{\hat{G}(\sigma, 0|\sigma)} - \frac{\hat{G}(\sigma, 0|r)}{\hat{G}(\sigma, 0|\sigma)} \frac{\hat{G}(r, 0|\sigma)}{\hat{G}(\sigma, 0|\sigma)} \right] \tag{A.7}$$

We note that $k_f^0(\infty) = [\hat{G}(\sigma, 0|\sigma)]^{-1} = 4\pi D_0 \tilde{\sigma}$ and this corresponds to the steady-state rate constant obtained by Dorsaz, et al.[10] for the reaction of the type $A + B \to A + P$ with excess B's, for which there is no reactive interference effect; that is

$$\frac{k_f^0(\infty)}{k_D} = \frac{\beta\Pi(C_B^s(\infty))}{C_B^s(\infty)} = \frac{1 + \phi_B + \phi_B^2 - \phi_B^3}{(1 - \phi_B)^3} \tag{A.8}$$

where $\phi_B = \phi_B(\infty) = (4\pi / 3)(\sigma_B / 2)^3 C_B$. Finally, with Eqs. (A.6) and (A.8), Eq. (A.7) can be rewritten as

$$\frac{k_f(\infty)}{k_D} = \frac{1 + \phi_B + \phi_B^2 - \phi_B^3}{(1 - \phi_B)^3} \left\{ 1 + C_B \int d\mathbf{r}\, v_B(r) \left[\frac{\tilde{\sigma}}{\tilde{r}} - \frac{1}{2} \left(\frac{\tilde{\sigma}}{\tilde{r}} \right)^2 \right] \right\}, \tag{A.8'}$$

which is Eq. (4.15) in the main text. In calculating the tilded variables, we need an expression for the steady-state number density field, $C_B^s(r)$, which may be approximated roughly as

$$C_B^s(r) \cong C_B \left[1 - \frac{\hat{G}(r, s|\sigma)}{\hat{G}(\sigma, s|\sigma)} \right] = C_B \left(1 - \frac{\tilde{\sigma}}{\tilde{r}} \right) \cong C_B \left(1 - \frac{\sigma}{r} \right) \tag{A.9}$$

References

1. S. A. Rice, *Diffusion-Limited Reactions* (Elsevier, Amsterdam, 1985).
2. E. Kotomin and V. Kuzovkov, *Modern Aspects of Diffusion-Controlled Reactions* (Elsevier, Amsterdam, 1996).
3. K. Allinger and A. Blumen, J. Chem. Phys. **72**, 4608 (1980).
4. M. Tachiya, Radiat. Phys. Chem. **21**, 167 (1983).
5. A. Szabo, J. Phys. Chem. **93**, 6929 (1989).
6. Y. Jung and S. Lee, J. Phys. Chem. A **101**, 5255 (1997).
7. J. Lee, J. Sung, and S. Lee, J. Chem. Phys. **113**, 8686 (2000).
8. J. K. G. Dhont, *An Introduction to Dynamics of Colloids* (Elsevier, Amsterdam, 1996).
9. J. Dzubiella and J. A. McCammon, J. Chem. Phys. **122**, 184902 (2005).
10. N. Dorsaz, C. De Michele, F. Piazza, P. De Los Rios, and G. Foffi, Phys. Rev. Lett. **105**, 120601 (2010).
11. F. Piazza, N. Dorsaz, C. De Michele, P. De Los Rios, and G. Foffi, J. Phys. Condens. Matter **25**, 375104 (2013).
12. A. Zaccone, N. Dorsaz, F. Piazza, C. De Michele, M. Morbidelli, and G. Foffi, J. Phys. Chem. B **115**, 7383 (2011).
13. R. Samson and J. M. Deutch, J. Chem. Phys. **67**, 847 (1977).
14. S. D. Traytak, Chem. Phys. Lett. **197**, 247 (1992); Chem. Phys. **193**, 351 (1995); J. Chem. Phys. **105**, 10860 (1996); Chem. Phys. Lett. **453**, 212 (2008).
15. G. Zoia and W. Strieder, J. Chem. Phys. **108**, 3114 (1998); W. Strieder and S. Saddawi, *ibid.* **113**, 10818 (2000); N. McDonald and W. Strieder, *ibid.* **118**,

4598 (2003).

16. H.-K. Tsao, J. Chem. Phys. **114**, 10247 (2001); Phys. Rev. E **66**, 011108 (2002).
17. J. Uhm, J. Lee, C. Eun, and S. Lee, J. Chem. Phys. **125**, 054911 (2006); Bull. Korean Chem. Soc. **27**, 1181 (2006).
18. A. Blumen and J. Manz, J. Chem. Phys. **71**, 4694 (1979).
19. A. Blumen, J. Chem. Phys. **72**, 2632 (1980).
20. Yu. H. Kalnin, Phys. Status Solidi B **101**, K139 (1980).
21. S. F. Swallen, K. Weidemaier, and M. D. Fayer, J. Phys. Chem. **99**, 1856 (1995).
22. S. F. Swallen and M. D. Fayer, J. Chem. Phys. **103**, 8864 (1995).
23. J. Sung and S. Lee, J. Chem. Phys. **111**, 796 (1999).
24. J. Sung, J. Chi, and S. Lee, J. Chem. Phys. **111**, 804 (1999).
25. J. Sung and S. Lee, J. Chem. Phys. **111**, 10159 (1999); **112**, 2128 (2000).
26. M. Litniewski, J. Chem. Phys. **123**, 124506 (2005); **124**, 114501 (2006); **125**, 174501 (2006); **127**, 034505 (2007); J. Phys. Condens. Matter **19**, 065110 (2007).
27. M. Litniewski and J. Gorecki, J. Chem. Phys. **134**, 244505 (2011).
28. K. Seki and M. Tachiya, Phys. Rev. E **80**, 041120 (2009).
29. K. Seki, M. Wojcik, and M. Tachiya, J. Chem. Phys. **134**, 094506 (2011).
30. K. Seki, M. Wojcik, and M. Tachiya, Phys. Rev. E **85**, 011131 (2012).
31. K. Seki, A. Ballal, and M. Tachiya, J. Phys. Chem. C **116**, 22086 (2012).
32. S. Lee, C. Y. Son, J. Sung, and S.-H. Chong, J. Chem. Phys. **134**, 121102

(2011).

33. C. Y. Son and S. Lee, J. Chem. Phys. **135**, 224512 (2011).

34. C. Y. Son, J. Kim, J.-H. Kim, J. S. Kim, and S. Lee, J. Chem. Phys. **138**, 164123 (2013).

35. S. Lee and M. Karplus, J. Chem. Phys. **86**, 1883 (1987); **96**, 1663(E) (1992).

36. J.-H. Kim and S. Lee, J. Chem. Phys. **131**, 014503 (2009).

37. D. L. Ermak and J. A. McCammon, J. Chem. Phys. **69**, 1352 (1978).

38. P. Strating, Phys. Rev. E **59**, 2175 (1999).

39. M. P. Allen and D. J. Tildesley, *Computer Simulation of liquids* (Clarendon, Oxford, 1987).

40. H. S. Carslaw and J. C. Jaeger, *Conduction of Heat in Solids,* 2nd ed. (Clarendon, Oxford, 1959).

41. M. Abramovitz and I. Stegun, *Handbook of Mathematical Functions with Formulas, Graphs, and Mathematical Tables* (Dover, New York, 1964).

42. N. F. Carnahan and K. E. Starling, J. Chem. Phys. **51**, 635 (1969).

43. C. W. Gardiner, *Handbook of Stochastic Methods*, 2nd ed. (Springer-Verlag, Berlin, 1985).

Chapter 3

3. Time-dependent electron transfer rate between geminate ions with strong Coulomb interaction and distance-dependent reactivity

3.1. Introduction

Electron transfer reactions following photoexcitation of a molecule provide an ideal model system for studying elementary reaction dynamics occurring in condensed phases. A detailed investigation of these reaction processes is also important to improve the efficiency of solar energy conversion and photocatalysis. Therefore, many studies have been carried out from both theoretical and experimental aspects.[1-20]

After photoexcitation a donor molecule transfers an electron to any one of the surrounding acceptor molecules that are usually present in excess. Then a back electron-transfer process between a geminate pair of the donor and acceptor molecules proceeds. The overall theoretical perspective of these processes was well described by Dorfman and M. D. Fayer.[13] In this work, we will just consider the back electron-transfer process between a geminate ion pair.

In a classical work published in 1938, Onsager derived an expression for the separation probability of a geminate ion pair, undergoing the Brownian motion in the presence of an external electric field as well as the attractive Coulomb interaction between the ions.[4] Hong and Noolandi[5,6] obtained an exact time-

dependent solution to the Onsager problem in the absence of the external electric field, but with the generalization to the case of finite recombination rate at nonzero reaction radius. They also obtained an exact expression for the long-time separation probability of the geminate ions in the presence of the external electric field.[7] However, their solution is too complicated for practical use, so that the problem has been reconsidered with various mathematical methods.[8-12,21-25]

The previous analytic expressions for the time-dependent electron-transfer rate and the charge separation probability were obtained only for the case where the reaction can be assumed to occur at a contact separation. Although Wilemski and Fixman[43] proposed a general method for treating the diffusion-influenced reactions with distance-dependent reactivity, an accurate and practical expression for the charge recombination rate is still lacking. The Wilemski-Fixman method requires a Green's function expression for the Smoluchowski equation with the drift term due to the Coulomb potential. Hong and Noolandi[6] obtained an exact expression for the Green's function but it is too complicated for practical use, as mentioned above.

In this work, we employ the recently proposed solution method[21,22] for Fredholm integral equations of the second kind to derive a very accurate time-dependent solution to the Onsager problem with the account of the distance-dependent reactivity. We also consider the dependence of the solution on the initial separation between the geminate ions. However, due to the mathematical complexity, we do not include the effect of an external electric field in the present work. A closed-form analytic expressions for the time-dependent charge recombination rate and the

survival probability of the geminate ion pair are presented, which are accurate enough for most reasonable parameter values.

3.2. Theory

3.2.1. Reaction model

We consider the electron transfer reaction between a geminate pair of ions that are generated initially at a distance r_0. We assume that relative motion of the ions can be described by the Smoluchowski equation. The rate of electron transfer between the ions at a separation r is described by the Marcus theory as[27]

$$S_R(r) = \frac{2\pi}{\hbar} \frac{|V|^2}{(4\pi\lambda k_B T)^{1/2}} \exp\left(-\frac{(\Delta G + \lambda)^2}{4\lambda k_B T} \right). \quad (1)$$

Here V is the matrix element of the interaction Hamiltonian between the donor state and the acceptor state, which depends very sharply on the distance between the donor and acceptor. The following functional form is usually assumed for the distance dependence of V:

$$|V|^2 = |V_0|^2 e^{-\alpha(r-\sigma)} \quad (2)$$

with V_0 denoting the coupling at the contact distance σ. ΔG is the free energy difference, and λ is the solvent reorganization energy. Both ΔG and λ also depend on r.[2,3,19,28] The distance dependence of ΔG is determined largely by the Coulomb interaction[3] as

$$\Delta G = \Delta G_\infty + \zeta e^2 / (\varepsilon_s r), \quad (3)$$

where ΔG_∞ is the free energy change at infinite separation of reactants and ε_s is

the static dielectric constant. ζ is +1 for an electron transfer between ions and -1 for that between neutral reactants. Neglecting the contribution from the intramolecular modes, the reorganization energy λ is often approximated as[3,29]

$$\lambda = \frac{e^2}{2}\left(\frac{1}{\varepsilon_\infty} - \frac{1}{\varepsilon_s}\right)\left(\frac{1}{r_D} + \frac{1}{r_A} - \frac{2}{r}\right) \tag{4}$$

where ε_∞ denotes the optical dielectric constant, and r_D and r_A are the radii of donor and acceptor, respectively. With the shorthand notation defined by $\nu = \pi^{1/2}\left|V_0\right|^2/(\hbar k_B T)$, $\bar{\lambda} = \lambda / k_B T$, and $A = \Delta G/(k_B T) + \bar{\lambda}$, the reaction sink function $S_R(r)$ can be rewritten as

$$S_R(r) = \nu\bar{\lambda}^{-1/2} e^{-A^2/(4\bar{\lambda})} e^{-\alpha(r-\sigma)}. \tag{5}$$

For the above model of reaction and transport, we can write down the time-evolution equation for the probability density of finding unreacted reactant pair at a separation *r* at time *t*, given that their initial separation was r_0, as

$$\frac{\partial P(r,t|r_0)}{\partial t} = D\frac{1}{r^2}\frac{\partial}{\partial r} r^2 h(r) e^{-U(r)} \frac{\partial}{\partial r} e^{U(r)} P(r,t|r_0) - S_R(r) P(r,t|r_0). \tag{6}$$

The initial and the boundary conditions are given by

$$P(r,t=0|r_0) = \frac{\delta(r-r_0)}{4\pi r_0^2}, \quad \frac{\partial}{\partial r} e^{U(r)} P(r,t|r_0)\Big|_{r=\sigma} = 0,$$

$$\lim_{r\to\infty} P(r,t|r_0) = 0. \tag{7}$$

In Eqs. (6) and (7), $U(r)$ denotes the interaction potential in units of $k_B T$ (k_B and T are Boltzmann's constant and the absolute temperature). D denotes the

relative diffusion constant, and $h(r)$ accounts for the effect of hydrodynamic interaction on the relative motion of ions.

The quantity of interest is the survival probability $W(r_0,t)$ that the geminate ion pair has not undergone the electron transfer reaction until time *t*, irrespective of their separation. $W(r_0,t)$ is related to $P(r,t|r_0)$ as

$$W(r_0,t) = 4\pi \int_\sigma^\infty dr\, r^2 P(r,t|r_0)\,. \tag{8}$$

Instead of solving Eqs. (6) – (8), one may solve directly the equation for the survival probability, which can be derived from the adjoint equation of the Smoluchowski equation in Eq. (6).[7-9] It is given by

$$\frac{\partial}{\partial t} W(r_0,t) = De^{U(r_0)} \frac{1}{r_0^2} \frac{\partial}{\partial r_0} r_0^2 h(r_0) e^{-U(r_0)} \frac{\partial}{\partial r_0} W(r_0,t) - S_R(r_0) W(r_0,t)\,. \tag{9}$$

For an analytic manipulation, it is more convenient to consider the equation for the geminate reaction probability, $X(r,t) = 1 - W(r,t)$:

$$\frac{\partial}{\partial t} X(r,t) = De^{U(r)} \frac{1}{r^2} \frac{\partial}{\partial r} r^2 h(r) e^{-U(r)} \frac{\partial}{\partial r} X(r,t) - S_R(r) X(r,t) + S_R(r)\,. \tag{10}$$

In Eq. (10), we have chosen to use *r* rather than r_0 as an independent variable for the brevity of notation. The initial and boundary conditions are given by

$$X(r,t=0) = 0; \qquad \lim_{r\to\infty} X(r,t) = 0; \qquad \frac{\partial}{\partial r} X(r,t)\bigg|_{r=\sigma} = 0\,. \tag{11}$$

Once the geminate reaction probability is determined, the geminate reaction rate, $R(r,t)$, is given by $R(r,t) = dX(r,t)/dt$.

3.2.2. A quick derivation of Wilemski-Fixman-Weiss theory

By taking the Laplace transformation of Eq. (6), we get

$$s\hat{P}(r,s|r_0)-\frac{\delta(r-r_0)}{4\pi r_0^2}.$$

$$=D\frac{1}{r^2}\frac{\partial}{\partial r}r^2h(r)e^{-U(r)}\frac{\partial}{\partial r}e^{U(r)}\hat{P}(r,s|r_0)-S_R(r)\hat{P}(r,s|r_0) \qquad (12)$$

We denote the Laplace transform of a function $f(t)$ by $\hat{f}(s)$. Equation (12) can be rewritten as an integral equation given by

$$\hat{P}(r,s|r_0)=\hat{G}(r,s|r_0)-4\pi\int_\sigma^\infty dr_1\, r_1^2\hat{G}(r,s|r_1)S_R(r_1)\hat{P}(r_1,s|r_0), \qquad (13)$$

where $\hat{G}(r,s|r_0)$ is the Green's function for the Smoluchowski equation in the absence of reaction. With the detailed balance conditions,[30] $\hat{P}(r,s|r_0)e^{-U(r_0)}=\hat{P}(r_0,s|r)e^{-U(r)}$ and $\hat{G}(r,s|r_0)e^{-U(r_0)}=\hat{G}(r_0,s|r)e^{-U(r)}$, Eq. (13) can be rewritten as

$$\hat{P}(r_0,s|r)=\hat{G}(r_0,s|r)-4\pi\int_\sigma^\infty dr_1\, r_1^2\hat{G}(r_1,s|r)S_R(r_1)\hat{P}(r_0,s|r_1). \qquad (14)$$

The survival probability is given by $\hat{W}(r,s)=4\pi\int_\sigma^\infty dr_0\, r_0^2\hat{P}(r_0,s|r)$. Hence, from Eq. (14), we get an integral equation for the geminate reaction probability, $\hat{X}(r,s)=s^{-1}-\hat{W}(r,s)$, as

$$\hat{X}(r,s)=s^{-1}4\pi\int_\sigma^\infty dr_1\, r_1^2\hat{G}(r_1,s|r)S_R(r_1)$$

$$-4\pi\int_\sigma^\infty dr_1\, r_1^2\hat{G}(r_1,s|r)S_R(r_1)\hat{X}(r_1,s). \qquad (15)$$

This gives a formally exact expression for $\hat{X}(r,s)$ given by[21,22]

$$\hat{X}(r,s)=\frac{1}{s}\frac{4\pi\int_{\sigma}^{\infty}dr_1\,r_1^2S_R(r_1)\hat{G}(r_1,s|r)}{1+4\pi\int_{\sigma}^{\infty}dr_1\,r_1^2S_R(r_1)\hat{G}(r_1,s|r)\hat{X}(r_1,s)/\hat{X}(r,s)}. \tag{16}$$

A simple estimate for the raio, $\hat{X}(r_1,s)/\hat{X}(r,s)$, in Eq. (16) can be given by

$$\frac{\hat{X}(r_1,s)}{\hat{X}(r,s)}=\frac{\hat{R}(r_1,s)}{\hat{R}(r,s)}=\frac{4\pi\int_{\sigma}^{\infty}dr_2\,r_2^2S_R(r_2)\hat{P}(r_2,s|r_1)}{4\pi\int_{\sigma}^{\infty}dr_2\,r_2^2S_R(r_2)\hat{P}(r_2,s|r)}$$

$$\cong\frac{4\pi\int_{\sigma}^{\infty}dr_2\,r_2^2S_R(r_2)\hat{G}(r_2,s|r_1)}{4\pi\int_{\sigma}^{\infty}dr_2\,r_2^2S_R(r_2)\hat{G}(r_2,s|r)} \tag{17}$$

Apparently, this is an approximation that is valid only when the reactivity is small so that the depletion of $\hat{P}(r_2,s|r)$ in the reaction zone is not so significant. However, we note that the error would be partially offset because it enters as a ratio. With Eq. (17), we obtain the following approximate expression for the geminate reaction probability:

$$\hat{X}(r,s)\cong\hat{X}^{WFW}(r,s)=\frac{1}{s}\frac{J_1(r,s)}{1+J_2(r,s)/J_1(r,s)}, \tag{18}$$

where $J_1(r,s)$ and $J_2(r,s)$ are defined by

$$J_1(r,s)=4\pi\int_{\sigma}^{\infty}dr_1\,r_1^2S_R(r_1)\hat{G}(r_1,s|r), \tag{19}$$

$$J_2(r,s)=4\pi\int_{\sigma}^{\infty}dr_1\,r_1^2S_R(r_1)\hat{G}(r_1,s|r)J_1(r_1,s). \tag{20}$$

Equation (18) was first obtained by Weiss[31] through a perturbation analysis of the

Wilemski-Fixman theory of diffusion-controlled reactions[26] (see also Ref. 20).

We have a general expression of $\hat{G}(r,s|r_0)$ for arbitrary $U(r)$ and $h(r)$ that are accurate for intermediate to small values of s.[21] However, to calculate the time-dependent survival probability, we need an accurate, but not too complicated expression of $\hat{G}(r,s|r_0)$ for intermediate to large values of s, which is not available for the present. Therefore, the utility of Eq. (18) is restricted to the long-time regime. In the interaction-free case with $U(r)=0$ and $h(r)=1$ for $r \geq \sigma$, an exact expression for $\hat{G}(r,s|r_0)$ is given by[1]

$$\hat{G}_0(r,s\,|\,r_0)=\frac{1}{8\pi D\zeta r r_0}\left[e^{-\zeta|r-r_0|}+\frac{\sigma\zeta-1}{\sigma\zeta+1}e^{-\zeta(r+r_0-2\sigma)}\right] \tag{21}$$

where $\zeta=\sqrt{s/D}$. Hence the Wilemski-Fixman-Weiss (WFW) expression for the geminate reaction probability in Eq. (18) is most useful for calculating the electron-transfer rate between neutral reactants.

3.2.3. A new expression for $\hat{X}(r,s)$

First, we take the Laplace transfromation of Eq. (10). We have

$$s\hat{X}(r,s)=De^{U(r)}\frac{1}{r^2}\frac{\partial}{\partial r}r^2h(r)e^{-U(r)}\frac{\partial}{\partial r}\hat{X}(r,s)$$

$$-S_R(r)\hat{X}(r,s)+\frac{1}{s}S_R(r)\,. \tag{22}$$

Multiplying Eq. (22) by $D^{-1}e^{-U(r)}r^2$ and integrating the resulting equation over r from σ to r_1, we get

$$\frac{s}{D}\int_{\sigma}^{r_1} dr_2\, r_2^2 e^{-U(r_2)}\hat{X}(r_2,s) = r_1^2 h(r_1) e^{-U(r_1)}\frac{\partial}{\partial r_1}\hat{X}(r_1,s)$$

$$-\frac{1}{D}\int_{\sigma}^{r_1} dr_2\, r_2^2 e^{-U(r_2)} S_R(r_2)\hat{X}(r_2,s) + \frac{1}{Ds}\int_{\sigma}^{r_1} dr_2\, r_2^2 e^{-U(r_2)} S_R(r_2) \tag{23}$$

To obtain Eq. (23), we have used the inner boundary condition in Eq. (11). Then, by multiplying Eq. (23) by $r_1^{-2}h(r_1)^{-1}e^{U(r_1)}$ and integrating the resulting equation over r_1 from r to infinity, we get

$$\hat{X}(r,s) = \frac{1}{Ds}\int_{r}^{\infty} dr_1 \frac{e^{U(r_1)}}{r_1^2 h(r_1)}\int_{\sigma}^{r_1} dr_2\, r_2^2 e^{-U(r_2)} S_R(r_2)$$

$$-\frac{1}{D}\int_{r}^{\infty} dr_1 \frac{e^{U(r_1)}}{r_1^2 h(r_1)}\int_{\sigma}^{r_1} dr_2\, r_2^2 e^{-U(r_2)} S_R(r_2)\hat{X}(r_2,s)$$

$$-\frac{s}{D}\int_{r}^{\infty} dr_1 \frac{e^{U(r_1)}}{r_1^2 h(r_1)}\int_{\sigma}^{r_1} dr_2\, r_2^2 e^{-U(r_2)}\hat{X}(r_2,s) \tag{24}$$

To obtain Eq. (24), we have used the outer boundary condition in Eq. (11). Finally, by introducing the Flannery transformation,[32]

$$\tilde{r}(r) \equiv \left[\int_{r}^{\infty} dr_1 \frac{e^{U(r_1)}}{r_1^2 h(r_1)}\right]^{-1}, \tag{25}$$

and carrying out the integrations by parts for the three double integral terms on the right hand side of Eq. (24), we get

$$\hat{X}(r,s) = \frac{1}{Ds}\int_{\sigma}^{\infty} dr_1 \frac{r_1^2 e^{-U(r_1)}}{\max(\tilde{r},\tilde{r}_1)} S_R(r_1)$$

$$-\frac{s}{D}\int_{\sigma}^{\infty} dr_1 \frac{r_1^2 e^{-U(r_1)}}{\max(\tilde{r},\tilde{r}_1)}\hat{X}(r_1,s) - \frac{1}{D}\int_{\sigma}^{\infty} dr_1 \frac{r_1^2 e^{-U(r_1)}}{\max(\tilde{r},\tilde{r}_1)} S_R(r_1)\hat{X}(r_1,s)\,. \tag{26}$$

As mentioned above, an exact Laplace-tranform expression of the Green's function, $\hat{G}(r,s|r_0)$, for the Smoluchowki equation with arbitrary $U(r)$ and $h(r)$ is not known, but an asymptotic expression that is exact up to first order in $\zeta(=\sqrt{s/D})$ is given by[1,12,21]

$$\hat{G}(r_1,s|r) = G_s(r_1,r) - \frac{e^{-U(r_1)}}{4\pi D}\zeta + O(\zeta^2) \tag{27}$$

where $G_s(r_1,r)$ is

$$G_s(r_1,r) = \hat{G}(r_1,s=0|r) = e^{-U(r_1)}\frac{\tilde{r}_1 + \tilde{r} - |\tilde{r}_1 - \tilde{r}|}{8\pi D\tilde{r}_1\tilde{r}} = \frac{e^{-U(r_1)}}{4\pi D\max(\tilde{r}_1,\tilde{r})}. \tag{28}$$

With Eq. (28), Eq. (26) can be rewritten as

$$\hat{X}(r,s) = \frac{1}{s}4\pi\int_\sigma^\infty dr_1\, r_1^2 G_s(r_1,r)S_R(r_1)$$

$$-4\pi\int_\sigma^\infty dr_1\, r_1^2 G_s(r_1,r)\left[s + S_R(r_1)\right]\hat{X}(r_1,s). \tag{29}$$

This is a Fredholm integral equation of the second kind, which we now have to solve.

As introduced in Refs. 21 and 22, an efficient solution method for integral equations of this type is first to write a formally exact solution of the form,

$$\hat{X}(r,s) = \frac{1}{s}\frac{4\pi\int_\sigma^\infty dr_1\, r_1^2\hat{G}_s(r_1,r)S_R(r_1)}{1 + 4\pi\int_\sigma^\infty dr_1\, r_1^2\hat{G}_s(r_1,r)\left[s + S_R(r_1)\right]\hat{X}(r_1,s)/\hat{X}(r,s)}. \tag{30}$$

To get an explicit solution, we then have to find an approximate expression for the ratio, $\hat{X}(r_1,s)/\hat{X}(r,s)$. Because the geminate reaction usually occurs very quickly,

a short-time (large-s) approximation for $\hat{X}(r,s)$ would be useful to evaluate the ratio. The errors due to the use of such approximations for $\hat{X}(r,s)$ and $\hat{X}(r_1,s)$ are expected to be partially cancelled out because they enter as a ratio in Eq. (30).

In the Appendix, we provide a derivation of a large-s expression for $\hat{X}(r,s)$. The large-s expression $\hat{X}^{(0)}(r,s)$ in Eq. (A11) can be used to evaluate the ratio $\hat{X}(r_1,s)/\hat{X}(r,s)$ in Eq. (30) to get an improved estimate of $\hat{X}(r,s)$ as given by

$$\hat{X}^{(1)}(r,s)=\frac{1}{s}\frac{4\pi\int_{\sigma}^{\infty}dr_1\,r_1^2\hat{G}_s(r_1,r)S_R(r_1)}{1+4\pi\int_{\sigma}^{\infty}dr_1\,r_1^2\hat{G}_s(r_1,r)\left[s+S_R(r_1)\right]\hat{X}^{(0)}(r_1,s)/\hat{X}^{(0)}(r,s)}. \tag{31}$$

By iteration, one may obtain further improved results but with increasing computational cost. Once $\hat{X}(r,s)$ is given, the geminate electron-transfer rate $R(r,t)$ and the survival probability $W(r,t)$ can be calculated from the following Laplace transform expressions:

$$\hat{R}(r,s)=s\hat{X}(r,s), \tag{32}$$

$$\hat{W}(r,s)=s^{-1}-\hat{X}(r,s). \tag{33}$$

The inverse Laplace transformation can be carried out very efficiently by using the Stehfest algorithm.[33] In Sec. III, we will see that Eqs. (31) and (33) provide accurate results for the time-dependent survival probability of the geminate ion pair for all reasonable parameter values up to the time when $R(r,t)$ becomes almost zero and thus $W(r,t)$ reaches an almost plateau value.

3.2.4. Long-time expression for $\hat{X}(r,s)$

We now provide an expression for $W(r,t)$ that is asymptotically correct at long times. The derivation is based on the WFW expression for $\hat{X}(r,s)$ in Eq. (18). For the general case with arbitrary $U(r)$ and $h(r)$, an asymptotic expression of $\hat{G}(r,s|r_0)$ that is exact up to first order in $\zeta\ (=\sqrt{s/D})$ is given by Eq. (27). Then, with Eqs. (18) and (27), it can be shown that the survival probability of the geminate ion at long times is given by

$$W(r,t) \cong W_u(r) + \frac{A(r)}{(\pi D t)^{1/2}}. \tag{34}$$

Here, $W_u(r)$ is the ultimate survival probability, $W(r,\infty)$, that is given by

$$W_u(r) = 1 - \frac{K_1(r)}{1 + K_2(r)/K_1(r)} \tag{35}$$

with

$$K_1(r) = J_1(r,0) = 4\pi \int_\sigma^\infty dr_1\, r_1^2 S_R(r_1) G_s(r_1,r), \tag{36}$$

$$K_2(r) = J_2(r,0) = 4\pi \int_\sigma^\infty dr_1\, r_1^2 S_R(r_1) G_s(r_1,r) K_1(r_1). \tag{37}$$

In Eq. (34), $A(r)$ is given by

$$A(r) \equiv \frac{X_u(r)}{4\pi D}\left\{\frac{2\kappa_{eq}}{K_1(r)} - \frac{K_3 + \kappa_{eq}[1+K_1(r)]}{K_1(r)+K_2(r)}\right\} \tag{38}$$

where $X_u(r)[=1-W_u(r)]$ is the ultimate recombination probability. κ_{eq} and K_3 are constants given by

$$\kappa_{eq} \equiv 4\pi \int_{\sigma}^{\infty} dr\, r^2 S_R(r) e^{-U(r)} \tag{39}$$

$$K_3 \equiv 4\pi \int_{\sigma}^{\infty} dr\, r^2 S_R(r) e^{-U(r)} K_1(r) \tag{40}$$

Note that κ_{eq} is an equilibrium rate constant for bulk recombination.

3.3. Results and discussion

3.3.1. Characterization of the model sink function in Eq. (5)

The distance-dependence of the dimensionless variables $\bar{\lambda}$ and A in Eq. (5) can be expressed as

$$\bar{\lambda} \equiv \frac{\lambda}{k_B T} = c_0 \left(\gamma - \frac{2\sigma}{r} \right) \tag{41}$$

$$A \equiv \frac{\Delta G + \lambda}{k_B T} = \frac{\Delta G_\infty}{k_B T} + c_0 \gamma + c_1 \frac{\sigma}{r} \tag{42}$$

where γ, c_0, and c_1 are dimensionless constants defined by

$$\gamma \equiv \frac{\sigma}{r_D} + \frac{\sigma}{r_A}, \quad c_0 \equiv \frac{r_c}{2\sigma} \left(\frac{\varepsilon_s}{\varepsilon_\infty} - 1 \right), \quad c_1 \equiv \frac{r_c}{\sigma} \left[(\zeta + 1) - \frac{\varepsilon_s}{\varepsilon_\infty} \right], \tag{43}$$

and r_c is the Onsager distance defined by $r_c = e^2 / (\varepsilon_s k_B T)$. Note that if $r_D = r_A = \sigma / 2$, $\gamma = 4$ and this value will be assumed for γ hereafter.

In a polar solvent with $\varepsilon_s \cong 35$ and $\varepsilon_\infty \cong 2.5$, $r_c \cong 16$ Å. Hence, if $\sigma \cong 10$ Å, $r_c / \sigma \cong 1.6$ and $c_0 \cong 10$. For an electron transfer between ions $c_1 \cong -19$, while for an electron transfer between neutral reactants $c_1 \cong -22$. We thus have

$$\bar{\lambda} \cong 10(4 - 2\sigma / r),$$

$$A \cong \frac{\Delta G_\infty}{k_B T} + 40 - 19 \times \frac{\sigma}{r} \quad \text{(for an electron transfer between ions),}$$

$$A \cong \frac{\Delta G_\infty}{k_B T} + 40 - 22 \times \frac{\sigma}{r} \quad \text{(for an electron transfer between neutral reactants).}$$

(44)

When $\Delta G_\infty = 0$, $\bar{\lambda} \cong 20$ and $A \cong 20$ at $r = \sigma$.

On the other hand, in a nonpolar solvent with $\varepsilon_s \cong 4$ and $\varepsilon_\infty \cong 2.5$, $r_c \cong 140$ Å. Hence, if $\sigma \cong 10$ Å, $r_c / \sigma \cong 14$ and $c_0 \cong 4.2$. For an electron transfer between ions $c_1 \cong 5.6$, while for an electron transfer between neutral reactants $c_1 \cong -22$. We thus have

$$\bar{\lambda} \cong 4.2\left(4 - 2\sigma / r\right),$$

$$A \cong \frac{\Delta G_\infty}{k_B T} + 16.8 + 5.6 \times \frac{\sigma}{r} \quad \text{(for an electron transfer between ions),}$$

$$A \cong \frac{\Delta G_\infty}{k_B T} + 16.8 - 22 \times \frac{\sigma}{r} \quad \text{(for an electron transfer between neutral reactants).}$$

(45)

When $r = \sigma$ and $\Delta G_\infty = 0$, $\bar{\lambda} \cong 8.4$ while $A \cong 20$ and -5 for ionic and neutral reactants, respectively.

The parameter α in Eq. (5) is roughly the inverse of the electron tunneling distance, which is about 1 Å.[2,3,15,16] The value of the parameter ν varies more specifically depending on the reaction system. In the model calculations described below, we will vary the value of $\nu[\bar{\lambda}(\sigma)]^{-1/2}$ from 10 to 10^3 in units of

D/σ^2 .[2,15] Note that in all calculations described in Sec. IIIB we use the dimensionless variables: length in σ, time in σ^2/D, and energy in k_BT. We will assume the value of σ to be 10 Å.

Following the work of Tachiya and Murata,[28] we display the distance-dependence of the reaction sink function in Fig. 3.1. Figures 3.1(a) and 3.1(b) display characteristic variations of $S_R(r)$ for the electron-transfer between ions and neutral reactants in common polar solvents, respectively, while Figs. 3.1(c) and 1(d) are for the electron-transfer between ions and neutral reactants in common nonpolar solvents, respectively. The five curves in each of these figures are for differing values of ΔG_∞ in eV, as indicated by the numbers on the respective curves.

From Figs. 3.1(a) and 3.1(b), we see that for the electron transfers in polar solvents with $\varepsilon_s \cong 35$, we may approximate the sink function as an exponentially decaying function,

$$S_R(r) = \kappa e^{-\alpha(r-\sigma)}. \tag{46}$$

Also, for the electron transfers in nonpolar solvents with $\varepsilon_s \cong 4$, if ΔG_∞ is smaller than -4 eV for the reaction between ions or if ΔG_∞ is larger than 2 eV for the reaction between neutral reactants, we may use the exponential sink function. We will thus evaluate the accuracy of the theoretical expressions first for the case with the exponential sink function in Eq. (46), and then for the more complicated cases as depicted in Figs. 3.1(c) and 3.1(d).

Figure 3.1. Characteristic distance-dependence of $S_R(r)$ for the electron transfers between ions in polar solvents [Fig. 3.1(a)], between neutral reactants in polar solvents [Fig. 3.1(b)], between ions in nonpolar solvents [Fig. 3.1(c)], and between neutral reactants in nonpolar solvents [Fig. 3.1(d)]. See Eqs. (5), (44), and (45) for detailed description. We set the values of $\nu[\bar{\lambda}(\sigma)]^{-1/2}/(D/\sigma^2)$ and $\alpha\sigma$ to 10^3 and 10, respectively. Figures 3.1(e) and 3.1(f) display the dependence of $S_R(\sigma)$ on ΔG_∞ for the electron transfers between ions and between neutral reactants, respectively, in nonpolar solvents. Figure 3.1(f) displays the behavior typical to the Marcus inverted region.

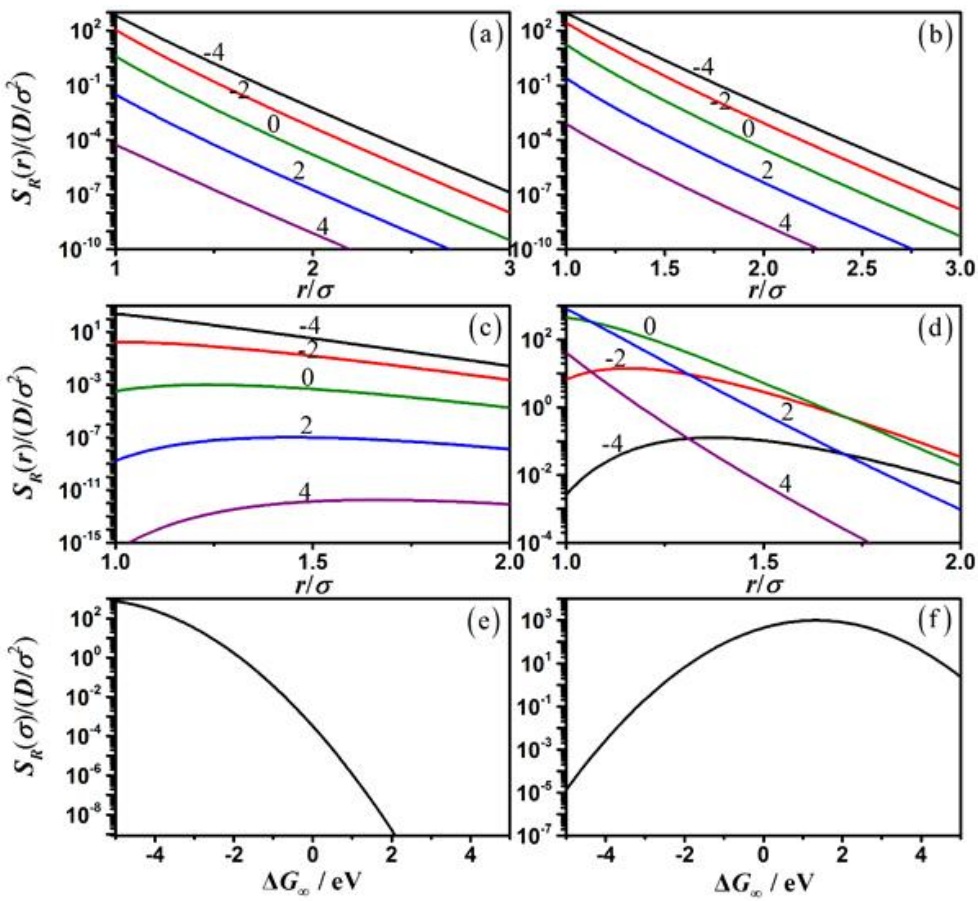

3.3.2. Results with the exponential sink function in Eq. (46)

We have evaluated the accuracy of the analytic expressions for the geminate reaction probability given in Sec. II against the full numerical results obtained by solving Eq. (9) for the survival probability of the geminate reactant pairs. The geminate reaction probability is related to the survival probability by Eq. (33). In this subsection, we will assume that the sink function is given by Eq. (46). When the experimental results are analyzed by using Eq. (46) as the reaction model, the values of α and κ determined thereby may be slightly different from the corresponding quantities in Eq. (5) even if the same experimental data are used in the respective analysis. Nevertheless, in the calculations described below, we will use the input value of κ as estimated from the relation $\kappa = \nu[\bar{\lambda}(\sigma)]^{-1/2} e^{-[A(\sigma)]^2/[4\bar{\lambda}(\sigma)]}$, for the sake of convenience.

For the electron transfer between ions with $U(r) = -r_c / r$, the approximate expression $\hat{X}^{(1)}(r,s)$ of the geminate reaction probability in Eq. (31) is evaluated with the zeroth-order expression $\hat{X}^{(0)}(r,s)$ in Eq. (A11). The inverse Laplace transformation is then carried out numerically by using the Stehfest algorithm.[33]

For the sake of simplicity, we will neglect the effect of hydrodynamic interaction hereafter; that is, we will take $h(r)$ to be unity at all separations. When $h(r) = 1$, $\hat{G}_h(r,s|r_0)$ defined in Eq. (A4) is given by $\hat{G}_0(r,s|r_0)$ whose explicit expression is given in Eq. (21). When $h(r) = 1$ and $U(r) = -r_c / r$, the Flannery transformed distance variable $\tilde{r}(r)$, defined by Eq. (25) and appearing in

the expression of $G_s(r_1,r)$ in Eq. (28), is given by

$$\tilde{r}(r) = r_c / (1 - e^{-r_c/r}), \tag{47}$$

and $M(r,s|\sigma)$, which is defined in Eq. (A8) and appears in the expression of $\hat{X}^{(0)}(r,s)$ in Eq. (A11), is given by

$$M(r,s|\sigma) = \frac{r_c\, e^{-\zeta(r-\sigma)}}{r(1+\zeta\sigma)}. \tag{48}$$

With the exponential sink function in Eq. (46), the integral $I_1(r,s)$, which is defined in Eq. (A7) and appears in the expression of $\hat{X}^{(0)}(r,s)$, can be calculated analytically. We have

$$I_1(r,s) = \frac{\kappa}{Dr(\zeta^2-\alpha^2)^2}\Big\{[(\zeta^2-\alpha^2)r - 2\alpha]\mathrm{e}^{-\alpha(r-\sigma)} + \alpha[2 + 2\alpha\sigma - (\zeta^2-\alpha^2)\sigma^2]\mathrm{e}^{-\zeta(r-\sigma)}/(1+\zeta\sigma)\Big\} \tag{49}$$

In particular, $I_1(\sigma,s)$ appearing in the expression of $\hat{X}^{(0)}(\sigma,s)$ in Eq. (A12) is given by

$$I_1(\sigma,s) = \frac{\kappa[1+(\alpha+\zeta)\sigma]}{D(\zeta+\alpha)^2(1+\zeta\sigma)}. \tag{50}$$

Hence, the geminate reaction probability expression $\hat{X}^{(1)}(r,s)$ in Eq. (31) can be calculated by calculating two simple integrals numerically.

For the electron transfer between neutral reactants, the geminate reaction probability can be calculated most efficiently by using the Wilemski-Fixman-Weiss (WFW) expression given by Eq. (18). When $h(r) = 1$ and the reaction sink

function is given by Eq. (46), the two integrals $J_1(r,s)$ and $J_2(r,s)$ can be evaluated analytically as

$$J_1(r,s) = I_1(r,s) \tag{51}$$

$$\begin{aligned} J_2(r,s) = \kappa^2 \Big[D^2 r(\alpha+2\zeta)(4\alpha^4 - 5\alpha^2\zeta^2 + \zeta^4)^2(1+\zeta\sigma)^2 \Big]^{-1} \\ \times \Big\{ \mathrm{e}^{-2\alpha(r-\sigma)}(\alpha+2\zeta)(1+\zeta\sigma)^2 \Big[4\alpha^3(3+\alpha r) - \alpha(6+5\alpha r)\zeta^2 + \zeta^4 r \Big] \\ - \mathrm{e}^{-(\alpha+\zeta)(r-\sigma)}(1+\zeta\sigma)(4\alpha^2-\zeta^2)^2[2+2\alpha\sigma+(\alpha^2-\zeta^2)\sigma^2] \\ + \mathrm{e}^{-\zeta(r-\sigma)}(\alpha-\zeta)^2 \Big[(10\alpha^2+8\alpha\zeta+\zeta^2) \Big[2+2(2\alpha+\zeta)\sigma + (4\alpha^2+4\alpha\zeta-\zeta^2)\sigma^2 \Big] \\ + (\alpha+\zeta)(4\alpha^2-\zeta^2)(4\alpha^2+6\alpha\zeta+\zeta^2)\sigma^3 \Big] \Big\} \end{aligned} \tag{52}$$

An improved result can be obtained by using the expression $\hat{X}^{WFW}(r,s)$ in Eq. (18) to evaluate the ratio $\hat{X}(r_1,s)/\hat{X}(r,s)$ in Eq. (16).

Figures 3.2(a) – 3.2(f) display the time-dependent survival probabilities in highly reactive cases with $\bar{\lambda}(\sigma) = 20$, $A(\sigma) = 20$, $\nu_0 \equiv \nu[\bar{\lambda}(\sigma)]^{-1/2}/(D/\sigma^2) = 10^3$, and $\alpha\sigma = 10$. Each figure in this set represents a case of differing strength of interaction potential (measured by the value of r_c) and different initial separation *r* between the geminate reactants. The values of r_c and *r* used for calculation are noted in the figure legend. The full numerical results are displayed by filled squares, while the results of Eq. (31) for $r_c > 0$ and Eq. (18) for $r_c = 0$ are given by solid curves. We see that the approximate analytic results are in excellent agreement with the full numerical results, except for

$r_c = 14\sigma$ and $r = 2\sigma$ [Fig. 3.2(b)], in which case the present theory overestimates the survival probability.

In the high-reactivity limit, the survival probability is often approximated by[1]

$$W(r,t) \approx \exp[-S_R(r)t]. \tag{53}$$

This simple approximation assumes that the reaction proceeds before any movement of reactant occurs. In Fig. 3.2(a), the result of Eq. (53) is drawn by the dashed curve. We see that this approximation underestimates the survival probability considerably. For the other 5 cases in Fig. 3.2, the approxmation of Eq. (53) has been found to be much more worse, and thus its results are not drawn at all. When $r = \sigma$, it underestimates $W(r,t)$ too much. On the other hand, when $r = 2\sigma$, it overestimates $W(r,t)$ too much. In Figs. 3.2(c) – 3.2(f), results of the asymptotic expression of $W(r,t)$ in Eq. (34) have also been drawn by the dotted curves. In the case of Figs. 3.2(e) and 3.2(f), the dotted curves are hardly distinguishable from the solid curves except at very short times.

Figures 3.3(a) – 3.3(f) display the time-dependent survival probabilities in moderately reactive cases with $\bar{\lambda}(\sigma) = 20$, $A(\sigma) = 20$, $\nu_0 = 10^2$, and $\alpha\sigma = 10$. The values of r_c and r are varied in the same way as the corresponding figures of Fig. 3.2. Again, the approximate analytic results of Eq. (31) (for $r_c > 0$) and Eq. (18) (for $r_c = 0$), drawn by solid curves, are in excellent agreement with the full numerical results, drawn by filled squares, except for $r_c = 14\sigma$ and $r = 2\sigma$. In the case of Fig. 3.3(b), the present theory overestimates the survival probability.

The high-reactivity approximation of Eq. (53) is again useless; the trend is similar as in Fig. 3.2. Even in the most favorable case of Fig. 3.3(a), it underestimates the survival probability considerably. When $r = \sigma$ it underestimates $W(r,t)$ too much, and when $r = 2\sigma$ it overestimates $W(r,t)$ too much. In Figs. 3.3(c) – 3.3(f), results of the asymptotic expression of $W(r,t)$ in Eq. (34) have been drawn by the dotted curves. It is seen that these curves are in good agreement with the full numerical results except at short times.

Figures 3.4(a) – 3.4(f) display the time-dependent survival probabilities in weakly reactive cases with $\bar{\lambda}(\sigma) = 20$, $A(\sigma) = 20$, $\nu_0 = 10$, and $\alpha\sigma = 10$. The values of r_c and *r* are varied in the same way as the corresponding figures of Fig. 3.2. We note the same trend as in Figs. 3.2 and 3.3. The approximate analytic results of Eq. (31) (for $r_c > 0$) and Eq. (18) (for $r_c = 0$), drawn by solid curves, are in excellent agreement with the full numerical results, drawn by filled squares, except for $r_c = 14\sigma$ and $r = 2\sigma$. In the case of Fig. 3.4(b), the present theory overestimates the survival probability. Again, the high-reactivity approximation of Eq. (53) is useless. On the other hand, the asymptotic expression in Eq. (34), whose results are drawn by dotted curves in Figs. 3.4(c) – 3.4(f), are in good agreement with the full numerical results except at short times.

Figure 3.2. Time-dependent survival probabilities of geminate reactants in highly reactive cases with $\nu_0 = 10^3$, $\bar{\lambda}(\sigma) = 20$, $A(\sigma) = 20$, and $\alpha\sigma = 10$. The strength of interaction potential measured by r_c and the initial distance r between the reactants are varied as noted in the legends of Figs. 3.2(a) – 3.2(f).

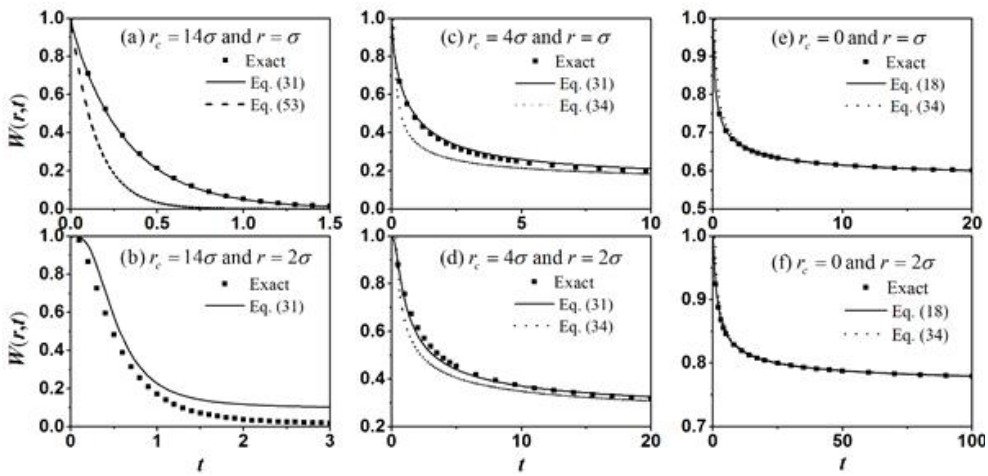

Figure 3.3. Time-dependent survival probabilities of geminate reactants in moderately reactive cases with $\nu_0 = 10^2$, $\bar{\lambda}(\sigma) = 20$, $A(\sigma) = 20$, and $\alpha\sigma = 10$. The strength of interaction potential measured by r_c and the initial distance r between the reactants are varied as noted in the legends of Figs. 3.3(a) – 3.3(f).

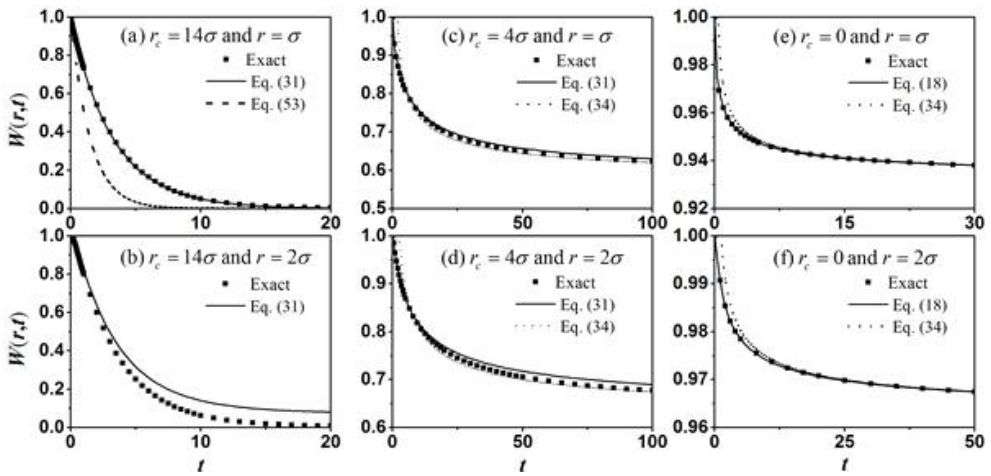

Figure 3.4. Time-dependent survival probabilities of geminate reactants in weakly reactive cases with $\nu_0 = 10$, $\bar{\lambda}(\sigma) = 20$, $A(\sigma) = 20$, and $\alpha\sigma = 10$. The strength of interaction potential measured by r_c and the initial distance r between the reactants are varied as noted in the legends of Figs. 3.4(a) – 3.4(f).

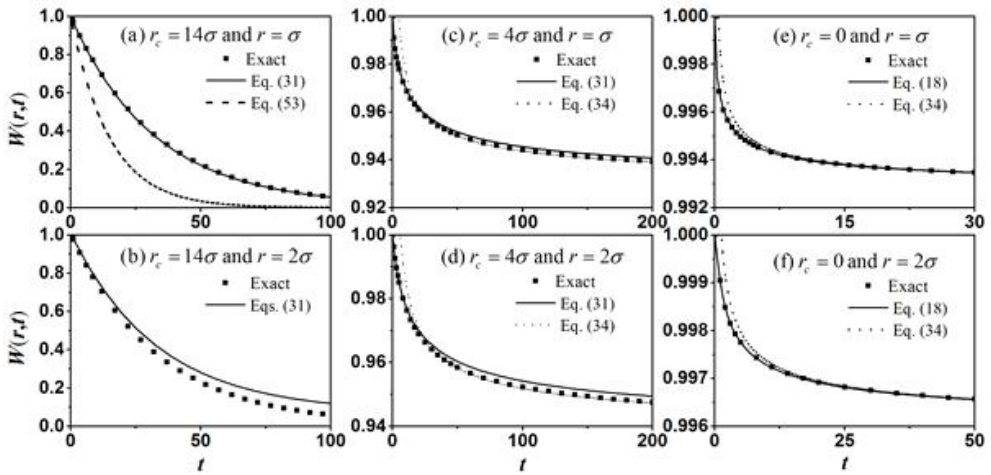

3.3.3. Results with the Marcus-model sink function in Eq. (5)

Figure 3.1 shows that the exponential sink function in Eq. (46) is not appropriate for the electron transfers in nonpolar solvents with $\varepsilon_s \cong 4$, if ΔG_∞ is larger than -2 eV for the reaction between ions or if ΔG_∞ is smaller than 0 eV for the reaction between neutral reactants. In this subsection, we examine the accuracy of the analytic expressions for the geminate reaction probability in these two situations. With the Marcus-model sink function in Eq. (5), together with the auxiliary relations given in Eqs. (44) and (45), the integrals $J_1(r,s)$, $J_2(r,s)$, and $I_1(r,s)$ defined by Eqs. (19), (20), and (A7) as well as the integral appearing in Eq. (31) need to be evaluated numerically.

Figures 3.5(a) – 3.5(d) display the time-dependent survival probabilities of geminate ion pairs in a nonpolar solvent. The values of parameters used are $\nu_0 \equiv \nu[\bar{\lambda}(\sigma)]^{-1/2}/(D/\sigma^2) = 10^3$, $\alpha\sigma = 10$, and $r_c = 14\sigma$. The distance-dependent dimensionless functions $\bar{\lambda}(r)$ and $A(r)$ are calculated by using Eq. (45). Each figure represents a case of differing values of ΔG_∞ and initial separation *r*, which are noted in the figure legend. The full numerical results are displayed by filled squares, while the results of Eq. (31) are given by solid curves. We also display the results of the asymptotic expression of $W(r,t)$ in Eq. (34) by the dotted curves.

We see that the approximate analytic results are in excellent agreement with the full numerical results in all cases, but the asymptotic expression is less useful. It is

noteworthy that the survival probability decays very slowly. For the same value of ν_0, the backward electron-transfer rate of ions is much smaller in nonpolar solvents than in polar solvents, because a large attractive Coulomb potential energy is lost upon neutralization.

Figure 3.6 displays the similar results as Fig. 3.5 but for the cases with a smaller reactivity parameter; $\nu_0 = 10^2$. The other parameters are the same as in Fig. 3.5. Again, each figure represents a case of differing values of ΔG_∞ and initial separation *r*, which are noted in the figure legend. We see that approximate analytic results of Eq. (31) represented by solid curves are in excellent agreement with the full numerical results represented by filled squares. Again, the asymptotic expression, whose results are displayed by the dotted curves, is found to be less useful.

Figures 3.7(a) – 3.7(d) display the time-dependent survival probabilities of a geminate pair of neutral reactants in a nonpolar solvent with $\varepsilon_s \cong 4$ and $\varepsilon_\infty \cong 2.5$. The values of reactivity parameters used are $\nu_0 \equiv \nu[\bar{\lambda}(\sigma)]^{-1/2} / (D/\sigma^2) = 10^3$ and $\alpha\sigma = 10$. The distance-dependent dimensionless functions $\bar{\lambda}(r)$ and $A(r)$ are calculated by using Eq. (45). Each figure represents a case of differing values of ΔG_∞ and initial separation *r*, which are noted in the figure legend. The full numerical results are displayed by filled squares, while the results of Eq. (18) are given by solid curves. We also display the results of the asymptotic expression of $W(r,t)$ in Eq. (34) by the dotted curves.

We see that the approximate analytic results are in excellent agreement with the full numerical results for the cases with $\Delta G_\infty = -2$ eV; see Figs. 3.7(c) and 3.7(d). However, for the cases with $\Delta G_\infty = -1$ eV, the theory underestimates the survival probabilty when $r = \sigma$. On the other hand, it overestimates the survival probability when $r = 2\sigma$. The reason for this discrepancy is the weak reactivity approximation of Eq. (17) employed in the derivation of Eq. (18). One may try to use Eq. (16) to get an improved result by an iterative procedure, but such an approach is impractical due to large computational cost.

Figure 3.8 displays the similar results as Fig. 3.7 but for the cases with a smaller reactivity parameter; $\nu_0 = 10^2$. The other parameters are the same as in Fig. 3.7. Again, each figure represents a case of differing values of ΔG_∞ and initial separation *r*, which are noted in the figure legend. As expected, for these weak-reactivity cases, approximate analytic results of Eq. (18) represented by solid curves are in excellent agreement with the full numerical results represented by filled squares. Results of the asymptotic expression for the survival probability in Eq. (34), displayed by the dotted curves, are also in good agreement with the full numerical results except at very short times. It is noteworthy that the backward electron-transfer occurs much faster between neutral reactants than between ions for the same value of ν_0, because a large attractive Coulomb potential energy is gained upon reaction in the former case while it is lost in the latter case.

Figure 3.5. Time-dependent survival probabilities of geminate ions in a nonpolar solvent. The values of parameters used are $\nu_0 = 10^3$, $\alpha\sigma = 10$, and $r_c = 14\sigma$. The values of ΔG_∞ and the initial distance *r* between the reactants are varied as noted in the legends of Figs. 3.5(a) – 3.5(d).

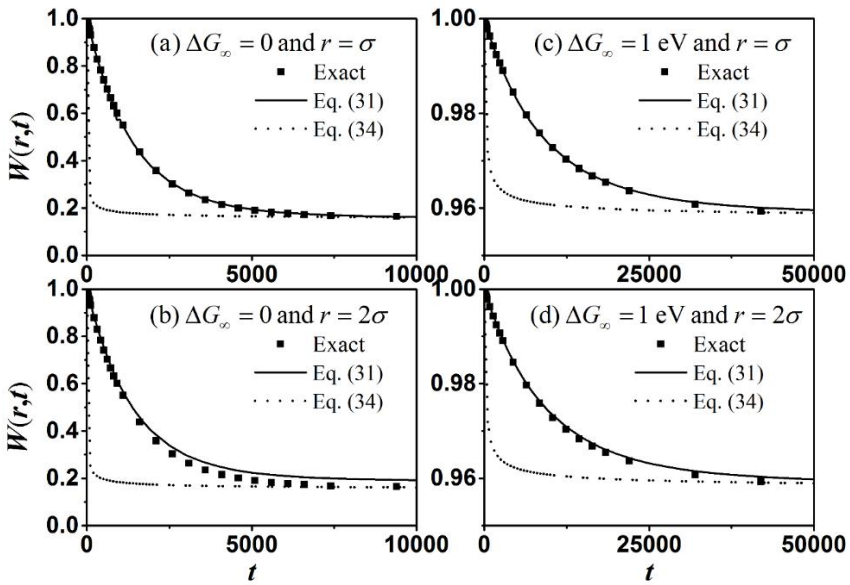

Figure 3.6. Time-dependent survival probabilities of geminate ions in a nonpolar solvent. The values of parameters used are $\nu_0 = 10^2$, $\alpha\sigma = 10$, and $r_c = 14\sigma$. The values of ΔG_∞ and the initial distance *r* between the reactants are varied as noted in the legends of Figs. 3.6(a) –3.6(d).

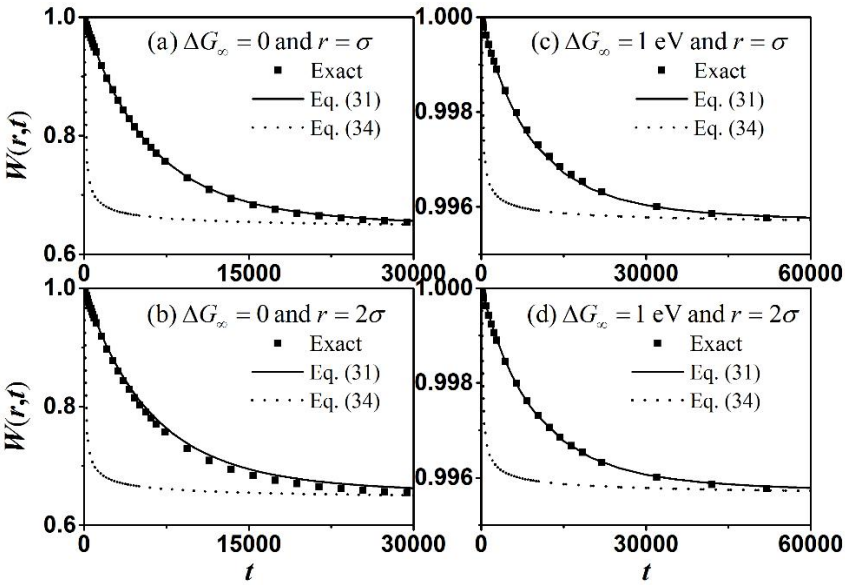

Figure 3.7. Time-dependent survival probabilities of geminate pairs of neutral reactants in a nonpolar solvent. The values of parameters used are $\nu_0 = 10^3$ and $\alpha\sigma = 10$. The values of ΔG_∞ and the initial distance r between the reactants are varied as noted in the legends of Figs. 3.7(a) – 3.7(d).

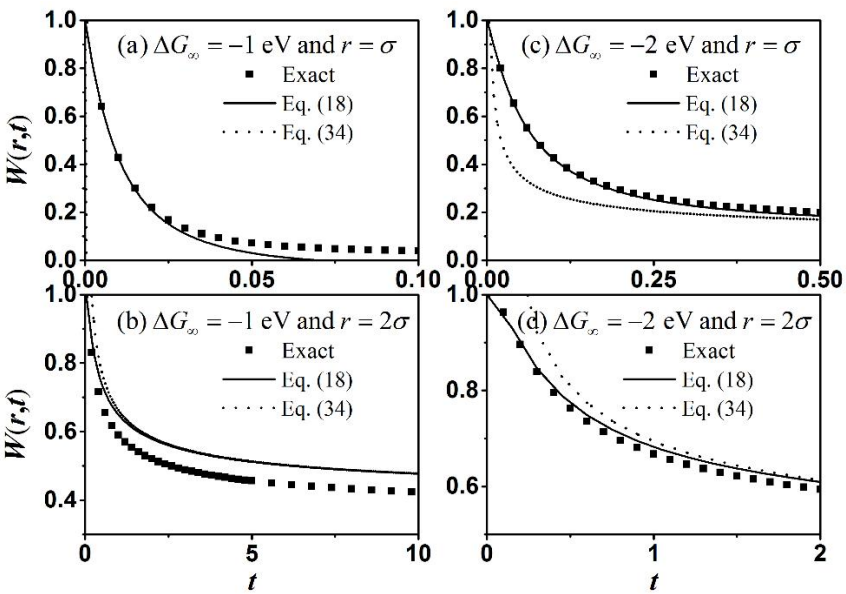

Figure 3.8. Time-dependent survival probabilities of geminate pairs of neutral reactants in a nonpolar solvent. The values of parameters used are $\nu_0 = 10^2$ and $\alpha\sigma = 10$. The values of ΔG_∞ and the initial distance r between the reactants are varied as noted in the legends of Figs. 3.8(a) – 3.8(d).

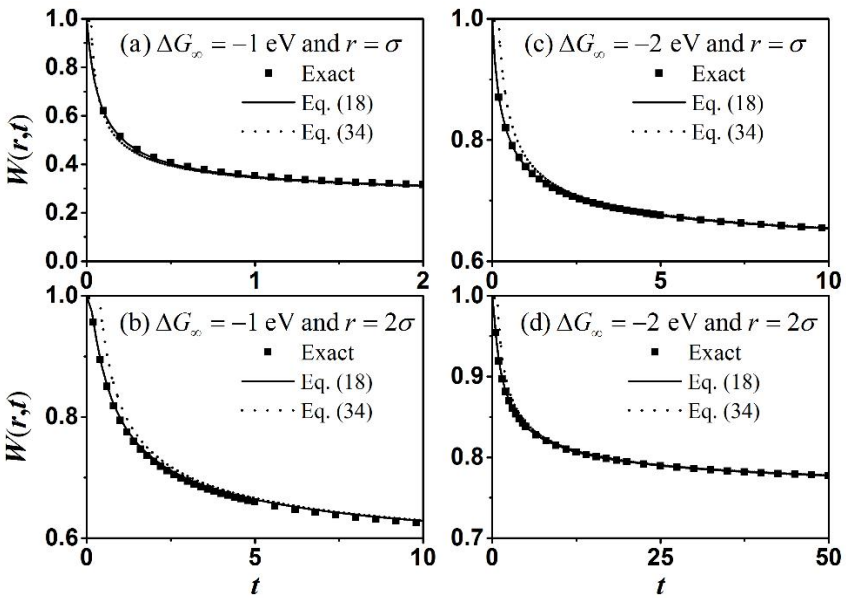

3.4. Concluding remarks

We presented analytic expressions for the time-dependent electron-transfer rate and the survival probability of geminate ions, which have a distance-dependent reactivity and undergo the Brownian motion under the influence of attractive Coulomb interaction. Equation (31) together with Eq. (A11) provides reasonably accurate results for most reactivity parameters. We have considered the cases for which the reactivity differs by two orders of magnitude and has a varying range; the results calculated for a longer-ranged sink function with $\alpha\sigma = 5$ are given in the Supplementary Material. In the case of neutral reactants, the Wilemski-Fixman-Weiss expression for the geminate recombination probability given in Eq. (18), or its generalized version given in Eq. (16) is found to be more useful owing to the availability of an exact Green's function expression. In addition, the asymptotic expression given in Eq. (34) must be useful in the cases with weak to moderate reactivity. It gives a very quick estimate for the intermediate to long time survival probability.

The present theoretical results can be particularly useful in analyzing the back electron-transfer phase of photo-induced reactions, where the photon energy is close to the threshold value so that the initially generated reactant pair has a small separation.[20]

Appendix: a large-s approximation for $\hat{X}(r,s)$

Equation (22) for the geminate reaction probability $\hat{X}(r,s)$ can be rewritten as

$$s\hat{X}(r,s) = L_0(r)\hat{X}(r,s) - L_1(r)\hat{X}(r,s) - S_R(r)\hat{X}(r,s) + \frac{1}{s}S_R(r) \tag{A1}$$

where

$$L_0(r) = D\frac{1}{r^2}\frac{\partial}{\partial r}r^2 h(r)\frac{\partial}{\partial r}, \tag{A2}$$

$$L_1(r) = Dh(r)\frac{\partial U(r)}{\partial r}\frac{\partial}{\partial r}. \tag{A3}$$

With the Green's function for the Smoluchowski equation in the absence of interaction potential, which can be represented by

$$\hat{G}_h(r,s|r_0) = \frac{1}{s - L_0(r)}\frac{\delta(r-r_0)}{4\pi r_0^2}, \tag{A4}$$

Eq. (A1) can be recast into an integral equation,

$$\hat{X}(r,s) = \frac{1}{s}4\pi\int_\sigma^\infty dr_1\, r_1^2\hat{G}_h(r,s|r_1)S_R(r_1) - 4\pi\int_\sigma^\infty dr_1\, r_1^2\hat{G}_h(r,s|r_1)L_1(r_1)\hat{X}(r_1,s)$$

$$-4\pi\int_\sigma^\infty dr_1\, r_1^2\hat{G}_h(r,s|r_1)S_R(r_1)\hat{X}(r_1,s). \tag{A5}$$

By manipulating the second term on the right hand side by integration by parts, Eq. (A5) can be rewritten as

$$\hat{X}(r,s) = \frac{1}{s}I_1(r,s) + M(r,s|\sigma)\hat{X}(\sigma,s) + \int_\sigma^\infty dr_1\,\hat{X}(r_1,s)\frac{\partial}{\partial r_1}M(r,s|r_1)$$

$$-4\pi\int_\sigma^\infty dr_1\, r_1^2\hat{G}_h(r,s|r_1)S_R(r_1)\hat{X}(r_1,s), \tag{A6}$$

where

$$I_1(r,s) = 4\pi \int_\sigma^\infty dr_1\, r_1^2 \hat{G}_h(r,s|r_1) S_R(r_1)\,, \tag{A7}$$

$$M(r,s|r_1) = 4\pi D r_1^2 h(r_1) U'(r_1) \hat{G}_h(r,s|r_1)\,. \tag{A8}$$

At short times (for large s), the Green's function $\hat{G}_h(r,s|r_1)$ is very small unless $r_1 \cong r$. We can thus make the following approximation for the two integrals in Eq. (A6):

$$\int_\sigma^\infty dr_1\, \hat{X}(r_1,s) \frac{\partial}{\partial r_1} M(r,s|r_1)$$

$$\cong \hat{X}(r,s) \int_\sigma^\infty dr_1 \frac{\partial}{\partial r_1} M(r,s|r_1) = -\hat{X}(r,s) M(r,s|\sigma) \tag{A9}$$

$$4\pi \int_\sigma^\infty dr_1\, r_1^2 \hat{G}_h(r,s|r_1) S_R(r_1) \hat{X}(r_1,s)$$

$$\cong \hat{X}(r,s) 4\pi \int_\sigma^\infty dr_1\, r_1^2 \hat{G}_h(r,s|r_1) S_R(r_1) = \hat{X}(r,s) I_1(r,s) \tag{A10}$$

With these approximations, Eq. (A6) gives the following zeroth-order approximation to $\hat{X}(r,s)$:

$$s\hat{X}^{(0)}(r,s) = \frac{I_1(r,s) + M(r,s|\sigma) s\hat{X}(\sigma,s)}{1 + I_1(r,s) + M(r,s|\sigma)} \tag{A11}$$

with

$$s\hat{X}^{(0)}(\sigma,s) = I_1(\sigma,s) / [1 + I_1(\sigma,s)]\,. \tag{A12}$$

By using this zeroth-order expression to evaluate the ratio $\hat{X}(r_1,s) / \hat{X}(r,s)$ in Eq. (30), we can obtain an accurate estimate of the geminate reaction probability $\hat{X}(r,s)$.

Supplementary Material

Figure 3.S2. Time-dependent survival probabilities of geminate reactants in highly reactive cases with $\nu_0 = 10^3$, $\bar{\lambda}(\sigma) = 20$, $A(\sigma) = 20$, and $\alpha\sigma = 5$. The strength of interaction potential measured by r_c and the initial distance *r* between the reactants are varied as noted in the legend.

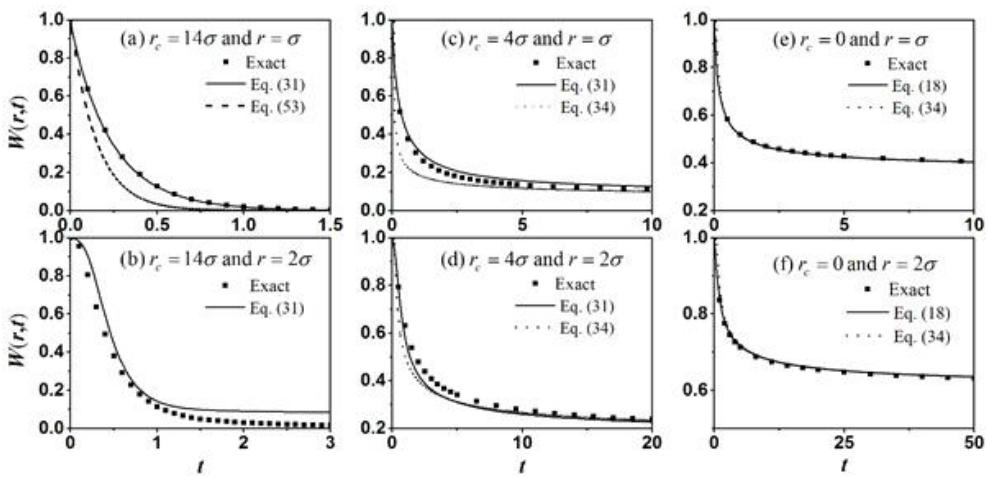

Figure 3.S3. Time-dependent survival probabilities of geminate reactants in moderately reactive cases with $\nu_0 = 10^2$, $\bar{\lambda}(\sigma) = 20$, $A(\sigma) = 20$, and $\alpha\sigma = 5$. The strength of interaction potential measured by r_c and the initial distance r between the reactants are varied as noted in the legend.

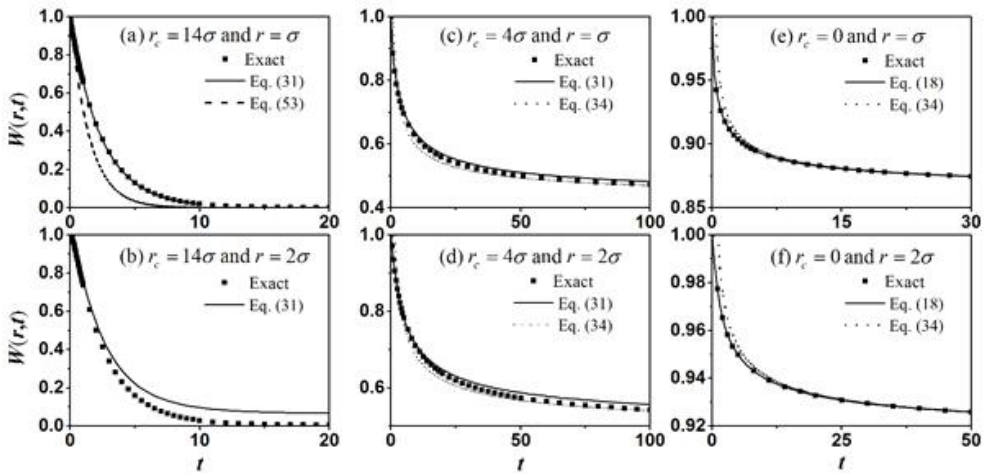

Figure 3.S4. Time-dependent survival probabilities of geminate reactants in weakly reactive cases with $\nu_0 = 10$, $\bar{\lambda}(\sigma) = 20$, $A(\sigma) = 20$, and $\alpha\sigma = 5$. The strength of interaction potential measured by r_c and the initial distance *r* between the reactants are varied as noted in the legend.

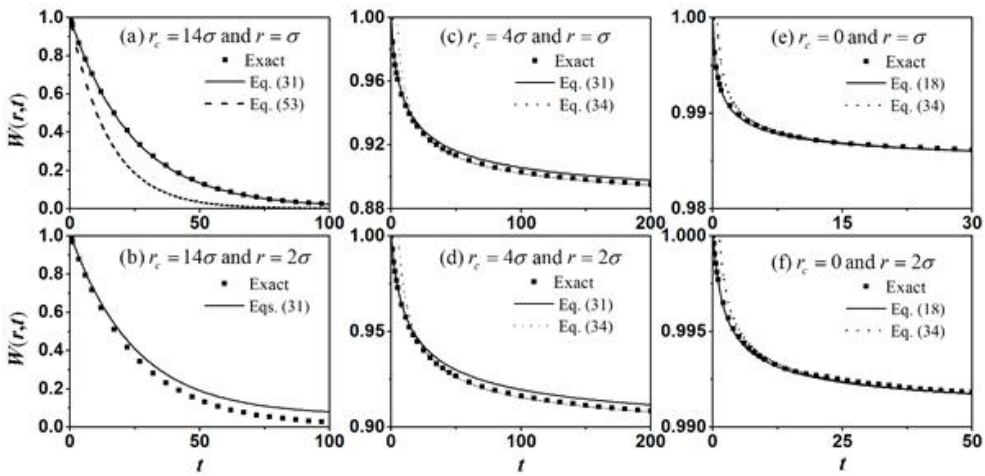

Figure 3.S5. Time-dependent survival probabilities of geminate ions in a nonpolar solvent. The values of parameters used are $\nu_0 = 10^3$, $\alpha\sigma = 5$, and $r_c = 14\sigma$. The values of ΔG_∞ and the initial distance *r* between the reactants are varied as noted in the legend.

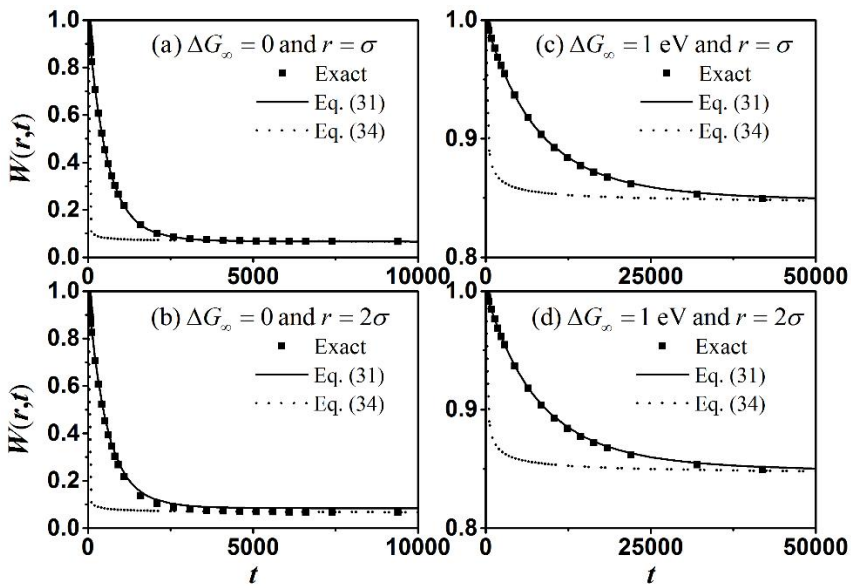

Figure 3.S6. Time-dependent survival probabilities of geminate ions in a nonpolar solvent. The values of parameters used are $\nu_0 = 10^2$, $\alpha\sigma = 5$, and $r_c = 14\sigma$. The values of ΔG_∞ and the initial distance *r* between the reactants are varied as noted in the legend.

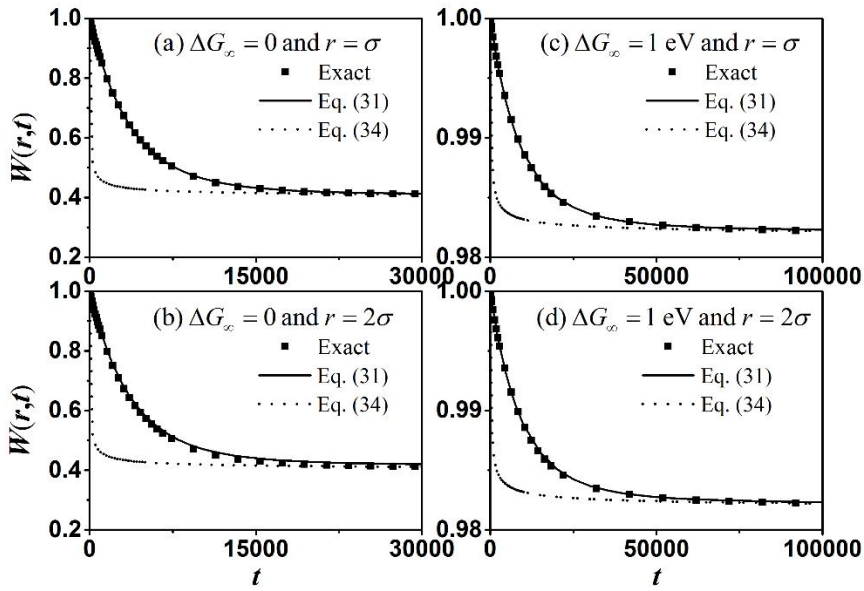

Figure 3.S7. Time-dependent survival probabilities of geminate pairs of neutral reactants in a nonpolar solvent. The values of parameters used are $\nu_0 = 10^3$ and $\alpha\sigma = 5$. The values of ΔG_∞ and the initial distance r between the reactants are varied as noted in the legend.

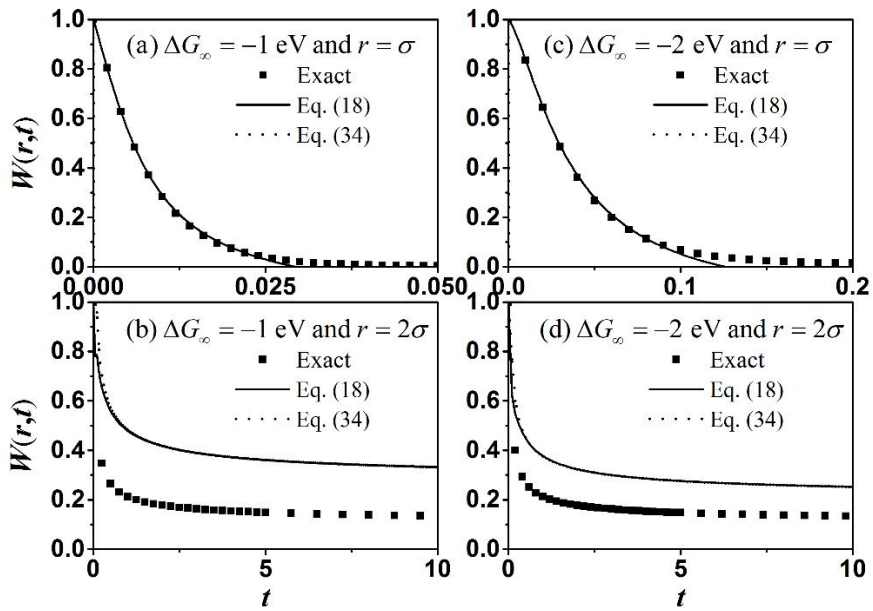

Figure 3.S8. Time-dependent survival probabilities of geminate pairs of neutral reactants in a nonpolar solvent. The values of parameters used are $\nu_0 = 10^2$ and $\alpha\sigma = 5$. The values of ΔG_∞ and the initial distance r between the reactants are varied as noted in the legend.

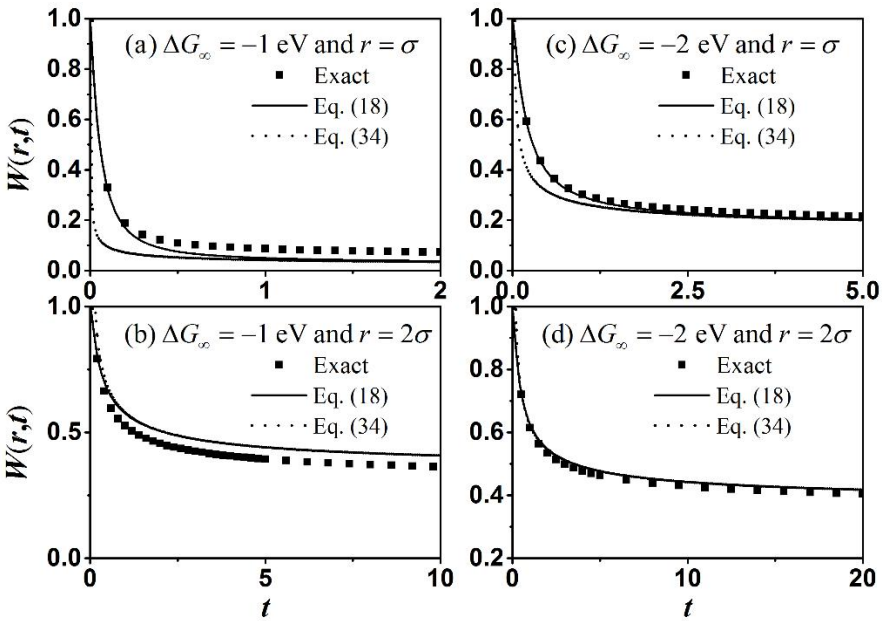

References

1. S. A. Rice, in *Diffusion-Limited Reactions*, Comprehensive Chemical Kinetics Vol. 25, edited by C. H. Bamford, C. F. H. Tipper, and R. G. Compton (Elsevier, Amsterdam, 1985).
2. A. I. Burshtein, Adv. Chem. Phys. **129**, 105 (2004).
3. A. V. Barzykin, P. A. Frantsuzov, K. Seki, and M. Tachiya, Adv. Chem. Phys. **123**, 511 (2002).
4. L. Onsager, Phys. Rev. **54**, 554 (1938).
5. K. M. Hong and J. Noolandi, J. Chem. Phys. **68**, 5163 (1978).
6. K. M. Hong and J. Noolandi, J. Chem. Phys. **69**, 5026 (1978).
7. J. Noolandi and K. M. Hong, J. Chem. Phys. **70**, 3230 (1979).
8. M. Tachiya, J. Chem. Phys. **70**, 238 (1979).
9. H. Sano and M. Tachiya, J. Chem. Phys. **71**, 1276 (1979).
10. M. Tachiya, Radiat. Phys. Chem. **21**, 167 (1983).
11. J. B. Pedersen, J. Chem. Phys. **72**, 3904 (1980).
12. S. Traytak, Chem. Phys. **154**, 263 (1991).
13. R. C. Dorfman and M. D. Fayer, J. Chem. Phys. **96**, 7410 (1992).
14. S. F. Swallen and M. D. Fayer, J. Chem. Phys. **103**, 8864 (1995).
15. K. Weidemaier, H. L. Tavernier, S. F. Swallen, and M. D. Fayer, J. Phys. Chem. A **101**, 1887 (1997).
16. V. S. Gladkikh, A. I. Burshtein, H. L. Tavernier, and M. D. Fayer, J. Phys. Chem. A **106**, 6982 (2002).

17. S. G. Fedorenko, A. A. Kipriyanov, and A. B. Doktorov, Physics Research International **2011**, 451670 (2011).

18. G. Angulo, D. R. Kattnig, A. Rosspeintner, G. Grampp, and E. Vauthey, Chem. Eur. J. **16**, 2291 (2010).

19. A. Rosspeintner and E. Vauthey, Phys. Chem. Chem. Phys. **16**, 25741 (2014).

20. Y. Suzuki, A. Furube, R. B. Singh, H. Matsuzaki, T. Minegishi, T. Hisatomi, K. Domen, and K. Seki, J. Phys. Chem. C **119**, 5364 (2015).

21. S. Lee, C. Y. Son, J. Sung, and S. Chong, J. Chem. Phys. **134**, 121102 (2011).

22. C. Y. Son, J. Kim, J.-H. Kim, J. S. Kim, and S. Lee, J. Chem. Phys. **138**, 164123 (2013).

23. K. Lee, S. Lee, C. H. Choi, and S. Lee, J. Chem. Phys. **147**, 144111 (2017).

24. K. Seki and M. Wojcik, J. Phys. Chem. C **121**, 3632 (2017).

25. M. Wojcik, A. Nowak, and K. Seki, J. Chem. Phys. **146**, 054101 (2017).

26. G. Wilemski and M. Fixman, J. Chem. Phys. **58**, 4009 (1973).

27. A. Nitzan, *Chemical Dynamics in Condensed Phases* (Oxford, UK, 2006).

28. M. Tachiya and S. Murata, J. Phys. Chem. **96**, 8441 (1992).

29. R. A. Marcus, J. Chem. Phys. **24**, 966 (1956); **26**, 867 (1957); **43**, 679 (1965).

30. C. Gardiner, *Stochastic Methods*, 4th ed. (Springer, Berlin, 2009).

31. G. H. Weiss, J. Chem. Phys. **80**, 2880 (1984).

32. M. R. Flannery, Phys. Rev. Lett. **47**, 163 (1981).

33. H. Stehfest, Commun. ACM, **13**, 47 (1970); **13**, 624 (1970).

Chapter 4

4. New method for constant-*NPT* molecular dynamics

4.1. Introduction

The traditional molecular dynamics (MD) simulation methods are for microcanonical ensemble systems that have conserved energy, volume, and number of particles.[1,2] However, a majority of experiments on physicochemical systems are carried out at constant temperature and pressure, in which the energy and volume of the system fluctuate. To examine the dynamical properties of molecules in such systems, one often employs the MD methods with thermostatting and barostatting algorithms. Unfortunately, the well-established thermostatting algorithms such as Andersen thermostat,[3] Berendsen thermostat,[4] Nosé-Hoover thermostat,[5,6] as well as the barostatting algorithms such as Andersen barostat, [3]Berendsen barostat,[4] and their variants,[7-13] may alter the dynamic properties of the molecules under consideration, because their equations of motion are modified by the coupling with the thermostat or the barostat.[2,14] For this reason, the dynamic properties of molecules have often been investigated by performing simulations using a constant-NVE MD method after preparing the system at chosen temperature and density.[15,16]

Another problem with the existing barostatting algorithms based on the Andersen barostat is that all the relative distances between particles are displaced

in the same proportion as the volume fluctuates. This would cause an obvious problem when there are groups of molecules with different compressibility.

In this paper, we propose a new MD simulation method, which is based on the fact that only the molecules near the boundary are directly disturbed by the movable thermal boundary in the real system. We thus introduce a boundary region in the simulation box and only the particles in this region are directly coupled to the thermostat and barostat. Thus the equations of motion for molecules located in the inner part of the simulation box remain intact. If a molecule of interest moves to the vicinity of the boundary region, we can simply relocate the boundary to keep the molecule at the central part of the simulation box.

The idea that only the molecules near the boundary must be thermally perturbed was often implemented, especially in simulating nonequilibrium systems,[17,18] by thermalizing the velocities of the molecules that strike the walls of the simulation box. Our approach that will be detailed in the next section differs from the previous ones in that the equations of motion of the particles in the boundary region are modulated according to the extended Lagrangian method as proposed originally by Andersen[3] and Nose[5] and modified later by Hoover[6] and Martyna, et al.[7,9] As for the barostatting algorithm, our method has some similarities with that of Uline and Corti[19,20] in that the volume fluctuation is controlled by the particles located at the wall, but in contrast with their method considering a single shell particle controlling the volume fluctuation, we consider the collective effect of the particles in the boundary region.

We test the efficiency of our algorithm in attaining the target temperature and pressure, and the conformity of the calculated equilibrium properties to those obtained from the widely used constant-NPT MD methods provided by Martyna, et al.[7-9] and Berendsen, et al.[4] For the dynamic properties, such as the mean square displacement, we compare our MD results with those from the constant-NVE MD simulations carried out under the same average temperature and pressure. In addition, we also check if our MD method correctly samples the desired thermodynamic ensemble by performing the test proposed recently by Shirts.[21]

We find that our MD method is as efficient as the Nosé-Hoover thermostat and the Andesen barostat in attaining the target temperature and pressure. Once the target temperature and pressure are reached, our method maintains the constant NPT condition in both inner and boundary regions. Although the Berendsen's constant-NPT MD method is very efficient to attain the target temperature and pressure, it does not produce the simulation results conforming to the true constant-NPT ensemble. Therefore, for a very large system, one may use the Berendsen's methods in the initial phase of the equilibration run, and thereafter employ our method to obtain reliable simulation results that conform to the constant-NPT ensemble system and do not alter the dynamic properties of the molecules of interest.

In Section 2, theoretical background of our constant-NPT MD methods is described. In Section 3 we present the details of the simulation procedures for testing the new MD methods, and compare our results with those obtained by other

constant-NPT MD methods like Andersen-Nosè-Hoover MD method as extended by Martyna, et al.[7-9] The efficiency of our new MD method in attaining the target temperature and pressure is also discussed. Section 4 summarizes the present work.

4.2. Theoretical background for the new MD method

4.2.1. Equations of motion

We divide the simulation box into the boundary and inner regions. The boundary region, which is the border region of the simulation box of uniform width, is defined by the ratio of its volume V_b to the volume V of the whole system. The particles in the inner region move according to the Newton's equation of motion,

$$\dot{\mathbf{r}}_i = \frac{\mathbf{p}_i}{m_i} \quad \text{and} \quad \dot{\mathbf{p}}_i = -\frac{\partial U}{\partial \mathbf{r}_i}, \tag{1}$$

where $\mathbf{r}_i$, $\mathbf{p}_i$, and m_i denote, respectively, the position, momentum, and mass of the ith particle in the inner region. U denotes the potential energy, and a dot over a letter indicates a time derivative.

The equations of motion for particles in the boundary region are based on the extended Lagrangian method proposed originally by Andersen[3] and Nose.[5] We modify the equations of motion proposed by Hoover[6] and Martyna, et al.[7-9] as

$$\dot{\mathbf{r}}_i = \frac{\mathbf{p}_i}{m_i} + \frac{1}{3}\frac{\dot{V}}{V_b}\mathbf{r}_i \tag{2}$$

$$\dot{\mathbf{p}}_i = -\frac{\partial U}{\partial \mathbf{r}_i} - \frac{1}{3}\frac{\dot{V}}{V_b}\mathbf{p}_i - \frac{p_\eta}{Q_\eta}\mathbf{p}_i \tag{3}$$

In these equations, V_b denotes the volume of the boundary region as mentioned above. p_η and Q_η are, respectively, the "momentum" and an effective "mass" associated with the thermostat variable η. The equations of motion for the thermostat and barostat variables are given by

$$\dot{\eta} = \frac{p_\eta}{Q_\eta} \tag{4}$$

$$\dot{p}_\eta = \sum_i{}'' \frac{\mathbf{p}_i^2}{m_i} - 3N_b k_B T \tag{5}$$

$$\dot{V} = \frac{p_V}{W} \tag{6}$$

$$\dot{p}_V = \mathcal{P}_b - P - \frac{p_\xi}{Q_\xi} p_V \tag{7}$$

$$\dot{\xi} = \frac{p_\xi}{Q_\xi} \tag{8}$$

$$\dot{p}_\xi = \frac{p_V^2}{W} - k_B T \tag{9}$$

In eq 5, Σ_i'' denotes a restricted summation over those particles in the boundary region and N_b is the number of particles in the boundary region. k_B is the Boltzmann constant and T is the bath temperature. In eq 6, p_V and W are, respectively, the "momentum" and an effective "mass" associated with the barostat variable V. In eq 7, P is the external pressure, and $\mathcal{P}_b$ is the internal pressure of the boundary region given by

$$\mathcal{P}_b = \frac{1}{3V_b}\sum_i{}'' \left(\frac{\mathbf{p}_i^2}{m_i} + \mathbf{r}_i \cdot \mathbf{f}_i \right), \tag{10}$$

where $\mathbf{f}_i$ is the force on the *i*th particle. The equation of motion for p_V is modulated by another thermostat variable ξ. p_ξ and Q_ξ are, respectively, the "momentum" and an effective "mass" associated with ξ, and the equations of motion for ξ and p_ξ are given by eqs 8 and 9.

We now examine whether the equations of motion given by eqs 1 – 10 provide the proper isothermal-isobaric ensemble distribution. We will employ the statistical mechanical analysis method for non-Hamiltonian systems proposed by Tuckerman, et al.[22-25] First, it can be shown easily that if the number of particles in the boundary region, N_b, remains practically constant during the course of simulation, there is a conserved energy of the form,

$$H'(\mathbf{r}^N, \mathbf{p}^N, V, p_V, \eta, p_\eta, \xi, p_\xi) = H_0(\mathbf{r}^N, \mathbf{p}^N)$$

$$+ \frac{p_V^2}{2W} + PV + \frac{p_\eta^2}{2Q_\eta} + 3N_b k_B T\eta + \frac{p_\xi^2}{2Q_\xi} + k_B T\xi, \tag{11}$$

where $H_0(\mathbf{r}^N, \mathbf{p}^N)$ is the physical Hamiltonian with $(\mathbf{r}^N, \mathbf{p}^N)$ denoting the positions and momenta of all *N* particles in the system. The constancy of N_b may not hold for small system with low density, but for large and dense system the fluctuation in the value of N_b must be negligible. Because of the external force acting on the particles in the boundary region, due to the imbalance of external and

internal pressures, the total momentum of the particles is not conserved and H' is the only conserved quantity.

Next, the extended phase-space compressibility is given by

$$\kappa(\mathbf{X}) \equiv \frac{\partial}{\partial \mathbf{X}} \cdot \dot{\mathbf{X}} = \sum_i{}' \frac{\partial}{\partial \mathbf{r}_i} \cdot \dot{\mathbf{r}}_i + \sum_i{}'' \frac{\partial}{\partial \mathbf{r}_i} \cdot \dot{\mathbf{r}}_i + \sum_i{}' \frac{\partial}{\partial \mathbf{p}_i} \cdot \dot{\mathbf{p}}_i + \sum_i{}'' \frac{\partial}{\partial \mathbf{p}_i} \cdot \dot{\mathbf{p}}_i$$

$$+ \frac{\partial \dot{V}}{\partial V} + \frac{\partial \dot{p}_V}{\partial p_V} + \frac{\partial \dot{\eta}}{\partial \eta} + \frac{\partial \dot{p}_\eta}{\partial p_\eta} + \frac{\partial \dot{\xi}}{\partial \xi} + \frac{\partial \dot{p}_\xi}{\partial p_\xi}$$

$$= -3N_b \dot{\eta} - \dot{\xi} . \tag{12}$$

Here, we have introduced the shorthand notation $\mathbf{X}$ for the extended phase-space coordinates $(\mathbf{r}^N, \mathbf{p}^N, V, p_V, \eta, p_\eta, \xi, p_\xi)$, and $\Sigma_i{}'$ denotes a restricted summation over those particles in the inner region. We thus obtain the phase-space metric factor as

$$\sqrt{g(\mathbf{X})} = e^{3N_b \eta + \xi} \tag{13}$$

The partition function for the extended non-Hamiltonian system is then given by[22-25]

$$\Omega = \int d\mathbf{X} \sqrt{g(\mathbf{X})}\ \delta(H' - C_1)$$

$$= \int d\mathbf{p}^N \int d\mathbf{r}^N \int dp_V \int dV \int dp_\xi \int d\xi \int dp_\eta$$

$$\times \int d\eta\, e^{3N_b \eta} e^{\xi} \delta\left(H_0(\mathbf{r}^N, \mathbf{p}^N) + \frac{p_V^2}{2W} + PV + \frac{p_\eta^2}{2Q_\eta} + 3N_b k_B T \eta + \frac{p_\xi^2}{2Q_\xi} + k_B T \xi - C_1 \right)$$

$$= \frac{1}{3N_b k_B T} \int d\xi \int dp_V \int dp_\xi \int dp_\eta \exp\left\{ -\frac{1}{k_B T} \frac{p_V^2}{2W} - \frac{1}{k_B T} \frac{p_\eta^2}{2Q_\eta} - \frac{1}{k_B T} \frac{p_\xi^2}{2Q_\xi} + \frac{1}{k_B T} C_1 \right\}$$

$$\times \int d\mathbf{p}^N \int d\mathbf{r}^N \int dV \exp\left\{-\frac{1}{k_B T}\left[H_0(\mathbf{r}^N, \mathbf{p}^N) + PV\right]\right\} \tag{14}$$

One can note that, aside from the arbitrary normalization factor given by the first integral over the thermostat and barostat variables, the second integral over $(\mathbf{r}^N, \mathbf{p}^N, V)$ represents the isothermal-isobaric partition function for the *N*-particle system.

4.2.2. Reversible symplectic integrator

Any dynamic function $A(\mathbf{X})$ of the extended phase-space coordinates **X**, which has no explicit time-dependence, evolves in time as

$$\frac{d}{dt} A(\mathbf{X}) = \frac{\partial A}{\partial \mathbf{X}} \cdot \dot{\mathbf{X}} = \dot{\mathbf{X}} \cdot \frac{\partial}{\partial \mathbf{X}} A \equiv iLA \,. \tag{15}$$

The Liouville operator is given by

$$\begin{aligned} iL &= \dot{\mathbf{X}} \cdot \frac{\partial}{\partial \mathbf{X}} = \sum_i{}' \dot{\mathbf{r}}_i \cdot \frac{\partial}{\partial \mathbf{r}_i} + \sum_i{}'' \dot{\mathbf{r}}_i \cdot \frac{\partial}{\partial \mathbf{r}_i} + \sum_i{}' \dot{\mathbf{p}}_i \cdot \frac{\partial}{\partial \mathbf{p}_i} + \sum_i{}'' \dot{\mathbf{p}}_i \cdot \frac{\partial}{\partial \mathbf{p}_i} \\ &\quad + \dot{V} \frac{\partial}{\partial V} + \dot{p}_V \frac{\partial}{\partial p_V} + \dot{\eta} \frac{\partial}{\partial \eta} + \dot{p}_\eta \frac{\partial}{\partial p_\eta} + \dot{\xi} \frac{\partial}{\partial \xi} + \dot{p}_\xi \frac{\partial}{\partial p_\xi} \\ &= iL_1 + iL_2 + iL_3 + iL_4 + iL_5 + iL_6 \end{aligned} \tag{16}$$

with

$$iL_1 = \sum_i{}' \mathbf{v}_i \cdot \frac{\partial}{\partial \mathbf{r}_i} + \sum_i{}'' \left(\mathbf{v}_i + \frac{1}{3} \frac{\dot{V}}{V_b} \mathbf{r}_i \right) \cdot \frac{\partial}{\partial \mathbf{r}_i} + \dot{V} \frac{\partial}{\partial V} , \tag{17}$$

$$iL_2 = \sum_i{}' \frac{\mathbf{f}_i}{m_i} \cdot \frac{\partial}{\partial \mathbf{v}_i} + \sum_i{}'' \left(\frac{\mathbf{f}_i}{m_i} - \frac{1}{3} \frac{\dot{V}}{V_b} \mathbf{v}_i \right) \cdot \frac{\partial}{\partial \mathbf{v}_i} , \tag{18}$$

$$iL_3 = \left(\frac{\Delta P}{W} - v_\xi \dot{V} \right) \frac{\partial}{\partial \dot{V}} + v_\xi \frac{\partial}{\partial \xi}, \tag{19}$$

$$iL_4 = \frac{G_\xi}{Q_\xi} \frac{\partial}{\partial v_\xi}, \tag{20}$$

$$iL_5 = \sum_i{}'' \left(-v_\eta \mathbf{v}_i \right) \cdot \frac{\partial}{\partial \mathbf{v}_i} + v_\eta \frac{\partial}{\partial \eta}, \tag{21}$$

$$iL_6 = \frac{G_\eta}{Q_\eta} \frac{\partial}{\partial v_\eta}. \tag{22}$$

In eqs 17 – 22, $\mathbf{v}_i$ is the velocity of the *i*th particle, $\dot{V}$ is the "volume velocity" as given by eq 6, and

$$v_\eta = \frac{p_\eta}{Q_\eta}, \quad v_\xi = \frac{p_\xi}{Q_\xi}, \quad G_\eta = \sum_i{}'' m_i \mathbf{v}_i^2 - 3N_b k_B T,$$

$$G_\xi = W\dot{V}^2 - k_B T, \quad \Delta P = \mathcal{P}_b - P. \tag{23}$$

Under the condition that the number of particles in the boundary region, N_b, remains practically constant, we may neglect the time-dependence of the Liouville operator, and write a formal solution to eq 15 as

$$A(\mathbf{X}(t)) = e^{iLt} A(\mathbf{X}(0)). \tag{24}$$

In particular, we have

$$\mathbf{X}(\Delta t) = e^{iL\Delta t} \mathbf{X}(0). \tag{25}$$

For small Δt, by applying the Trotter formula repeatedly,[26,27] the time-evolution operator $e^{iL\Delta t}$ is factorized approximately as

$$e^{iL\Delta t} = e^{i(L_5+L_6)\Delta t/2} e^{i(L_3+L_4)\Delta t/2} e^{i(L_1+L_2)\Delta t} e^{i(L_3+L_4)\Delta t/2} e^{i(L_5+L_6)\Delta t/2} + O(\Delta t^3). \tag{26}$$

The operator, $e^{i(L_1+L_2)\Delta t}$, which governs the time evolution of the coordinates and velocities of particles is further factorized as

$$e^{i(L_1+L_2)\Delta t} = e^{iL_2\Delta t/2} e^{iL_1\Delta t} e^{iL_2\Delta t/2} + O(\Delta t^3). \tag{27}$$

For the operators, $e^{i(L_3+L_4)\Delta t}$ and $e^{i(L_5+L_6)\Delta t}$, which mainly govern the time evolution of thermostat variables, we have applied a higher-order factorization as proposed by Yoshida:[27]

$$e^{i(L_3+L_4)\Delta t/2} = e^{iL_4 w_1\Delta t/2} e^{iL_3 w_2\Delta t/2} e^{iL_4 w_3\Delta t/2} e^{iL_3 w_4\Delta t/2} e^{iL_4 w_5\Delta t/2} e^{iL_3 w_6\Delta t/2} e^{iL_4 w_7\Delta t/2}$$

$$+O(\Delta t^5), \tag{28}$$

$$e^{i(L_5+L_6)\Delta t/2} = e^{iL_6 w_1\Delta t/2} e^{iL_5 w_2\Delta t/2} e^{iL_6 w_3\Delta t/2} e^{iL_5 w_4\Delta t/2} e^{iL_6 w_5\Delta t/2} e^{iL_5 w_6\Delta t/2} e^{iL_6 w_7\Delta t/2}$$

$$+O(\Delta t^5), \tag{29}$$

where

$$w_1 = w_7 = \frac{1}{2(2-2^{1/3})}; \quad w_2 = w_6 = \frac{1}{(2-2^{1/3})};$$

$$w_3 = w_5 = \frac{1-2^{1/3}}{2(2-2^{1/3})}; \quad w_4 = \frac{-2^{1/3}}{(2-2^{1/3})}. \tag{30}$$

The approximate factorizations of the time-evolution operators in eqs 26 – 29 provide a stepwise set of move algorithms of the extended-system variables.[9,24,25] For example, for any system or bath variable X_i, we have

$$X_i(\Delta t) = \exp\left[\Delta t\, a(\mathbf{X})\frac{\partial}{\partial X_i}\right] X_i(0) \cong X_i(0) + \Delta t\, a(\mathbf{X}(0)). \tag{31}$$

When $a(\mathbf{X})$ depends linearly on X_i, as $a_1(\bar{\mathbf{X}}) + a_2(\bar{\mathbf{X}})X_i$ with $\bar{\mathbf{X}}$ denoting the extended system coordinates other than X_i, a slightly improved result can be obtained by directly solving the corresponding differential equation [cf. eq 15],

$$\frac{d}{dt}X_i = a_1(\bar{\mathbf{X}}(0)) + a_2(\bar{\mathbf{X}}(0))X_i . \tag{32}$$

In this case, we have

$$X_i(\Delta t) \cong X_i(0)e^{a_2(\bar{\mathbf{X}}(0))\Delta t} + \frac{a_1(\bar{\mathbf{X}}(0))}{a_2(\bar{\mathbf{X}}(0))}\left[e^{a_2(\bar{\mathbf{X}}(0))\Delta t} - 1\right]. \tag{33}$$

With eq 31 or eq 33, the overall displacements in the extended-system variables $\mathbf{X}$ in a given time step Δt can be performed stepwise as follows.

(1) Under the operation of $e^{i(L_5+L_6)\Delta t}$ as factorized in eq 29, displace the thermostat variables v_η and η and the velocities $\{\mathbf{v}_i\}$ of the particles in the boundary region:

$$e^{iL_6 w_n \Delta t/2} v_\eta \quad \rightarrow \quad v_\eta = v_\eta + (w_n \Delta t / 2)G_\eta / Q_\eta , \tag{34}$$

$$e^{iL_5 w_n \Delta t/2} \eta \quad \rightarrow \quad \eta = \eta + (w_n \Delta t / 2)v_\eta , \tag{35}$$

$$e^{iL_5 w_n \Delta t/2} \mathbf{v}_i \quad \rightarrow \quad \mathbf{v}_i = \mathbf{v}_i e^{-(w_n \Delta t/2)v_\eta} , \tag{36}$$

where $\{w_n\}$ are the weighting factors given in eq 30, and the value of G_η as defined in eq 23 must be updated upon the changes in $\mathbf{v}_i$.

(2) Recalculate the pressure imbalance ΔP, and then under the operation of $e^{i(L_3+L_4)\Delta t}$ as factorized in eq 28, displace the thermostat variables v_ξ and ξ and the "volume velocity":

$$e^{iL_4 w_n \Delta t/2} v_\xi \quad \rightarrow \quad v_\xi = v_\xi + (w_n \Delta t / 2) G_\xi / Q_\xi , \tag{37}$$

$$e^{iL_3 w_n \Delta t/2} \xi \quad \rightarrow \quad \xi = \xi + (w_n \Delta t / 2) v_\xi , \tag{38}$$

$$e^{iL_3 w_n \Delta t/2} \dot{V} \quad \rightarrow \quad \dot{V} = \dot{V} e^{-(w_n \Delta t/2) v_\xi} + \frac{\Delta P}{W} \frac{1}{v_\xi} \left[1 - e^{-(w_n \Delta t/2) v_\xi} \right], \tag{39}$$

where $\{w_n\}$ are the weighting factors given in eq 30, and the value of G_ξ as defined in eq 23 must be updated upon the change in $\dot{V}$.

(3) Displace the particle velocities under the operation of $e^{iL_2 \Delta t/2}$:

$$e^{iL_2 \Delta t/2} \mathbf{v}_i \quad \rightarrow \quad \mathbf{v}_i = \mathbf{v}_i + \frac{\Delta t}{2} \frac{\mathbf{f}_i}{m_i} \quad \text{for particles in the inner region,} \tag{40}$$

$$e^{iL_2 \Delta t/2} \mathbf{v}_i \quad \rightarrow \quad \mathbf{v}_i = \mathbf{v}_i e^{-v_\varepsilon \Delta t/2} + \frac{\mathbf{f}_i}{m_i} \frac{1}{v_\varepsilon} \left(1 - e^{-v_\varepsilon \Delta t/2} \right)$$

for particles in the boundary region, (41)

where $v_\varepsilon = \dot{V} / (3V_b)$.

(4) Displace the particle coordinates and adjust the volume under the operation of $e^{iL_1 \Delta t}$:

$$e^{iL_1 \Delta t} \mathbf{r}_i \quad \rightarrow \quad \mathbf{r}_i = \mathbf{r}_i + \Delta t \, \mathbf{v}_i \quad \text{for particles in the inner region,} \tag{42}$$

$$e^{iL_1 \Delta t} \mathbf{r}_i \quad \rightarrow \quad \mathbf{r}_i = \mathbf{r}_i e^{v_\varepsilon \Delta t} + \mathbf{v}_i \frac{1}{v_\varepsilon} \left(e^{v_\varepsilon \Delta t} - 1 \right)$$

for particles in the boundary region, (43)

$$e^{iL_1 \Delta t} V \quad \rightarrow \quad V = V + \Delta t \dot{V} , \tag{44}$$

(5) Apply the periodic boundary condition, update the nearest-neighbor list, and recalculate the forces $\{\mathbf{f}_i\}$ on the particles as well as N_b, V_b, and v_ε.

(6) Displace the particle velocities under the operation of $e^{iL_2\Delta t/2}$ according to the equations in eqs 40 and 41.

(7) Recalculate G_ξ and ΔP as defined in eq 23, and impose the time-evolution by the operation of $e^{i(L_3+L_4)\Delta t}$ as factorized in eq 28; see eqs. 37 – 39.

(8) Recalculate G_η as defined in eq 23, and impose the time-evolution by the operation of $e^{i(L_5+L_6)\Delta t}$ as factorized in eq 29; see eqs. 34 – 36.

(9) Record the extended-system coordinates $\mathbf{X}(t+\Delta t)$ at the new time step, and check the values of H' in eq 11, N_b, density, system temperature, internal pressure, and so on.

4.3. Numerical test of the MD method

4.3.1. Simulation details

To evaluate the efficiency of our MD method in attaining the target temperature and pressure and to check the conformity of the calculated equilibrium properties to the constant-NPT ensemble system, we have simulated the Lennard-Jones (LJ) particle system modeling the argon fluid under high pressure. We modified the MD codes provided by Frenkel and Smit.[2] The basic units used in the simulations are as follows; length in σ, energy in ε, and mass in m with σ, ε and m being the model LJ potential parameters and the mass of an argon atom, respectively. From

these units, other units follow: for instance, time in $\sigma\sqrt{m/\varepsilon}$ and temperature in ε / k_B.

The N particles are moved according to the algorithm described in Section 2 with time step size Δt of 0.001. The LJ potential is truncated and shifted at the cutoff radius of 3.0, so that we calculate the internal pressure of the boundary region with the correction for the truncation as[2]

$$\mathcal{P}_b = \frac{1}{3V_b}\sum_i{}'' \left(\frac{\mathbf{p}_i^2}{m_i} + \mathbf{r}_i \cdot \mathbf{f}_i \right) + \frac{16\pi}{3}\varepsilon\rho^2\sigma^3 \left[\frac{2}{3}\left(\frac{\sigma}{r_c}\right)^9 - \left(\frac{\sigma}{r_c}\right)^3 \right]. \tag{45}$$

Here, ε and σ are the Lennard-Jones potential parameters, r_c is the cutoff radius, and ρ is the number density in the boundary region, which is not much different from the overall number density, N/V. The Verlet neighbor list method[1] is also employed with the cutoff of 4.0.

The boundary region can be defined by two parameters, the relative volume V_b/V and its thickness δ. We fix the value of V_b/V and adjust δ with volume fluctuation as

$$\delta = \frac{L}{2}\left[1 - \left(1 - \frac{V_b}{V} \right)^{1/3} \right]. \tag{46}$$

The relative volume of the boundary region can be as small as 0.2 for a system of 2,048 LJ particles.

Following the previous works,[9] we set the effective masses of the bath variables according to the following equation,

$$Q_\eta = 3N_b\tau_T^2 k_B T\,, \tag{47}$$

$$Q_\xi = \tau_T^2 k_B T\,, \tag{48}$$

$$W = N_b\tau_P^2 k_B T / V_b^2\,, \tag{49}$$

During the course of simulation, the value of N_b may fluctuate slightly, but the above effective masses are calculated with a fixed value of $N_b (= NV_b / V)$. Below we will present the extensive simulation results to examine the effects of different choice of the parameter values, V_b / V, τ_T, and τ_P.

4.3.2. Thermostatting and Barostatting efficiency

We first evaluate the efficiency of our MD method in attaining the target temperature and pressure for simulating a constant-NPT ensemble system. Starting with a system containing 2,048 LJ particles equilibrated at the target temperature 0.80 and the target pressure 0.50, we run the trajectory for 1×10^6 time steps with $V_b / V = 0.3$, $\tau_T = 1.0$ and $\tau_P = 10$, during which the average of the kinetic temperature is maintained at the value of 0.80. We then subject the system to a sudden temperature jump; the target temperature is raised to 1.20. After running the system trajectory for 1×10^6 time steps, we then switch the target temperature back to 0.80 and run the trajectory for additional 1×10^6 time steps.

The response of the system to the sudden temperature changes is displayed in Figure 4.1, in which the variation of the instant kinetic temperature with time is plotted. The result for the whole system is drawn in gray color, while the result for

the inner region alone is drawn in black color. We find that the mean temperature of the inner region also settles down to the new target value very quickly in less than 1×10^4 time steps. Although the initial fluctuation right after the temperature jump is quite large, it also relaxes to the normal value after about 5×10^4 time steps. After the initial fluctuations, the mean kinetic temperature of the inner region as well as the whole system is kept at 1.20 and 0.80 in the respective time interval after the temperature jumps.

Similarly, Figure 4.2 displays the response of the system after the pressure jumps. Starting with a system containing 2048 LJ particles equilibrated at the target temperature 1.00 and the target pressure 0.50, the target pressure is increased to 1.00 at 1×10^6 time steps and then decreased back to 0.50 at 2×10^6 time steps. The trajectory was run with $V_b / V = 0.3$, $\tau_T = 1.0$ and $\tau_P = 10$. Again, we plot the variation of internal pressure of the whole system in gray color, while that for the inner region in black color. We see that barosttaing is as efficient as thermostatting. The mean value of internal pressure settles down to the new target value very rapidly. After the initial fluctuation, the mean value of internal pressure for the inner region as well as for the whole system is maintained at 1.00 and 0.50 in the respective time interval after the pressure jumps.

Figure 4.1. Testing the thermostatting efficiency by sudden changes in the target temperature from 0.80 to 1.20 then back to 0.80. The target pressu re is kept at 0.50. The variation of the kinetic temperature of the whole sys tem is plotted in gray color as a function of time. We also display the vari ation of the kinetic temperature of the inner region alone in black color. No te that the inner region has a little larger fluctuation because it is a smaller system.

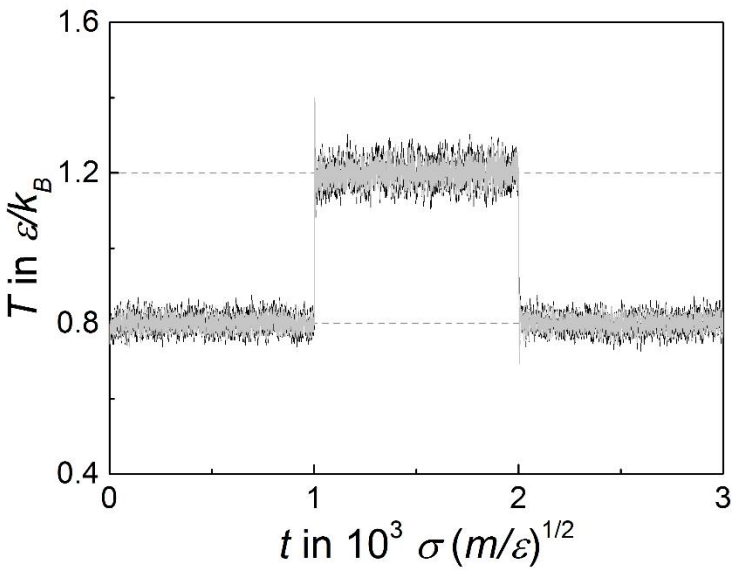

Figure 4.2. Testing the barostatting efficiency by sudden changes in the target pressure from 0.50 to 1.00 then back to 0.50. The target temperature is kept at 1.00. The variation of the internal pressure is plotted as a function of time. The result for the whole system is drawn in gray color while the result of the inner region alone in black color. Note that the inner region has a little larger fluctuation because it is a smaller system.

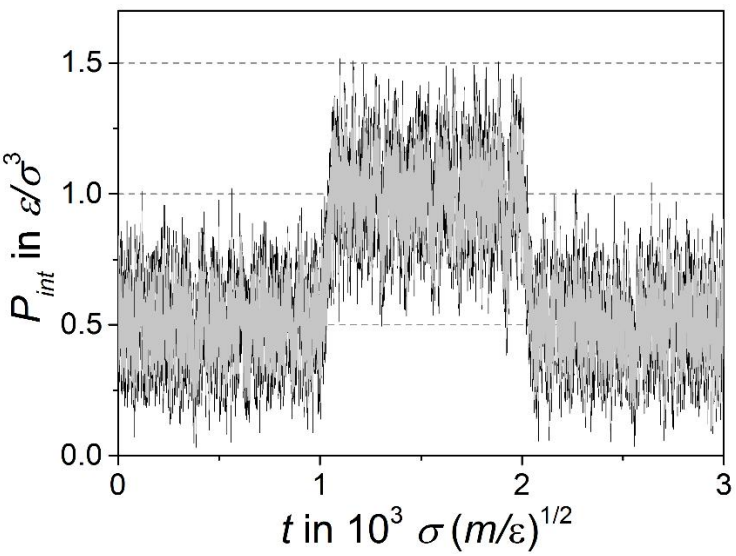

4.3.3. Equilibrium properties

We examine whether the equilibrium properties, calculated after the target temperature and pressure are reached, agree with those obtained from the widely used constant-NPT MD methods. We first calculate the average number density as a function of the target temperature and pressure and compare the results with those obtained from the MD methods of Berendsen et al.[4] and Martyna, et al.,[7-9] who extended the Andersen-Nose-Hoover MD method.[3,5,6] The calculated equation of state data are listed in Table 4.1.

For each data point in Table 4.1, we have run a trajectory of 2,048 LJ particles for 2×10^6 time steps for equilibration and then additional 10^7 time steps for data production with the time step size of 0.001. The relative size of the boundary region, V_b / V, was set to 0.3, and values of the time scale parameters, τ_T and τ_P, were set to 1 and 10, respectively. Other details of the present MD simulations were described above in Section 5.3.1. For the simulations with the MD methods of Martyna et al.[9] (designated as MTTK hereafter) and Berendsen et al.[4], we actually adapt the subroutines included in the TINKER v6.3 simulation package.[28] In the MTTK method, the definition of the barostat variable is different from that in the present MD method, and the "effective mass" associated with the barostat is given by $W_{MTTK} = (3N+1)\tau_P^2 k_B T$.[9,24,28] The time-scale parameter τ_P is physically the same one as we introduced in eq 49 for the present MD method, so that its value is also set to 10. In the MTTK method as implemented in TINKER, the Nose-Hoover chain with four thermostat variables is used with the effective mass given by

$Q_1 = 3N\tau_T^2 k_B T$ and $Q_2 = Q_3 = Q_4 = \tau_T^2 k_B T$. Again, the time-scale parameter τ_T is physically the same one as we introduced in eq 47, so that its value is also set to 1.0. In the MD method of Berendsen et al.[4], two time-scale parameters τ_T^B and τ_P^B are used, which control the relaxation rates to the target temperature and pressure, respectively. We set the values of these parameters as $\tau_T^B = 1.0$ and $\tau_P^B = 5.0$, which are the commonly suggested values.

From Table 4.1 we see that the equation-of-state data produced by the present MD agree with those from the MTTK MD and the Berendsen's MD. The magnitudes of fluctuation (i.e., the standard deviation) in the number density calculated by the present MD also agree with those from the MTTK MD, but those calculated by the Berendsen's MD are significantly smaller as noted in earlier works.[11]

In Table 4.1, we also present the results for the inner region alone in the parentheses. In Table 4.S1 of Supporting Information, the results are compared with those calculated from the MTTK MD. For the MTTK MD method, we just set the inner region of the same size for the purpose of comparison. It is seen that the inner region properties calculated from the present MD method are in good agreement with those calculated from the MTTK MD method. Although only the particles in the boundary region are coupled to the thermostat and barostat variables, the inner region alone as well as the whole system behaves properly as a constant-NPT ensemble system. Furthermore, there is no physical discontinuity

between the inner and the boundary regions except for the dynamical perturbation on the boundary-region particles.

In Table 4.2 we list the average enthalpy per particle, $\langle H \rangle / N = [\langle E \rangle + P\langle V \rangle] / N$, as a function of target temperature and pressure. Again, we observe that the mean values of enthalpy and its magnitudes of fluctuation calculated from the present MD agree with those from the MTTK MD. Although the Berendsen's MD gives the correct mean values of enthalpy, it underestimates the magnitudes of fluctuation significantly. Again, we also list the results for the inner region alone in the parentheses, and the results are compared with those calculated from the MTTK MD; see Table 4.S2 of Supporting Information. It is seen that the inner region properties calculated from the present MD method are in good agreement with those calculated from the MTTK MD method. The inner region alone behaves as a proper constant-NPT system, and that there is no physical discontinuity between the inner and the boundary regions.

Figures 4.3 to 4.5 display the fluctuations in kinetic energy, potential energy, and enthalpy, respectively, that are calculated from the present MD, MTTK MD, and the Berendsen's MD. From Figure 4.3, we see that the fluctuation in kinetic energy per particle, $\langle (\Delta E_k)^2 \rangle^{1/2} / N$, calculated from the simulations of the present and the MTTK MD is that expected for an ideal gas, $\langle (\Delta E_k)^2 \rangle = 3Nk_B^2 T^2 / 2$. In contrast, the Berendsen's MD predicts much smaller fluctuations. The fluctuations in potential energy and enthalpy calculated from the present MD method are also in good agreement with those calculated from the MTTK MD; see Figures 4.4 and 4.5.

On the other hand, the fluctuations in those quantities calculated from the Berendsen's MD are again too small.

In Figure 4.6, we display the radial distribution functions at three different states with (a) $T = 0.8$ and $P = 0.6$, (b) $T = 1.0$ and $P = 0.5$, and (c) $T = 1.2$ and $P = 0.4$. We see that the results of the present MD are indistinguishable from those from the MTTK MD method. Although we do not show here, the velocity distribution functions calculated from the present MD simulations at various state points are indistinguishable from the Maxwell-Boltzmann distribution as it should.

Table 4.1. Number density and its fluctuation as a function of target temperature *T* and target pressure *P*, calculated by the present MD method, MTTK MD method,[9] and Berendsen MD method.[4] For the present MD method, in addition to the data for the whole system, we also present the results for the inner region alone in the parentheses.

T	*P*	Number density		
		Present MD	MTTK	Berendsen
0.80	0.40	0.8286 ± 0.0042 (0.8286 ± 0.0066)	0.8286 ± 0.0042	0.8289 ± 0.0013
0.80	0.50	0.8352 ± 0.0040 (0.8352 ± 0.0064)	0.8350 ± 0.0042	0.8353 ± 0.0013
0.80	0.60	0.8411 ± 0.0042 (0.8411 ± 0.0066)	0.8411 ± 0.0040	0.8413 ± 0.0013
1.00	0.40	0.7498 ± 0.0053 (0.7498 ± 0.0072)	0.7499 ± 0.0053	0.7503 ± 0.0017
1.00	0.50	0.7599 ± 0.0050 (0.7598 ± 0.0070)	0.7596 ± 0.0051	0.7600 ± 0.0016
1.00	0.60	0.7685 ± 0.0052 (0.7685 ± 0.0071)	0.7685 ± 0.0049	0.7689 ± 0.0016
1.20	0.40	0.6621 ± 0.0065 (0.6620 ± 0.0081)	0.6614 ± 0.0070	0.6623 ± 0.0021
1.20	0.50	0.6774 ± 0.0060 (0.6775 ± 0.0077)	0.6777 ± 0.0063	0.6782 ± 0.0020
1.20	0.60	0.6915 ± 0.0060 (0.6915 ± 0.0078)	0.6915 ± 0.0062	0.6921 ± 0.0019

Table 4.2. Average enthalpy per particle and its fluctuation as a function of target temperature *T* and target pressure *P*, calculated by the present MD method, MTTK MD method,[9] and Berendsen MD method.[4] For the present MD method, in addition to the results for the whole system, we also present the results for the inner region alone in the parentheses.

T	*P*	Enthalpy		
		Present MD	MTTK	Berendsen
0.80	0.40	-3.705 ± 0.039 (-3.705 ± 0.044)	-3.705 ± 0.038	-3.709 ± 0.008
0.80	0.50	-3.626 ± 0.038 (-3.626 ± 0.043)	-3.624 ± 0.038	-3.628 ± 0.008
0.80	0.60	-3.543 ± 0.039 (-3.544 ± 0.044)	-3.543 ± 0.038	-3.546 ± 0.008
1.00	0.40	-2.724 ± 0.048 (-2.724 ± 0.054)	-2.725 ± 0.048	-2.729 ± 0.010
1.00	0.50	-2.658 ± 0.048 (-2.657 ± 0.054)	-2.656 ± 0.048	-2.660 ± 0.010
1.00	0.60	-2.585 ± 0.049 (-2.585 ± 0.056)	-2.585 ± 0.047	-2.589 ± 0.010
1.20	0.40	-1.701 ± 0.059 (-1.700 ± 0.066)	-1.696 ± 0.061	-1.704 ± 0.013
1.20	0.50	-1.659 ± 0.057 (-1.660 ± 0.064)	-1.660 ± 0.058	-1.665 ± 0.013
1.20	0.60	-1.611 ± 0.058 (-1.610 ± 0.065)	-1.611 ± 0.059	-1.617 ± 0.012

Figure 4.3. Fluctuations in kinetic energy calculated from the present MD (black squares), MTTK MD (red circles), and the Berendsen's MD (blue triangles). The pressure is varied as the abscissa, and the temperature is varied as 0.8, 1.0, and 1.2 (from top to bottom). Results of the present MD are hardly distinguishable from those of MTTK MD.

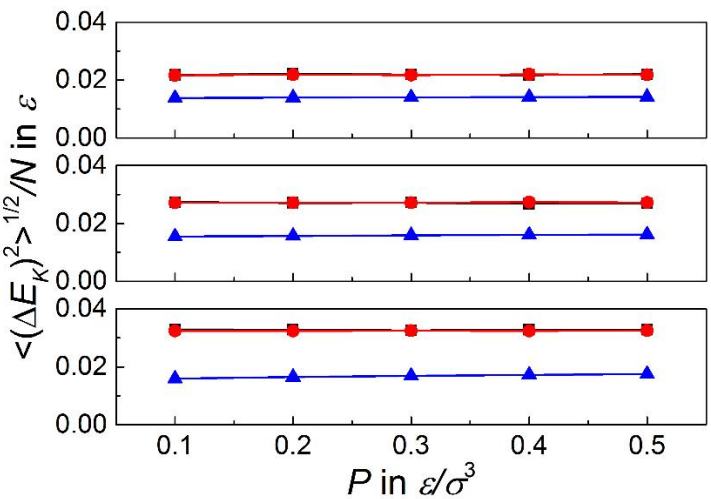

Figure 4.4. Fluctuations in potential energy calculated from the present MD (black squares), MTTK MD (red circles), and the Berendsen's MD (blue triangles). The pressure is varied as the abscissa, and the temperature is varied as 0.8, 1.0, and 1.2 (from top to bottom). Results of the present MD are hardly distinguishable from those of MTTK MD.

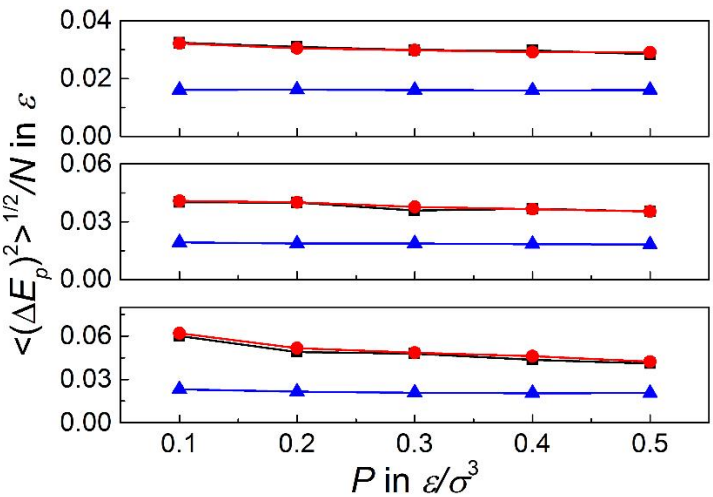

Figure 4.5. Fluctuations in enthalpy calculated from the present MD (black squares), MTTK MD (red circles), and the Berendsen's MD (blue triangles). The pressure is varied as the abscissa, and the temperature is varied as 0.8, 1.0, and 1.2 (from top to bottom). Results of the present MD are hardly distinguishable from those of MTTK MD.

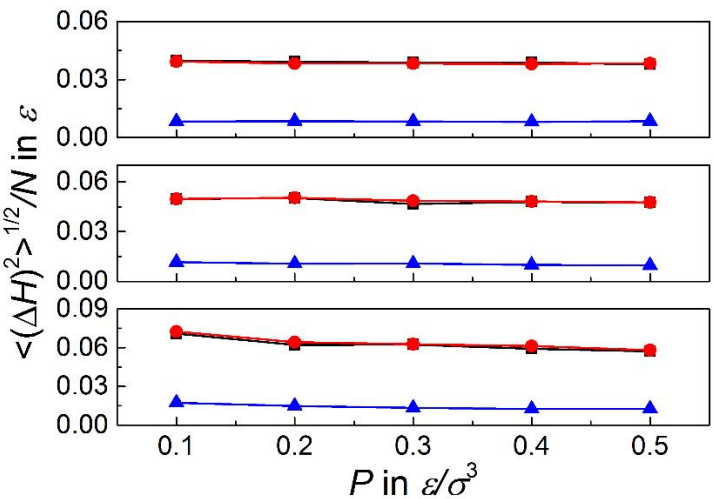

Figure 4.6. Radial distribution functions at three different states with (a) $T = 0.8$ and $P = 0.6$, (b) $T = 1.0$ and $P = 0.5$, and (c) $T = 1.2$ and $P = 0.4$.

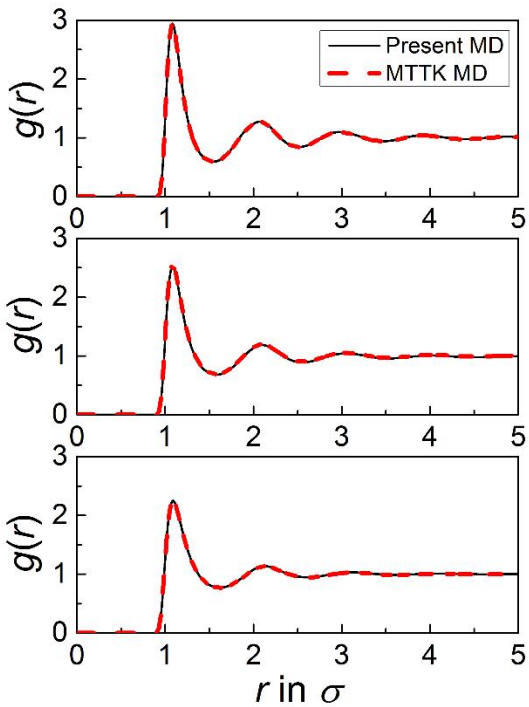

4.3.4 Shirts test

Shirts proposed a rigorous test method for validating the sampling from various equilibrium ensembles.[21] For example, for constant-NPT ensembles, he suggested that the following relations must be verified:

$$\ln\left[\frac{P(H|T_2,P)}{P(H|T_1,P)}\right] = \ln\frac{T_2}{T_1} + \frac{1}{k_B}\left(\frac{G_2}{T_2} - \frac{G_1}{T_1}\right) - \frac{1}{k_B}\left(\frac{1}{T_2} - \frac{1}{T_1}\right)H\,, \tag{50}$$

$$\ln\left[\frac{P(V|T,P_2)}{P(V|T,P_1)}\right] = \ln\frac{P_1}{P_2} + \frac{G_2 - G_1}{k_B T} - \frac{P_2 - P_1}{k_B T}V\,, \tag{51}$$

$$\ln\left[\frac{P(V,E|T_2,P_2)}{P(V,E|T_1,P_1)}\right]$$

$$= \ln\frac{T_2 P_1}{T_1 P_2} + \frac{1}{k_B}\left(\frac{G_2}{T_2} - \frac{G_1}{T_1}\right) - \frac{1}{k_B}\left(\frac{1}{T_2} - \frac{1}{T_1}\right)E - \frac{1}{k_B}\left(\frac{P_2}{T_2} - \frac{P_1}{T_1}\right)V\,. \tag{52}$$

Here, $P(H|T,P)$ and $P(V|T,P)$ denote the probability densities that a system in the constant-NPT ensemble with target temperature and pressure given by T and P has the enthalpy $H\,(=E+PV)$ and the volume V, respectively, while $P(V,E|T,P)$ is the joint probability density that the system has the volume V and the energy E. Equation 50 tells that the logarithm of the ratio of probability distributions of H for two systems with different temperatures must vary linearly with H at least in the range of H where the distributions overlap. Equations 51 and 52 bears similar information for the respective distributions.

To check that sampling of the state points by the present MD method conforms to eq 50, we have carried out a pair of simulations with $T_1 = 0.98$ and $T_2 = 1.02$.

In both simulations, P was set to 0.5, and the thermostat and barostat parameters τ_T and τ_p were set to 1.0 and 10, respectively. In each simulation, the system containing 2048 LJ particles was equilibrated for 2×10^6 time steps and then its trajectory was run for 10^7 time steps for data production. From a histogram analysis, the enthalpy distributions were calculated, and the resulting $\ln[P(H|T_2,P)/P(H|T_1,P)]$ vs. H curve in the range of H where the distributions overlap was fitted to a straight line using the method of linear squares.[29] The result is displayed in Figure 4.7. The calculated slope 0.0399 ± 0.0006, with the coefficient of determination $R^2=0.990$, is in good agreement with the expected value of $k_B^{-1}(T_1^{-1}-T_2^{-1})=0.0400$.

To check if the volume distributions conform to eq 51, we have carried out a pair of simulations with $P_1=0.4$ and $P_2=0.6$. In both simulations, T was set to 1.0, and the other settings of simulations were the same as described above. Again, the volume distributions were calculated from the histogram analysis, and the resulting $\ln[P(V|T,P_2)/P(V|T,P_1)]$ vs. V curve in the range of V where the distributions overlap was fitted to eq 51. The result is displayed in Figure 4.8. The calculated slope -0.196 ± 0.003, with the coefficient of determination $R^2=0.970$, is in good agreement with the expected value of $(P_1-P_2)/(k_BT)=-0.200$.

To check if the joint distributions of V and E conform to eq 52, we have carried out a pair of simulations with ($T_1=0.99$, $P_1=0.45$) and ($T_2=1.01$, $P_2=0.50$). In both simulations, the other settings of simulations were the same as described

above. Figure 4.9 displays the simulation results. $\ln[P(V,E|T_2,P_2)/P(V,E|T_1,P_1)]$ vs. E curves were fitted to eq 52 for three fixed values of V: (a) $V = 2{,}695$, (b) $V = 2{,}700$, and (c) $V = 2705$. On the other hand, $\ln[P(V,E|T_2,P_2)/P(V,E|T_1,P_1)]$ vs. V curves were fitted to eq 52 for three fixed values of E: (d) $E = -6{,}805$, (e) $E = -6{,}800$, and (f) $E = -6{,}795$. Compared to the above two one-dimensional distributions, the results involve a considerable statistical noise. Nevertheless, the calculated slopes of the curves are in fair agreement with the expected values of $k_B^{-1}(T^{-1} - T^{-2}) = 0.0200$ and $k_B^{-1}(P_1/T_1 - P_2/T_2) = -0.0405$, respectively. The slope and the R^2 coefficient are given by (a) 0.0218 ± 0.0004 and 0.983, (b) 0.0199 ± 0.0005 and 0.968, (c) 0.0181 ± 0.0005 and 0.959, (d) -0.0465 ± 0.0047 and 0.670, (e) -0.0421 ± 0.0042 and 0.672, and (f) -0.0464 ± 0.0055 and 0.588.

Figure 4.7. The enthalpy distributions calculated from the present MD simulations conform to those expected for constant-NPT ensemble systems. The enthalpy distributions $P(H|T_1,P)$ and $P(H|T_2,P)$ were calculated with $T_1 = 0.98$, $T_2 = 1.02$, and $P = 0.5$.

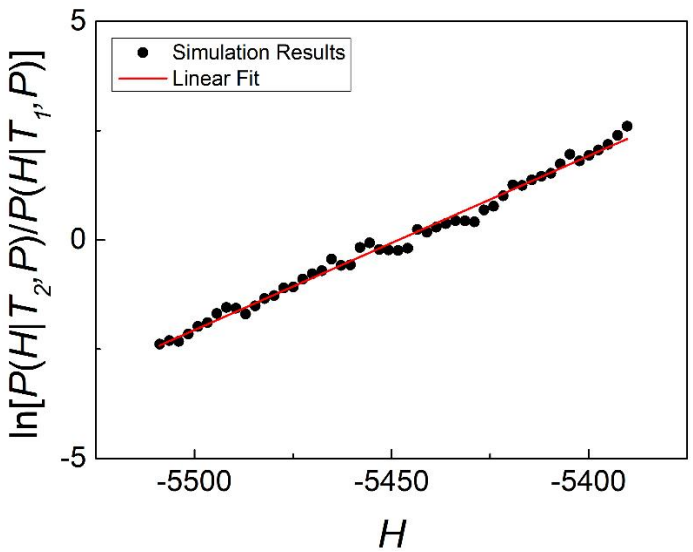

Figure 4.8. The volume distributions calculated from the present MD simulations conform to those expected for constant-NPT ensemble systems. The volume distributions $P(V|T,P_1)$ and $P(V|T,P_2)$ were calculated with $P_1 = 0.4$, $P_2 = 0.6$, and $T = 1.0$.

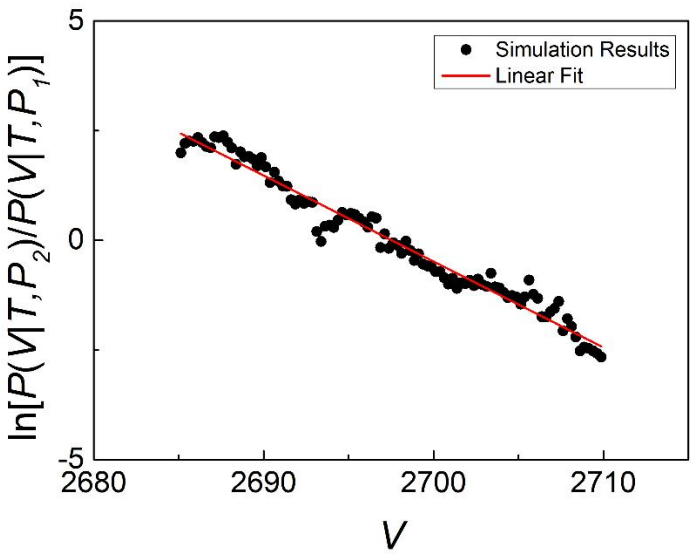

Figure 4.9. The joint distributions of *V* and *E* calculated from the present MD simulations conform to those expected for constant-NPT ensemble systems. The distributions $P(V,E|T_1,P_1)$ and $P(V,E|T_2,P_2)$ were calculated with ($T_1=0.99$, $P_1=0.45$) and ($T_2=1.01$, $P_2=0.50$).

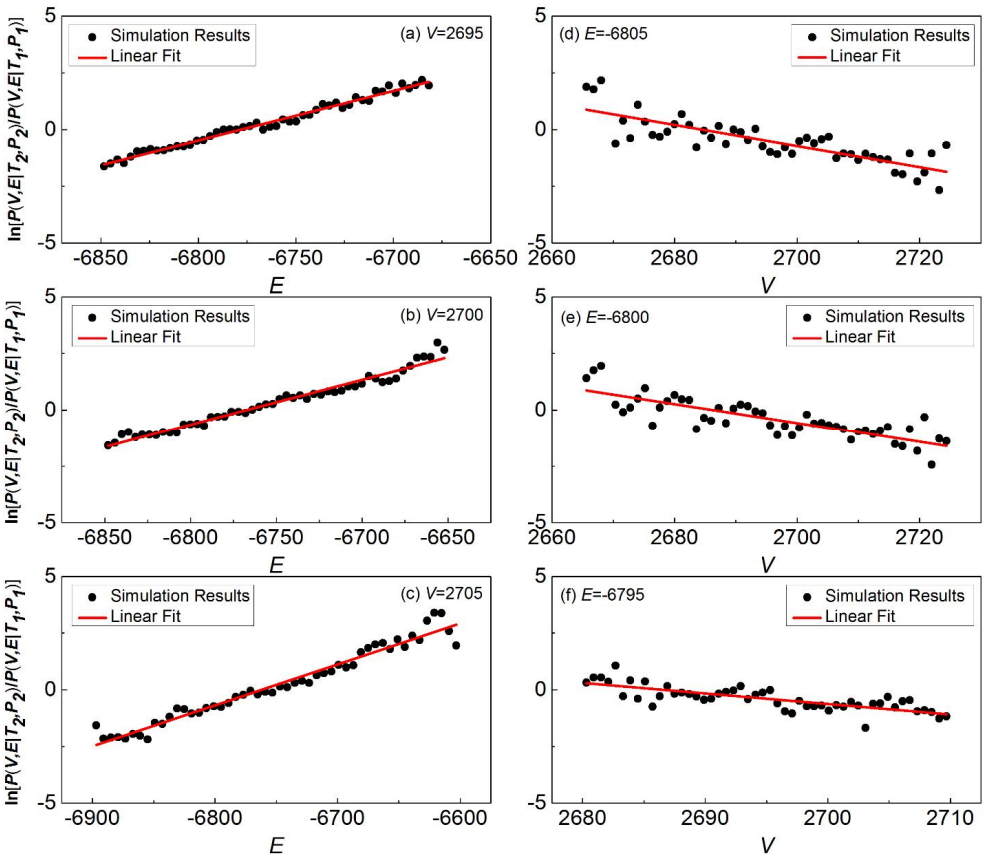

4.3.5. Dynamic properties

Recently Basconi and Shirts[14] investigated the effects of various thermostatting algorithms on the dynamic properties calculated in the MD simulations. They found that while the Andersen[3] and Langevin[30] thermostats slow down the self-diffusion of a tagged molecule, the popular velocity rescaling thermostats like the Berendsen,[4] Bussi,[11] and Nose-Hoover[5,6,9] thermostats do not much affect the kinetic properties as long as the coupling between particles and the thermostat is not too strong.

The main purpose of the present MD method is to calculate the correct dynamic properties of a solute molecule of primary interest. In the present test simulations, this "primary solute molecule" is a chain of 7 LJ particles, in which the adjacent particles interact with a harmonic potential with a spring constant of $k_v = 2$ and the equilibrium separation of $l_{eq} = 1.12$. The primary solute molecule is placed at the center of simulation box. To keep the dynamics of the primary solute molecule intact from the disturbance from the moving, thermal boundary, we may need occasionally to move the boundary of the simulation box, when any particle of the primary solute molecule approaches the boundary region within the distance of 1 σ.

For this purpose, we keep dual registry of the positions of the particles: one for the *actual* position vectors and the other for the *virtual* position vectors inside the simulation box. The virtual coordinates are adjusted when the periodic boundary condition is imposed at every time step and when the boundary of the simulation box is moved to reposition the primary solute molecule at the center of the

simulation box. Dynamic properties such as the mean square displacement are calculated from the actual position vectors, while the forces acting on the molecules are calculated from the virtual position vectors.

We have investigated the effects of coupling with the thermostat and barostat on the self-diffusion of the primary solute molecule. Since the MTTK MD method is known to give the most reliable results in many cases, we confine ourselves to comparing the results of the present MD and the MTTK MD methods with those of the constant-NVE MD method carried out at the same average temperature and pressure.

The test system consists of 2,048 LJ particles, of which 7 particles are bound as a chain as described above. After equilibrating the system at $T = 1.00$ and $P = 0.40$ by the MTTK MD method, we have carried out the constant-NVE MD simulation by using the velocity Verlet algorithm. We have monitored the variations of kinetic temperature and internal pressure during the course of constant-NVE MD simulation, and have selected only those trajectories in which the average kinetic temperature and the average internal pressure were kept at $T = 1.00 \pm 0.01$ and $P = 0.40 \pm 0.02$, respectively. One hundred such trajectories have been calculated. The time length of each trajectory was 10^6 steps.

The constant-NPT MD simulations at $T = 1.00$ and $P = 0.40$ have been carried out by using the present MD and the MTTK MD methods. For both MD methods, we have tested two sets of bath coupling parameters; (i) $\tau_T = 1.0$ and $\tau_P = 10$, and (ii) $\tau_T = 100$ and $\tau_P = 1000$. As mentioned in Section 5.3.1, these

parameters are defined slightly differently in the two MD methods, but each set of the coupling parameters is expected to give the enthalpy and volume fluctuations of about the same magnitude. For each MD method with a given set of the coupling parameters, one hundred trajectories of 10^6 time steps have been calculated.

In Figure 4.10, the mean squared displacements $\langle[\Delta\mathbf{r}(t)]^2\rangle$ of a chain of 7 particles, calculated from the five sets of MD simulations are plotted. For small *t*, the results of different MD simulations are hardly distinguishable. We thus plot the results for $t > 8$. The curves become perfectly linear for $t > 8$, so that the self-diffusion constant of the solute molecule has been calculated by $D = [\langle[\Delta\mathbf{r}(10)]^2\rangle - \langle[\Delta\mathbf{r}(8)]^2\rangle] / 6(10-8)$ and listed in Table 4.3.

We see that the results of the present MD are in excellent agreement with that of constant-NVE MD, regardless of the bath coupling parameters. In fact, the results of both sets of the present MD simulations are hardly distinguishable from that of constant-NVE MD simulations in Figure 4.10. On the other hand, the results obtained from the two sets of MTTK MD simulations are seen to deviate slightly. The self-diffusion constants calculated from the two sets of the present MD simulations differ from the estimate of the constant-NVE MD simulation by 0.4% with $\tau_T = 1.0$ and $\tau_P = 10$ and by 0.9% with $\tau_T = 100$ and $\tau_P = 1000$. On the other hand, the diffusion constant calculated from the MTTK MD simulation with $\tau_T = 1.0$ and $\tau_P = 10$ deviates by 1.5% and that calculated with $\tau_T = 100$ and $\tau_P = 1000$ by 1.3%.

Figure 4.10. Mean squared displacements of a chain of 7 LJ particles bound by harmonic springs at $T = 1.0$ and $P = 0.4$, calculated from the constant-NVE MD, the present MD, and the MTTK MD with two different sets of bath coupling parameters. The results of both sets of the present MD simulations are hardly distinguishable from that of constant-NVE MD simulations. The error bars represent the standard errors for the constant-NVE results obtained for 100 trajectories.

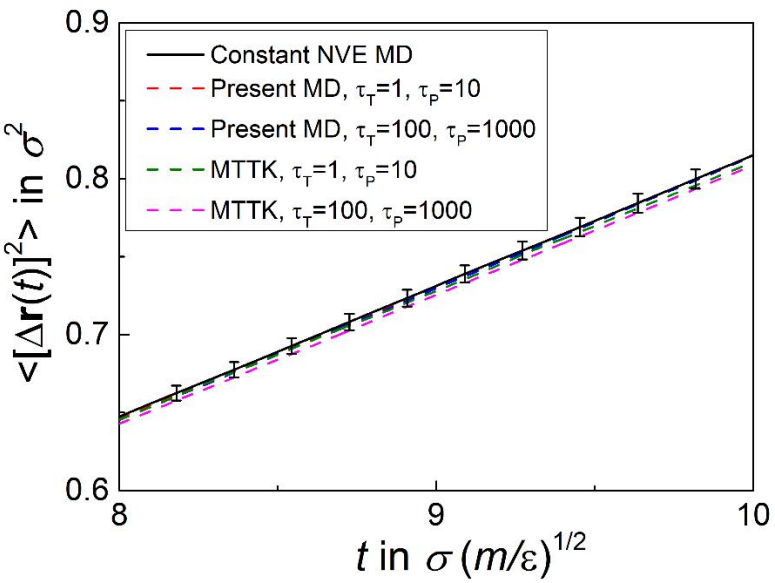

Table 4.3. Self-diffusion constant calculated by the constant-NVE MD method, the present MD method, and the MTTK MD method with two different sets of bath coupling parameters.

MD Method	Diffusion constant
Present MD with $\tau_T = 1.0$, $\tau_P = 10$.	0.01403 ± 0.00015
Present MD with $\tau_T = 1.0 \times 10^2$, $\tau_P = 1.0 \times 10^3$	0.01410 ± 0.00012
MTTK MD with $\tau_T = 1.0$, $\tau_P = 10$.	0.01377 ± 0.00014
MTTK MD with $\tau_T = 1.0 \times 10^2$, $\tau_P = 1.0 \times 10^3$	0.01380 ± 0.00015
Constant-NVE MD	0.01398 ± 0.00017

4.3.6. Additional tests

In the supporting information, we present some additional simulation results for supporting the quality of the present MD method. As mentioned in Section 5.2, the validity of the present MD method relies on the approximate constancy of the particle number, N_b, in the boundary region. In Table 4.S3, we list the mean and standard deviation of N_b for the nine simulation sets listed in Tables 4.1 and 4.2. For the two cases with the highest and lowest particle number density, we also display the variation of N_b with time in Figure 4.S1. We see that although N_b fluctuates a little, its mean value stays around 614.4 which is an expected value if the whole system is homogeneous in density. In Figure 4.S2, we display the variation of H' defined in eq 11 for the two cases of Table 4.S3 with the highest and lowest particle number density. We see that H' remains around a steady-state value.

In Tables 4.S4, 4.S5, and 4.S6, we present simulation results generated with thinner boundary region with $V_b / V = 0.2$ for a system of 2,048 LJ particles. In Table 4.S7, 4.S8, and 4.S9, we also present the simulation results for a larger system with $N = 8{,}192$ and $V_b / V = 0.3$. All the simulation results are in excellent agreement with those of the MTTK MD method. It is seen that the inner region alone as well as the whole system behaves as a proper constant-NPT system, and that there is no physical discontinuity between the inner and the boundary regions.

4.4. Conclusion

We have introduced a new constant-NPT MD method by modeling the actual role of movable, thermal boundary, which initially perturbs only the motion of particles in the vicinity of the boundary. A key advantage of the present MD method is that the motion of a solute molecule of primary interest can be kept intact from the coupling with the thermostat and barostat. This enables a reliable calculation of dynamic properties of a primary solute molecule of interest located in the inner region of the simulation box.

Another advantage is that the present MD method does not cause any problem in simulating the systems involving the inhomogeneity in compressibility. Due to the reason as mentioned in the introduction, the existing barostatting algorithms based on Andersen barostat cannot treat such systems properly.

We have confirmed that the present MD produces correct equilibrium properties of constant-NPT ensemble systems by calculating the number density and enthalpy and their fluctuations as well as the fluctuations of the kinetic and potential energies. We also performed the Shirts test to confirm that the present MD samples the correct enthalpy and volume distributions expected for constant-NPT ensemble systems. Above all, we confirmed that the present MD method produces the correct dynamic properties of the central solute as it promised.

Because the main purpose of the present paper is to introduce a new MD method and to check its usability, we have dealt with the simplest system consisting of LJ

particles. In a future work, we will extend the formulation to deal with more complex systems including a quantum-mechanical solute molecule.

Supporting information

Table 4.S1. Number density and its fluctuation in the inner region as a function of target temperature *T* and target pressure *P*, calculated by the present MD method and MTTK MD method.

T	*P*	Number density in the inner region	
		Present MD	MTTK
0.80	0.40	0.8286 ± 0.0066	0.8288 ± 0.0065
0.80	0.50	0.8352 ± 0.0064	0.8351 ± 0.0064
0.80	0.60	0.8411 ± 0.0066	0.8411 ± 0.0065
1.00	0.40	0.7498 ± 0.0072	0.7499 ± 0.0072
1.00	0.50	0.7598 ± 0.0070	0.7596 ± 0.0071
1.00	0.60	0.7685 ± 0.0071	0.7685 ± 0.0071
1.20	0.40	0.6620 ± 0.0081	0.6616 ± 0.0081
1.20	0.50	0.6775 ± 0.0077	0.6777 ± 0.0079
1.20	0.60	0.6915 ± 0.0078	0.6915 ± 0.0077

Table 4.S2. Average enthalpy per particle and its fluctuation in the inner region as a function of target temperature *T* and target pressure *P*, calculated by the present MD method and MTTK MD method.

T	*P*	Enthalpy per particle in the inner region	
		Present MD	MTTK
0.80	0.40	-3.705 ± 0.044	-3.707 ± 0.043
0.80	0.50	-3.626 ± 0.043	-3.624 ± 0.043
0.80	0.60	-3.544 ± 0.044	-3.543 ± 0.043
1.00	0.40	-2.724 ± 0.054	-2.724 ± 0.054
1.00	0.50	-2.657 ± 0.054	-2.657 ± 0.055
1.00	0.60	-2.585 ± 0.056	-2.584 ± 0.054
1.20	0.40	-1.700 ± 0.066	-1.697 ± 0.065
1.20	0.50	-1.660 ± 0.064	-1.659 ± 0.066
1.20	0.60	-1.610 ± 0.065	-1.610 ± 0.064

Table 4.S3. The mean and standard deviation of the particle number, N_b, in the boundary region, calculated for a system of 2,048 LJ particles by the present MD method with the volume ratio for the boundary region set to $V_b / V = 0.3$.

T	P	$\langle N_b \rangle$	σ_{N_b}
0.80	0.40	614.4	8.6
0.80	0.50	614.3	8.6
0.80	0.60	614.4	8.6
1.00	0.40	614.4	9.3
1.00	0.50	614.5	9.2
1.00	0.60	614.4	9.1
1.20	0.40	614.6	10.4
1.20	0.50	614.2	10.2
1.20	0.60	614.5	10.0

Figure 4.S1. The variation of N_b with time for the two cases of Table 4.S1 with the highest density ($T = 0.80$ and $P = 0.60$) and the lowest density ($T = 1.20$ and $P = 0.40$).

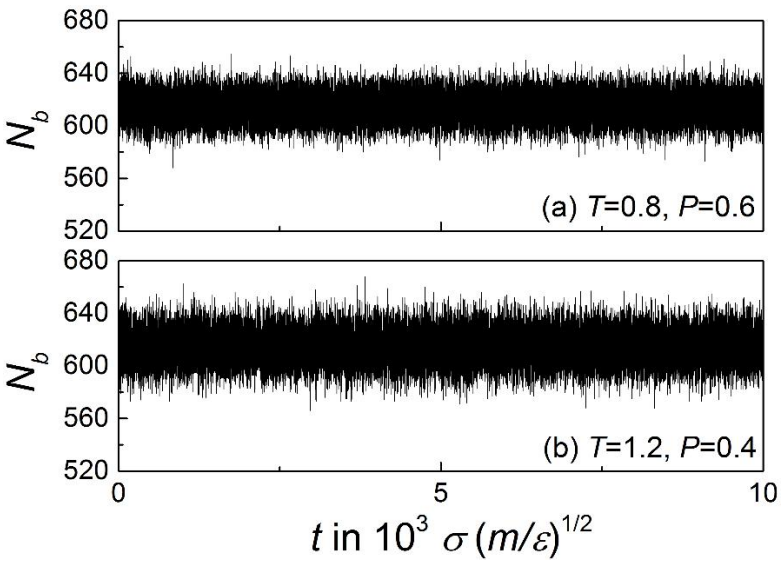

Figure 4.S2. The variation of H' defined in eq 11 with time for the two cases of Table 4.S1 with the highest density ($T = 0.80$ and $P = 0.60$) and the lowest density ($T = 1.20$ and $P = 0.40$).

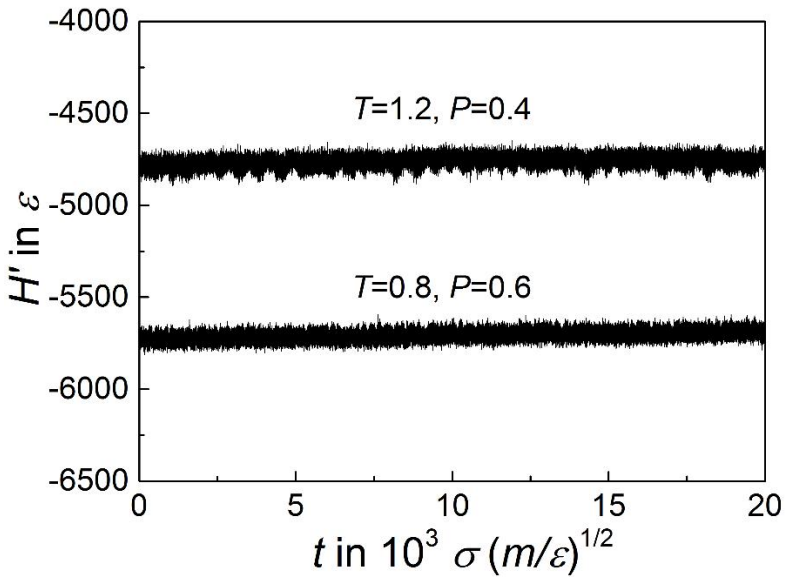

Table 4.S4. Number density and its fluctuation as a function of target temperature *T* and target pressure *P*, calculated for a system with $N = 2{,}048$ by the present MD method and MTTK MD method. For the present MD method the volume ratio for the boundary region is taken to be $V_b / V = 0.2$, and we also present the results for the internal region alone in the parentheses in addition to the data for the whole system.

T	*P*	Number density	
		Present MD	MTTK
0.80	0.60	0.8411 ± 0.0041 (0.8412 ± 0.0055)	0.8411 ± 0.0040
1.00	0.50	0.7594 ± 0.0051 (0.7594 ± 0.0063)	0.7596 ± 0.0051
1.20	0.40	0.6620 ± 0.0065 (0.6620 ± 0.0074)	0.6614 ± 0.0070

Table 4.S5. Average enthalpy per particle and its fluctuation as a function of target temperature T and target pressure P, calculated for a system with $N = 2{,}048$ by the present MD method and MTTK MD method. For the present MD method the volume ratio for the boundary region is taken to be $V_b / V = 0.2$, and we also present the results for the internal region alone in the parentheses in addition to the data for the whole system.

T	P	Enthalpy	
		Present MD	MTTK
0.80	0.60	-3.544 ± 0.038 (-3.544 ± 0.041)	-3.543 ± 0.038
1.00	0.50	-2.654 ± 0.048 (-2.654 ± 0.052)	-2.656 ± 0.048
1.20	0.40	-1.700 ± 0.058 (-1.700 ± 0.061)	-1.696 ± 0.061

Table 4.S6. The mean and standard deviation of the particle number, N_b, in the boundary region, calculated for a system with $N = 2{,}048$ by the present MD method with $V_b / V = 0.2$.

T	P	$\langle N_b \rangle$	σ_{N_b}
0.80	0.60	409.6	7.1
1.00	0.50	409.6	7.9
1.20	0.40	409.6	9.1

Table 4.S7. Number density and its fluctuation as a function of target temperature *T* and target pressure *P*, calculated for a system with $N = 8{,}192$ by the present MD method and MTTK MD method. For the present MD method the volume ratio for the boundary region is taken to be $V_b / V = 0.3$, and we also present the results for the internal region alone in the parentheses in addition to the data for the whole system.

T	*P*	Number density	
		Present MD	MTTK
0.80	0.60	0.8413 ± 0.0020 (0.8413 ± 0.0029)	0.8412 ± 0.0021
1.00	0.50	0.7596 ± 0.0025 (0.7596 ± 0.0033)	0.7597 ± 0.0026
1.20	0.40	0.6618 ± 0.0032 (0.6618 ± 0.0040)	0.6618 ± 0.0033

Table 4.S8. Average enthalpy per particle and its fluctuation as a function of target temperature T and target pressure P, calculated for a system with $N = 8{,}192$ by the present MD method and MTTK MD method. For the present MD method the volume ratio for the boundary region is taken to be $V_b / V = 0.3$, and we also present the results for the internal region alone in the parentheses in addition to the data for the whole system.

T	P	Enthalpy	
		Present MD	MTTK
0.80	0.60	-3.545 ± 0.019 (-3.546 ± 0.022)	-3.544 ± 0.019
1.00	0.50	-2.656 ± 0.024 (-2.656 ± 0.027)	-2.657 ± 0.024
1.20	0.40	-1.700 ± 0.030 (-1.700 ± 0.034)	-1.700 ± 0.030

Table 4. S9. The mean and standard deviation of the particle number, N_b, in the boundary region, calculated for a system with $N = 8{,}192$ by the present MD method with $V_b / V = 0.3$.

T	P	$\langle N_b \rangle$	σ_{N_b}
0.80	0.60	2,457.5	14.3
1.00	0.50	2,457.5	16.1
1.20	0.40	2,457.3	19.5

References

1. Allen, M. P.; Tildesley, D. J. *Computer Simulation of Liquids*; Oxford University Press: Oxford, 1987.
2. Frenkel, D.; Smit, B. *Understanding Molecular Simulation*, 2nd ed.; Academic Press; New York, 2002.
3. Andersen, H. C. Molecular Dynamics Simulations at Constant Pressure and/or Temperature. *J. Chem. Phys.* **1980**, *72*, 2384-2393.
4. Berendsen, H. J. C.; Postma, J. P. M.; van Gunsteren, W. F.; DiNola, A.; Haak, J. R. Molecular Dynamics with Coupling to an External Bath. *J. Chem. Phys*. **1984**, *81*, 3684-3690.
5. Nosé, S. A Unified Formulation of the Constant Temperature Molecular Dynamics Methods. *J. Chem. Phys*. **1984**, *81*, 511-519.
6. Hoover, W. G. Canonical Dynamics: Equilibrium Phase-Space Distributions. *Phys. Rev. A* **1985**, *31*, 1695-1697.
7. Martyna, G. J.; Klein, M. L.; Tuckerman, M. E. Nose-Hoover Chains: The Canonical Ensemble via Continuous Dynamics. *J. Chem. Phys*. **1994**, *97*, 2635-2643.
8. Martyna, G. J.; Tobias, D. J.; Klein, M. L. Constant Pressure Molecular Dynamics Algorithms. *J. Chem. Phys*. **1994**, *101*, 4177-4189.
9. Martyna, G. J.; Tuckerman, M. E.; Tobias, D. J.; Klein, M. L. Explicit Reversible Integrators for Extended Systems Dynamics. *Mol. Phys*. **1996**, *87*, 1117-1157.

10. Lowe, C. P. An Alternative Approach to Dissipative Particle Dynamics. *Europhys. Lett*. **1999**, *47*, 145-151.

11. Bussi, G.; Donadio, D.; Parrinello, M. Canonical Sampling through Velocity Rescaling. *J. Chem. Phys*. **2007**, *126*, 014101.

12. Braga, C.; Travis, K. P. A Configurational Temperature Nose-Hoover Thermostat. *J. Chem. Phys*. **2005**, *123*, 134101.

13. Patra, P. K.; Bhattacharya, B. A Deterministic Thermostat for Controlling Temperature Using All Degrees of Freedom. *J. Chem. Phys*. **2014**, *140*, 064106.

14. Basconi, J. E.; Shirts, M. R. Effects of Temperature Control Algorithms on Transport Properties and Kinetics in Molecular Dynamics Simulations. *J. Chem. Theory Comput*. **2013**, *9*, 2887-2899.

15. Schmidt, J. R.; Skinner, J. L. Hydrodynamic Boundary Conditions, the Stokes-Einstein Law, and Long-Time Tails in the Brownian Limit. *J. Chem. Phys*. **2003**, *119*, 8062-8068.

16. Wong, V.; Case, D. A. Evaluating Rotational Diffusion from Protein MD Simulations. *J. Phys. Chem. B* **2008**, *112*, 6013-6024.

17. Hoover, W. G.; Ashurst, W. T. Nonequilibrium Molecular Dynamics. In *Theoretical Chemistry, Advances and Perspectives, Vol. 1*; Eyring, H., Henderson, D., Eds.; Academic Press: New York, 1975; pp 1-51.

18. Ciccotti, G.; Tenenbaum, A. Canonical Ensemble and Nonequilibrium States by Molecular Dynamics. *J. Stat. Phys*. **1980**, *23*, 767-772.

19. Uline, M. J.; Corti, D. S. Molecular Dynamics in the Isothermal-Isobaric Ensemble: The Requirement of a "Shell" Molecule. II. Simulation Results. *J. Chem. Phys*. **2005**, *123*, 164102.

20. Uline, M. J.; Corti, D. S. Molecular Dynamics at Constant Pressure: Allowing the System to Control Volume Fluctuations via a "Shell" Particle. *Entropy* **2013**, *15*, 3941-3969.

21. Shirts, M. R. Simple Quantitative Tests to Validate Sampling from Thermodynamic Ensembles. *J. Chem. Theory Comput*. **2013**, *9*, 909-926.

22. Tuckerman, M. E.; Mundy, C. J.; Martyna, G. J. On the Classical Statistical Mechanics of Non-Hamiltonian Systems. *Europhys. Lett*. **1999**, *45*, 149-155.

23. Tuckerman, M. E.; Liu, Y.; Ciccotti, G.; Martyna, G. J. Non-Hamiltonian Molecular Dynamics: Generalizing Hamiltonian Phase Space Principles to Non-Hamiltonian Systems. *J. Chem. Phys*. **2001**, *115*, 1678-1702.

24. Tuckerman, M. E.; Alejandre, J.; López-Rendón, R.; Jochim, A. L.; Martyna, G. J. A Liouville-Operator Derived Measure-Preserving Integrator for Molecular Dynamics Simulations in the Isothermal-Isobaric Ensemble. *J. Phys. A: Math. Gen.* **2006**, *39*, 5629-5651.

25. Tuckerman, M. E. *Statistical Mechanics: Theory and Molecular Simulation*; Oxford University Press: Oxford, 2010.

26. Trotter, H. F. On the Product of Semi-Groups of Operators. *Proc. Amer. Math. Soc*. **1959**, *10*, 545-551.

27. Yoshida, H. Construction of Higher Order Symplectic Integrators. *Phys. Lett. A* **1990**, *150*, 262-268.

28. Ponder, J. W.; Richards, F. M. An Efficient Newton-like Method for Molecular Mechanics Energy Minimization of Large Molecules. *J. Comput. Chem*. **1987**, *8*, 1016-1024.

29. Bevington, P. R. *Data Reduction Error Analysis for the Physical Sciences*; McGraw-Hill, New York, 1969.

30. Schneider, T.; Stoll, E. Molecular-Dynamics Study of a Three-Dimensional One-Component Model for Distortive Phase Transitions. *Phys. Rev. B* **1978**, *17*, 1302-1322.

국문초록

자연적이거나 인공적인 계에서의 다양한 종류의 화학 반응들은 반응 분자들의 상대적 확산 속도에 크게 영향을 받는다. 그럼에도 불구하고, 많은 실제적 환경에서의 확산 지배 반응에 대한 쉽게 이해할 만한 설명은 여전히 부족하다.

이러한 문제를 해결하기 위하여, 많은 연구들이 이론적으로 또한 실험적으로 수행되어왔다. 이 논문은 이러한 쟁점을 밝혀내기 위하여 몇몇 특정 조건 하에서의 확산 지배 반응을 다룰 수 있는 이론적이고 계산적인 틀을 제시하고자 한다. 더불어 신뢰할 만한 동역학적 성질을 계산해 낼 수 있는 새로운 일정 온도, 일정 압력 분자 동역학 방법을 제시한다.

이 논문은 네 개의 장으로 구성되어 있다. 우선, 첫 번째 장에서는 논문의 전반적 내용을 기술한다. 스몰루코프스키의 확산 지배 반응 이론은 동종 반응 분자들이 서로 상호작용하지 않는다는 가정에서 출발한다. 그러나 반응 분자들의 농도가 높아질수록 이 가정은 성립하지 않는다. 두 번째 장에서는 반응 분자들의 농도가 높은 경우 적용 가능한 새로운 이론을 제시한다. 활성화에너지가 낮은 전자 전달 반응은 확산 지배 반응의 대표적인 예이다. 시간 의존적인 전자 이전 속도와 전하 분리 확률에 관한 이전의 해석적 이론들은 반응이 접촉 거리에서

일어난다고 가정될 수 있는 경우에 대해서만 구해졌다. 세 번째 장에서는 강한 쿨롱 상호작용과 거리 의존 반응성을 가지고 있는 쌍생 이온들 사이의 시간 의존 전자 이전 속도를 다루는 이론을 유도한다. 분자동역학 전산모사에서 이제까지 널리 사용되어 왔던 온도, 압력 조절 알고리즘들은 고려하고 있는 분자들의 동역학적 성질을 훼손할 수 있는데, 이는 이들의 운동 방정식이 온도, 압력 조절 장치로 인하여 변경되기 때문이다. 네 번째 장에서는 평형 성질뿐만 아니라 동역학적 성질도 정확히 계산할 수 있는 새로운 분자 동역학 모사실험 방법이 제시된다.

주요어 : 확산 지배 반응, 농도 효과, 배제 부피 효과, 전자 전달 속도, 분자동역학

학 번 : 2011-23216